KU LEUVEN

FACULTY OF SCIENCE

Development of a Cell-Irradiation Protocol and ^{225}Ac Recoil-Implantation Generator for Alpha Radiobiology

Daan NAUWELAERTS

CERN-THESIS-2024-260
//2024

Supervisor: Prof. T.E. Cocolios
Institute for Nuclear and Radiation Physics (KU Leuven)

Supervisor: Prof. C. Bartic
Institute for Soft Matter and Biophysics (KU Leuven)

Mentor: J. Johnson
Institute for Nuclear and Radiation Physics (KU Leuven)

Mentors: L. Dedroog and O. Deschaume
Institute for Soft Matter and Biophysics (KU Leuven)

Thesis presented in
fulfillment of the requirements
for the degree of Master of Science
in Physics

Academic year 2023-2024

Preface

When graduating high school, I could not wait to become a student in Leuven. And I must say, I was not disappointed. The past few years have been a remarkable journey and in a way this thesis marks both the end of this chapter as the beginning of a new one. Luckily for me, in this past year when working on my master's thesis, I had many people aiding and supporting me. Without them, this work would never have been completed. Hence, I would like to dedicate this page to thank all these people.

First and foremost, I would like to thank both my supervisors, professor Thomas Elias Cocolios and professor Carmen Bartic, for welcoming me in their research group and introducing me to many amazing new people to collaborate with. I sincerely like to thank both of them for their support and insight in the project. Moreover, I would also like to thank them for their feedback on my work throughout the year. I learned a lot from it.

Secondly, I sincerely would like to thank my daily mentors Lens, Olivier and Jake. Lens and Olivier, I would like to thank both of them for their time and patience while teaching me probably the most basic techniques in (bio)chemistry such as learning how to pipette, making suspensions, etc. Moreover, they were always there for helping me out when I was struggling. Jake, even though he was extremely busy writing his own thesis, he always had the time for helping me out, answering the many questions I had or discussing the project together. I greatly appreciated this.

Subsequently, I would like to extent my gratitude as well to professor Sarah Baatout and professor Piet Van Duppen for their time and effort to read this work.

Of course, this preface would not be complete without mentioning my best friends: Wout, Klaas, Arnout, Lode, Ibe, Peggy and Tibo. I sincerely would like to thank all of you for your friendship and support. I will never forget our many board game nights, the nights we went pooling in Downtown Jack, the nights playing cards and the many other memorable moments we shared together.

Subsequently, I would also like to thank my family for their support and encouragement throughout this journey. However, a special thanks goes out to my sister, for helping me out with the C++ code I utilized in chapter 5.

Lastly, I would like to express my gratitude towards Sarah. Not only for her time and effort in proofreading this entire work, but also for always believing in me, her never-ending support and her encouragement this past year.

Daan Nauwelaerts
June 2024

Scientific Summary

Nowadays, whenever a patient is diagnosed with metastatic cancer, the survival rate following diagnosis is typically low. For example, of all patients diagnosed with metastatic breast cancer only 28% of all women (and 22% of all men) will still be alive after five years. This number drops to 7% for patients diagnosed with metastatic lung cancer [1]. However, in the last two decades, promising results have been observed in clinical trials using targeted alpha therapy (TAT) for treating metastatic cancers. In TAT, an alpha-emitting radionuclide is attached to a vector that will carry the radionuclide towards the cancer cells by traveling along the circulatory and lymphatic system in the body. Even though the clinical trials look promising, TAT is nowadays not on a large scale clinically in use for cancer treatment. This is mainly due to (1) the high costs, (2) the availability and (3) the effects of the alpha-emitting sources and their recoiling daughter nuclei on (cancer) cells that are not yet fully understood.

In the first part of this thesis, the focus will be on the further development of a cell-irradiation protocol that can be used to determine the radiobiological effects of the emitted alpha particles in the decay of ^{225}Ac and subsequent daughter nuclei. The development of this protocol is the first step in a larger experimental endeavor to probe the radiobiological effects of the recoiling ^{225}Ac daughter nuclei. The goal of this protocol is to study the impact of the alpha particles on the cancerous cells by externally irradiating a hydrogel containing HeLa cells with alpha particles. After irradiation, the cell survival can be determined using, for instance, a Resazurin assay. In this project, three shortcomings of the existing protocol developed in earlier work were identified and modified: (1) The cell sedimentation inside the hydrogels was improved, such that the embedded cells are within reach of the alpha particles, (2) the protocol was adjusted such that sample manipulations during the measurements are minimized which reduces the chance of disrupting or damaging the hydrogels and (3) the glass slides required in the sample preparation were provided with a coating to avoid gel rupture. Afterwards, with the modified protocol, two new cell-irradiation experiments were performed.

In the second part of this thesis, the focus will be on the development of a recoil-implantation generator that can be used for the production of isotopes for cell-irradiation experiments. Whenever an ^{225}Ac isotope decays on an ^{225}Ac implanted foil, the remaining daughter nucleus might recoil out of the foil as a result of conservation of momentum. The idea behind the recoil-implantation generator is to implant these recoiling ^{225}Ac daughter nuclei on an empty aluminium disk. In this project, a setup was constructed from scratch and two measurements were performed. In the first part of each measurement, an empty aluminium disk is placed in front of an ^{225}Ac implanted foil while in the second part the implanted disk is placed in front of a passivated implanted planar silicon (PIPS) detector to identify the collected daughter nuclei. Subsequently, an expression was derived to determine the efficiency of the recoiling process from the data obtained during both

measurements.

Summary for a General Audience

Whenever a patient is diagnosed with cancer, there is a wide variety of treatment options available. The choice for which treatment to use is typically dependent on the type of cancer and the cancer's stage. In the early stages, the tumor is typically well-localized and can be treated well. In later stages, the cancer has often spread to other body parts, which makes treatment much harder. Such cancers are referred to as metastatic cancers. Nowadays, whenever a patient is diagnosed with metastatic cancer, the survival rate following diagnosis is typically low. For example, of all patients diagnosed with metastatic breast cancer only 28% of all women (and 22% of all men) will still be alive after five years. This number drops to 7% for patients diagnosed with metastatic lung cancer [1]. However, in the last two decades, promising results have been observed in clinical trials using targeted alpha therapy (TAT) for treating metastatic cancers. In TAT, a radioactive element is attached to a molecule known to the body that will carry it towards the cancer cells by traveling along the natural pathways. The radioactive element will emit alpha particles, which is a type of radiation that causes high damage to cells, but has a very low penetration depth. Both these characteristics make TAT an extremely effective way of damaging cancer cells, while reducing the damage to healthy cells to a minimum. Even though the clinical trials look promising, TAT is nowadays not on a large scale clinically in use for cancer treatment. This is mainly due to (1) the high costs, (2) the availability and (3) the effects of the alpha-emitting sources that are not yet fully understood.

In the first part of this thesis, the focus will be on the further development of a protocol that can be used to study the effects of the alpha-emitting sources. The goal of this protocol is to study the impact of the alpha particles on the cancerous cells by externally irradiating a gel containing cells with alpha particles. In this project, three shortcomings of the existing protocol developed in earlier work were identified and modified: (1) The cell sedimentation inside the gels was improved, such that the embedded cells are within reach of the alpha particles, (2) the protocol was adjusted such that sample manipulations during the measurements are minimized which reduces the chance of disrupting or damaging the gels and (3) the glass slides required in the sample preparation were provided with a thin layer (i.e., a coating) to avoid gel rupture. Afterwards, with the modified protocol, two new cell-irradiation experiments were performed.

In the second part of this thesis, the focus will be on the development of a generator that can be used for the production of radioactive sources for cell-irradiation experiments. In a similar way compared to firing a gun, a radioactive nucleus will recoil as well upon emitting alpha radiation. Hence, in this project, an experimental setup was built from scratch in order to catch these recoiling nuclei such that new radioactive sources can be produced. Subsequently, an expression was derived to determine the efficiency of the recoiling process from the data obtained during the measurements.

Contribution Statement

The results presented in this thesis would not have been obtained without the aid of many people. Hence, I would like to dedicate this page to thank everyone for their help during the measurements.

First, for the results shown in chapter 1, I would sincerely like to thank Jake Johnson for the ^{241}Am source manipulations during the irradiation experiment.

Secondly, for the results in chapter 2, I would sincerely like to thank Lens Dedroog for operating the confocal microscope when investigating the cell sedimentation in both the 1.5 mg/mL and 2.0 mg/mL collagen hydrogels, the polyethylene glycol hydrogels and the hydrogels containing Matrigel. Moreover, I would also like to thank Lens for allowing me to use the linear storage moduli he measured such that I could compare the stiffness of the gels in a quantitative way.

Thirdly, for the results in chapter 3, I would sincerely like to thank Philippe Mispelter and the guys from the workshop for making the adjustments to the Teflon holders such that new irradiation experiments could be performed. Next, I would also like to thank Yovan de Coene for operating the multiphoton microscope when investigating the gel adhesion to the glass slides. Lastly, but definitely not least, I would like to express my gratitude to Olivier Deschaume for cleaning the glass slides in a piranha solution, providing the APTES and methacrylate-silane coated glass slides and adding the coatings while teaching me how to prepare them at the same time.

Subsequently, for the results shown in chapter 4, I would sincerely like to thank Jake Johnson, and Anita Candiello for taking over when Jake was abroad, for the ^{241}Am source manipulations during all the irradiation experiments. Moreover, I would also like to thank both Lens Dedroog and Jake Johnson for taking the evening shift such that the first data point in the final irradiation experiment (i.e., when the sample was irradiated for three hours) could be obtained on the same day.

Finally, for the results in chapter 5, I would sincerely like to thank Jake Johnson for all source manipulations regarding the implantation and detection part in both measurements. I also would like to thank Max Keppens for his help when building the experimental setup together from scratch and allowing me to use the energy calibration he obtained such that I could perform the data analysis straight away. Thirdly, I would like to thank Michael Heines for allowing me to use his code to determine the value of the geometric efficiency.

List of Figures

List of Tables

List of Commonly Used Acronyms and Abbreviations

APTES	3-Aminopropyltriethoxysilane
a.u.	Arbitrary units
Bq	Becquerel, a unit for the activity: 1 Bq = 1 decay/s
CERN	Conseil Européen pour la Recherche Nucléaire
DIRAC	Direct irradiation with alphas on cells
DMEM	Dulbecco's modified eagle medium
DPBS	Dulbecco's phosphate-buffered saline
DPP-PHA	Digital Pulse Processing for Pulse Height Analysis
DTT	Dithiothreitol
EDTA	Ethylenediaminetetraacetic acid
EHS	Engelbreth-Holm-Swarm
FBS	Fetal bovine serum
Gy	Gray, a unit for the absorbed dose: 1 Gy = 1 J/kg
HEPES	2-[4-(2-hydroxyethyl)-1-piperazinyl]ethanesulphonic acid
IKS	Institute for Nuclear and Radiation Physics
ISOLDE	Isotope separation on-line device
ISOL	Isotope separation on-line
LAP	Lithium phenyl-2,4,6-trimethylbenzoylphosphinate
LET	Linear energy transfer
MEM NEAA	Minimum essential medium non-essential amino acids
MEDICIS	Medical isotopes collected from ISOLDE
Pa	Pascal, a unit for the linear elastic (or storage) modulus: 1 Pa = 1 N/kg
PBS	Phosphate-buffered saline
PEG	Polyethylene glycol
PEGDA	Polyethylene glycol diacrylate
Pen Strep	Penicillin Streptomycin

PIPS	Passivated implanted planar silicon
PSMA	Prostate-specific membrane antigen
SHG	Second-harmonic generation
SRIM	Stopping and Range of Ions in Matter
TAT	Targeted alpha therapy
THG	Third-harmonic generation
TRT	Targeted radionuclide therapy
UV	Ultraviolet
wt%	Weight percentage

List of Commonly Used Symbols

e^-	Electron
$\overline{\nu_e}$	Electron antineutrino
Z	Number of protons
A	Mass number, i.e. the sum of the number of protons and number of neutrons. Not to be confused with the activity.
ν_e	Electron neutrino
γ	Photon
eV	Electronvolt
ω	(Angular) frequency
r	Radius of the circular trajectory of the ionised elements in the mass separator
v	Velocity of the ionised elements upon entering the mass separator
q	Electric charge of the ionised elements entering the mass separator
m	Mass of the ionised elements entering the mass separator
B	Magnitude of the magnetic field of the analyzing magnet
ΔV	Potential difference
R	Resistor
$A = A(t)$	The activity at time t, expressed in Becquerel (Bq)
$N = N(t)$	The number of nuclei present at time t
λ	The decay constant (i.e. the probability per unit time that a nucleus will decay). Not to be confused with the photon wavelength.
$N_0 = N(t = 0)$	The initial number of nuclei present at time $t = 0$
$A_0 = A(t = 0) = \lambda N_0$	The initial activity at $t = 0$, where λ is the decay constant
$t_{1/2}$	The half-life

ϵ_{Recoil}	The recoil efficiency
$A_{\text{Disk}}^{(\text{Bi-213})}(t)$	The activity on the aluminium disk at time t due to the ^{213}Bi present.
$A_{0,\text{Disk}}^{(\text{Bi-213})} = A_{\text{Disk}}^{(\text{Bi-213})}(t=0)$	The initial activity on the aluminium disk due to the ^{213}Bi present. The initial activity refers here to the activity at the start of the experiment, after implantation.
$A_{\text{Foil}}^{(\text{Ac-225})}(t)$	The activity on the foil at time t due to the ^{225}Ac present
$A_{0,\text{Foil}}^{(\text{Ac-225})} = A_{\text{Foil}}^{(\text{Ac-225})}(t=0)$	The initial activity on the foil due to the ^{225}Ac present. The initial activity refers here to the activity at the start of the experiment, after implantation.
$N_{0\rightarrow t_m}^{(\text{Bi-213})}$	The total number of ^{213}Bi isotopes that decayed during the measurement.
$A_{\text{Disk}}^{(\text{Po-213})}(t)$	The activity on the aluminium disk at time t due to the ^{213}Po present.
b_{β^-}	The β^--branching ratio in the decay of ^{213}Bi, which is equal to 0.979 (97.9%).
ϵ_{Geo}	The geometric efficiency
t_m	If the measurement started at $t = 0$, the measurement stopped at $t = t_m$
$C_\alpha^{\text{Po-213}}$	The number of alpha particles detected due to the decay $^{213}\text{Po} \longrightarrow {}^{209}\text{Pb} + {}^{4}\text{He}$ per unit time.
$N_{0\rightarrow t_m}^{(\text{Po-213})}$	The total number of alpha particles detected due to the decay of $^{213}\text{Po} \longrightarrow {}^{209}\text{Pb} + {}^{4}\text{He}$.
u	Atomic mass unit
S_0	Singlet ground state
S_n	n^{th} excited singlet state
T_n	n^{th} excited triplet state
λ	Photon wavelength
$\langle x \rangle$	Weighted mean
σ_i	Uncertainty on the i^{th} data point
$w_i = \frac{1}{\sigma_i^2}$	Weight factor corresponding to the i^{th} data point

Contents

"Let's start at the very beginning. A very good place to start."

Maria von Trapp – The Sound of Music

Introduction

When a patient is diagnosed with cancer, there is a wide variety of treatment options available. Examples of such treatments are surgery, chemotherapy, hyperthermia (i.e., where heat is used to damage cancer cells), etc [3]. The applicability of each treatment depends on the type of cancer and the cancer's stage.

One of the main cancer treatments currently utilized, is radiotherapy where ionizing radiation is used to damage and kill cancer cells. Victor Despeignes was in 1896 the first physician to make use of radiotherapy to treat a malignant tumor of a patient by irradiating it with x rays [4]. However, even though radiotherapy has been evolving for more than 125 years since it was used for the first time, the most common type of radiotherapy nowadays is still external irradiation of cancer cells with x rays and, to a much lesser extent, irradiation with particles such as protons, electrons, neutrons or carbon isotopes [5]. The main problem with external irradiation, is that the beam of ionizing radiation must travel through the healthy tissue first in order to reach the tumor. Consequently, the beam will not only deposit its energy in the tumor, but in the surrounding healthy tissue as well and thus resulting in additional ionization damage. One way to mitigate the dose[1] to healthy tissue, is to immediately place a small radioactive source inside or near the tumor. That way, the radiation does not need to travel through the healthy tissue to reach the cancer cells. This technique is called brachytherapy [7]. The radioactive sources typically used for brachytherapy have a relatively short half-life ($t_{1/2}$) and decay through β^--decay or by electron capture. Examples of such isotopes are ^{192}Ir ($t_{1/2} = 73.8$ days), ^{125}I ($t_{1/2} = 59.4$ days) or ^{103}Pd ($t_{1/2} = 17.0$ days) [8].

In β^--decay, a nucleus of element X with proton number Z and mass number A, decays to a nucleus of element Y with a lower energy state, emitting an electron (e^-) and an electron antineutrino ($\overline{\nu_e}$) in the process. This decay can be written as

$$ {}^{A}_{Z}X \quad \longrightarrow \quad {}^{A}_{Z+1}Y + e^- + \overline{\nu_e}. \tag{1} $$

Electron capture, on the other hand, is a process where an orbital electron (typically from the K-shell) is drawn into the nucleus. As a result, an electron neutrino (ν_e) is emitted and a lower energy configuration will be obtained. Both neutrinos and anti-neutrinos barely interact with matter and thus do not cause any damage to cancer cells. However, the isotopes selected for brachytherapy that decay through electron capture, decay towards an excited nuclear state which on its turn will decay towards a stable configuration through γ-decay or internal conversion. This decay can be written in a more compact form as

$$ \begin{aligned} {}^{A}_{Z}X + e^- \quad &\longrightarrow \quad {}^{A}_{Z-1}Y^* + \nu_e \\ &\longrightarrow \quad {}^{A}_{Z-1}Y + \gamma + \nu_e. \end{aligned} \tag{2} $$

[1] The dose refers here to the absorbed dose which is defined as the mean energy absorbed per unit mass from any type of radiation. The dose is typically expressed in Gray (Gy), where 1 Gy = 1 J/kg [6].

Here a photon (γ) is emitted in the process. In internal conversion, the emitted photon will cause an orbital electron to be ejected from its orbit. The asterisk written next to the daughter nucleus is to indicate the excited state. Because of the decays in Equation 2, the dose delivered to the patient will be due to x rays following the electron capture, electrons following the internal conversion in the subsequent decay or Auger electrons resulting in the subsequent cascade following the internal conversion.

However, the emitted electrons in β^--decay are still able to travel up to several centimeters deep (depending on the energy) in surrounding tissue. The emitted photons, as a consequence of the γ-decay or the emitted x rays, will travel even further in tissue. This means that even in brachytherapy healthy tissue is still damaged to some extent, especially when small tumors are irradiated [9]. Moreover, when a patient is diagnosed with metastatic[2] cancer, both external irradiation and brachytherapy are not suitable treatments due to the fact that these treatments are only suitable for solid and well-localised tumors. Even when additional treatments besides radiotherapy are offered to the patient, the survival rate when being diagnosed with metastatic cancer is still low. For example, of all patients diagnosed with metastatic breast cancer only 28% of all women (and 22% of all men) will still be alive after five years. This number drops to 7% for patients diagnosed with metastatic lung cancer [1]. However, in the last two decades, intensive research and clinical trials have been performed using targeted radionuclide therapy (TRT), which is a relative new technique that shows potential in treating metastatic cancers.

Targeted Radionuclide Therapy

In TRT, a radionuclide is attached to a vector and injected into the patient. The vector will travel along the circulatory and lymphatic system in the human body towards the cancer cells, while carrying the isotope. This basic principle behind TRT is shown more clearly in Figure 1.

[2]A metastatic cancer is a cancer that has spread to other parts of the body as a consequence of cells breaking off from the original tumor. These tumor cells can then be transported through the bloodstream or the lymph system to other parts of the body where new tumors can be formed. Consequently, metastatic cancers are thus not well-localised nor solid [1].

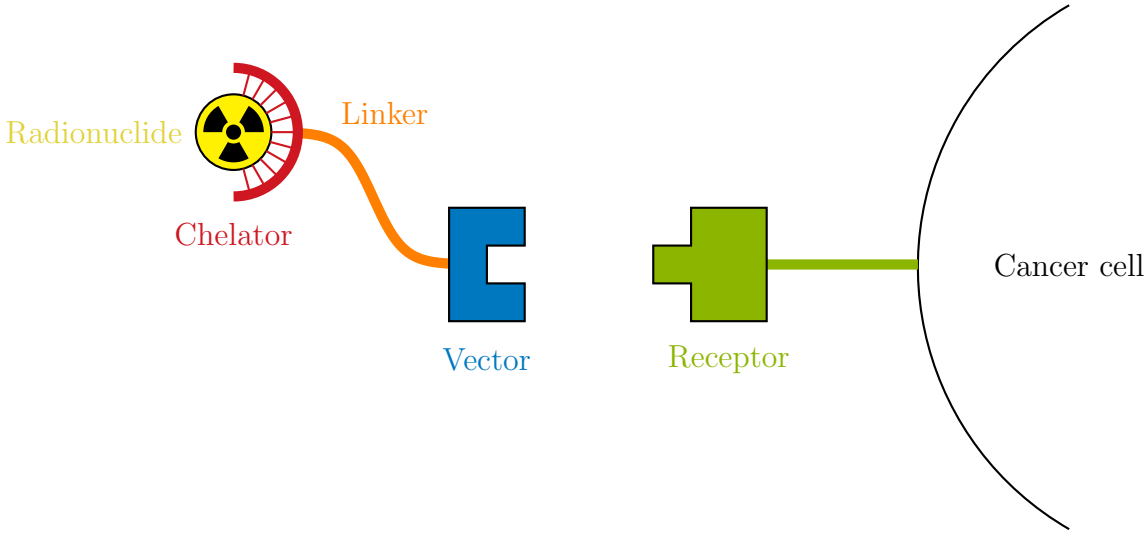

Figure 1: *Schematic illustration of the basic principle behind TRT. This illustration is based upon Figure 1(b) in [10].*

The radionuclide is bound to a bifunctional chelating agent (or chelator) that is in turn bound to a targeting vector. A chelating agent is a molecule where part of the molecule can form a bond with the radiometal while the other part of the molecule consists of a functional group that can covalently bind with the targeting vector. The chelator can be directly attached to the targeting vector, but often an additional linker is present in between the chelator and the vector to modify pharmacokinetics. In TRT, a variety of vectors are possible: It can either be a small peptide, a protein (such as for example an antibody) or a nanoparticle [10]. The choice of vector depends on the type of cancer the patient is diagnosed with. However, in recent years, a shift in interest from general TRT to targeted alpha therapy (TAT) has been observed as a result of promising results in preclinical and clinical trials [11].

TAT makes use of radionuclides that decay towards a lower energy configuration by emitting a ${}^{4}_{2}\mathrm{He}$ nucleus in the process. This decay is α-decay and can be written in a more compact form as

$$ {}^{A}_{Z}X \quad \longrightarrow \quad {}^{A-4}_{Z-2}Y + {}^{4}_{2}\mathrm{He}. \tag{3} $$

Alpha particles have a high linear energy transfer (LET), meaning that these particles transfer large amounts of energy to the surrounding medium per unit distance travelled inside this medium. The higher the LET of a particle, the more energy will be deposited to the surrounding medium and thus the faster the particle will slow down in this medium. Alpha particles are typically able to travel 50-100 μm inside human tissue, but the energy transferred per unit distance is much higher compared to electrons emitted in β^{-}-decay due to their high mass. More specific: An alpha particle emitted in alpha decay typically has an energy of approximately 4 MeV up to 9 MeV. As a result, the LET of such an alpha particle ranges from 50 keV/μm up to 200 keV/μm in human tissue. On the other hand, electrons emitted in β^{-}-decay have an energy of approximately 100 keV up to 1 MeV, resulting in a LET of approximately 0.06 keV/μm up to 0.15 keV/μm in human tissue [12, 13, 14]. Alpha particles thus cause much more damage to cancer cells compared to electrons emitted in general TRT as a result of β^{-}-decay. Electrons emitted in the decay of radioactive nuclei only cause limited ionization events resulting in single-

or double-stranded breaks in the DNA of the cancer cells that are often repairable and have a rather low probability of being lethal. Alpha particles, on the other hand, cause much more ionization events compared to electrons. As a result, alpha particles will cause multiple single- or double-stranded breaks in the DNA of cancer cells which are far more difficult to repair compared to a single break and thus resulting much more often in cell death. Hence, ionization events caused by alpha particles have a much higher probability of being lethal [15]. Moreover, due to the high LET and the fact that the range of the alpha particles (i.e., 50-100 μm) is only a few cell diameters in length, TAT makes it possible to damage and kill cancer cells with a high precision in an extremely effective way harming almost none of the surrounding healthy tissue [16].

Considerations to Take Into Account

In TAT, not only is the targeting vector of importance, but equally important is the interaction between the vector and the alpha-emitting radionucleus attached to it. For example, it is often challenging to find a suitable targeting vector that can maintain its biological properties while being irradiated by the source attached to it. Moreover, whenever an alpha-emitting source decays, a daughter nucleus remains with entirely different chemical properties compared to the parent nucleus. The daughter nuclei themselves are often alpha-emitting sources as well, resulting in more daughter nuclei. However, in practice, the different chemical properties of the daughter nuclei are often not even the major problem regarding the interaction between the targeting vector and the alpha-emitting source. The reason for this is that once a nucleus decays and emits an alpha particle in the process, the daughter nucleus will be pushed in the opposite direction as a result of conservation of momentum. The energy of the recoiling daughters is typically more than 1000 times higher compared to the binding energy of any chemical bond. This means that, in general, after a decay, the recoiling daughter will not be bound to the chelator (and thus to the targeting vector) anymore. Consequently, the recoiling daughter will become free from the targeting vector and might migrate away from the tumor where it can cause damage to healthy cells elsewhere in the body [17]. There are typically two solutions to avoid the distribution of daughter nuclei in the body of the patient.

The first solution is to choose an alpha-emitting source whose daughter nuclei have short half-lives (i.e., the order of milliseconds up to a couple of minutes). For example, the isotope ^{223}Ra is often utilized in TAT to palliate patients with bone metastasis. The ^{223}Ra will target the hydroxyapatite matrix in the bone[3], but the daughter nuclei of ^{223}Ra will not. However, due to the short half-lives of the daughter nuclei, the daughter nuclei will not even have the chance to migrate away from the tumor. Consequently, the daughter nuclei will deliver a high dose to the cancer cells as well, just like the ^{223}Ra parent nucleus, while only harming healthy cells in a limited way. [17].

The second solution, is the so-called nanogenerator approach where the alpha-emitting source is internalized in the targeting tissue or even in the cancer cells themselves. Consider for example the actinium isotope ^{225}Ac. One of the daughter nuclei of ^{225}Ac is the bismuth isotope ^{213}Bi which can be extremely radiotoxic for the patient. This means the distribution of ^{213}Bi, and other daughter nuclei of ^{225}Ac, in the body needs to be kept at

[3]TAT with ^{223}Ra is a special case of TAT in the sense that no vector is required to carry the isotopes to the cancer cells. ^{223}Ra is a calcium homologue so it naturally targets the hydroxyapatite.

a minimum. Hence, the radiopharmaceuticals containing ^{225}Ac make use of targeting vectors that transport the radioactive ^{225}Ac inside the cancer cells. As a result, the daughter nuclei will be contained inside the target tumor and thus maximizing their damage to the cancer cells while minimizing their damage to healthy tissue [17, 18, 19].

Over the years, many (pre)clinical tests were performed taken the above-mentioned considerations into account and it was concluded that ^{225}Ac, ^{211}At, ^{212}Bi, ^{213}Bi, ^{212}Pb, ^{223}Ra, ^{227}Th and ^{149}Tb showed the most potential for TAT [20, 21]. However, of the eight alpha-emitting sources that are listed here, only ^{223}Ra is commercially available. The radiopharmaceutical containing ^{223}Ra is often better known as Xofigo™ and is utilized for the treatment of castration-resistant prostate cancer with bone metastases [15, 21]. The remaining seven sources are currently not commercially available due to (1) the high production costs and (2) the availability. Consequently, it is not possible to use these alpha-emitting sources on a large scale for cancer treatment yet [19, 20]. Moreover, the effects of the alpha-emitting sources or the recoiling daughter nuclei on cancer cells are not yet fully understood and require further investigation. In this project, the focus will be on the actinium isotope ^{225}Ac.

Actinium-225

The actinium isotope ^{225}Ac shows potential for the treatment of bladder and prostate cancer, brain tumors (e.g., glioblastoma), neuroendocrine tumors and blood cancers (e.g., leukemia) [16, 22]. A more specific example of the potential of ^{225}Ac is demonstrated in Figure 2.

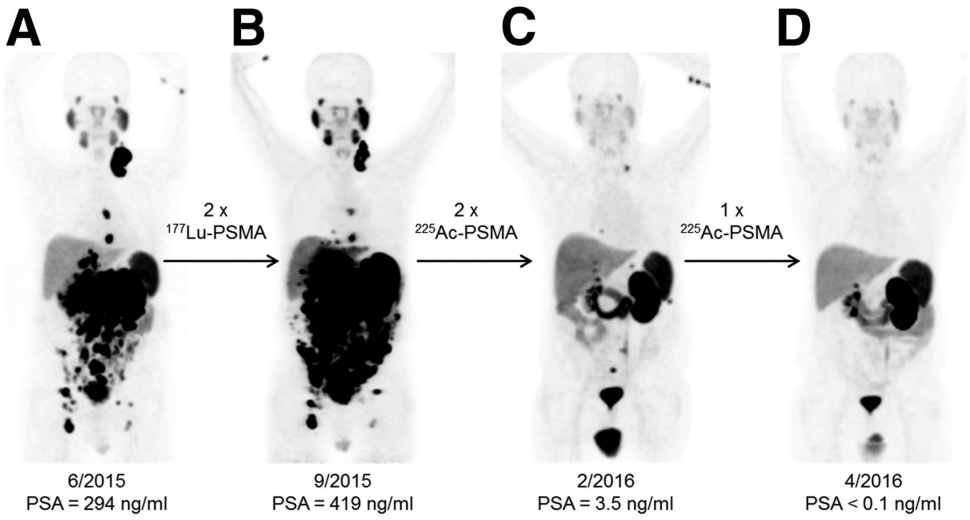

Figure 2: *An example illustrating the potential of ^{225}Ac for metastatic cancer treatment. The image shown here is a ^{68}Ga-PSMA-11 PET/CT scan of a patient that is diagnosed with peritoneal carcinomatosis and liver metastasis first following ^{177}Lu-PSMA radionuclide therapy, then after ^{225}Ac-PSMA therapy. Figure obtained from [23].*

A ^{68}Ga-PSMA-11 PET/CT scan of a patient diagnosed with peritoneal carcinomatosis[4] and liver metastasis is shown at different stages of treatment. At first, a conventional

[4]Peritoneal carcinomatosis is a form of cancer affecting the peritoneum. It is often the result of colorectal, gastric or gynaecological tumors that have spread in the body of the patient [24].

treatment was used where a β^--emitting source, ^{177}Lu, is attached to a prostate-specific membrane antigen (PSMA) as targeting vector and is injected into the body of the patient. Unfortunately, the tumor kept growing and no improvement can be observed upon comparing images A and B in Figure 2. In contrast, after applying a TAT treatment with ^{225}Ac, a clear improvement can be observed as can be seen in images C and D thus indicating the potential of ^{225}Ac.

However, even though the clinical trials with ^{225}Ac seem promising, further investigation is still required to make TAT with ^{225}Ac commercially available. For example, further investigation is necessary on the production side of ^{225}Ac such that larger quantities can be produced at lower costs. On the other hand, there are also still some unanswered questions on the radiobiology of TAT with ^{225}Ac. For example, the radiobiological effects of the recoiling daughter nuclei are not exactly known at this point. Nonetheless, it is important to know this to a much greater precision. That way, a more accurate dose can be delivered to the patient: An overestimation of the biological effects of the daughter nuclei would result in a dose that is too small for an effective cancer treatment, while an underestimation of the biological effects of the daughter nuclei would result in too much damage to the healthy tissue. Hence, the main focus of this project will be on the further development of a protocol that can be used to investigate the biological effects of the recoiling ^{225}Ac daughter nuclei by building on the work already established by Judith Vankeirsbilck in her internship in 2021 [25], Viktor Van den Bergh's master's thesis in 2022 [2] and Nathan Meurrens' honours project in 2023 [26].

The Goal of this Project

Judith Vankeirsbilck showed in 2021 during her internship at the Interdisciplinary Research Group at the Institute for Nuclear and Radiation Physics (IKS) in Leuven that it was not feasible from a practical point of view to measure the biological effect of the recoiling daughters directly [25]. This conclusion was based upon numerous SRIM (Stopping and Range of Ions in Matter) simulations. Hence, a different approach was required to measure the dose delivered by the recoiling ^{225}Ac daughters in an indirect way. However, due to the fact that the total dose delivered to a patient is the sum of the dose delivered by the emitted alpha particles and the dose delivered by the recoiling daughter nuclei, the dose of the recoiling daughter nuclei can be measured in an indirect way by subtracting the dose delivered by the emitted alpha particles from the total dose. As a result, an experimental endeavour was born to measure the dose delivered by the recoiling daughters of ^{225}Ac. The endeavour consists of multiple steps: First, the dose delivered by the emitted alpha particles will be investigated by externally irradiating cells embedded in a hydrogel[5] with ^{225}Ac. The cells are embedded in hydrogels in order to mimic tissues *in vitro*. Next, in the second step, the cells will be embedded in a hydrogel containing the ^{225}Ac isotopes to measure the total dose delivered to the cells inside the gel. Finally, in the third and last step, the total dose delivered will be remeasured where the ^{225}Ac isotopes are attached to a targeting vector such that the radioactive isotopes will be brought to

[5]Hydrogels are polymer networks in which the polymers are crosslinked with each other either chemically (i.e., by covalent bonds) or physically (i.e., by van der Waals forces, electrostatic forces, hydrogen bonds,...). The interstices in the polymer network of a hydrogel typically contain a considerable amount of water that is bound to the polymers [27, 28].

(or inside) the cells embedded in the hydrogel.

The first step of the above-mentioned experimental endeavour is currently in progress. In 2022, in his master's thesis, Viktor Van den Bergh laid the foundation of a protocol to externally irradiate cells embedded in a hydrogel in order to experimentally determine the cell viability after irradiation. Here the cell viability refers to the ratio of cells that are alive after irradiation compared to the total number of cells, meaning that

$$\text{Cell viability} = \frac{\#\text{ alive cells}}{\#\text{ alive cells} + \#\text{ dead cells}}. \tag{4}$$

Once the cell viability is known, it can be correlated to the dose delivered by the emitted alpha particles by using the Geant4 simulations developed by Nathan Meurrens in his honours project in 2023 at the Interdisciplinary Research Group at the IKS in Leuven [26].

The main focus of this thesis will be on the further development of the protocol developed by Viktor, which will be discussed in Part I. More specific, after having discussed each step of the cell-irradiation protocol in detail in chapter 1, three shortcomings of the protocol are identified near the end of this chapter. Hence, in chapter 2 and chapter 3, these shortcomings are more thoroughly investigated and a solution will be provided. Subsequently, in chapter 4, the results of two new cell-irradiation experiments will be show and discussed that were performed by utilizing the modifications provided in chapter 2 and chapter 3 to overcome these shortcomings. Lastly, in Part II, the production of radioactive isotopes that can be used for cell-irradiation experiments will be described.

Part I

Development of a Cell-Irradiation Protocol

"Success is 1% inspiration, 98% perspiration, and 2% attention to detail."

Phil Dunphy – Modern Family

1 The Cell-Irradiation Protocol

The focus of this first chapter will be on the cell-irradiation protocol developed by Viktor Van den Bergh to study the impact of alpha particles on cells. First, in section 1.1, an introduction on and global overview of the protocol will be provided. Subsequently, each step in the protocol will be discussed in detail starting in section 1.2 up to section 1.8. In the end, the goal of the cell-irradiation protocol is to quantify the impact of the alpha particles on cells in the subsequent days following irradiation by utilizing a Resazurin assay. Hence, in section 1.9 after having discussed the entire protocol, a fluorescence calibration will be provided. That way, the measured fluorescence intensities as function of time obtained from the Resazurin assays can be converted to the amount of cells that are alive after irradiation as a function of time. Lastly, in section 1.10, three shortcomings of the cell-irradiation protocol discussed in this chapter will be addressed.

1.1 Overview of the Cell-Irradiation Protocol

Studying and understanding the effects of both the alpha particles and recoiling daughter nuclei on cells is a complex endeavor. Hence, *in vitro* models are often utilized to mimic human tissue such that the complexity of the entire biological system can be reduced to a limited amount of aspects that can be probed in a controlled environment. Consequently, the main challenge when devising *in vitro* models is to obtain a model that is sufficiently complex to mimic real human tissue, yet simple enough such that the required aspects can be probed in a controlled way [29].

Viktor Van den Bergh laid in his master's thesis the foundation of an *in vitro* model to externally irradiate cells to study the impact of alpha particles. The cells that were utilized were HeLa cells, which is a cell line derived from cervical cancer cells [30]. In this model, the cells are embedded in a 1.5 mg/mL collagen hydrogel to mimic human tissue due to collagen being the most abundant protein in the human body [31]. Moreover, utilizing hydrogels also has a practical advantage as it allows to position HeLa cells in the top layer of the gel, within reach of the alpha particles, through sedimentation. This approach to position the cells in the top layer of the gel is more clearly shown in the

overview in Figure 1.1 where the protocol developed by Viktor Van den Bergh in his master's thesis to prepare and irradiate the embedded cells is illustrated.

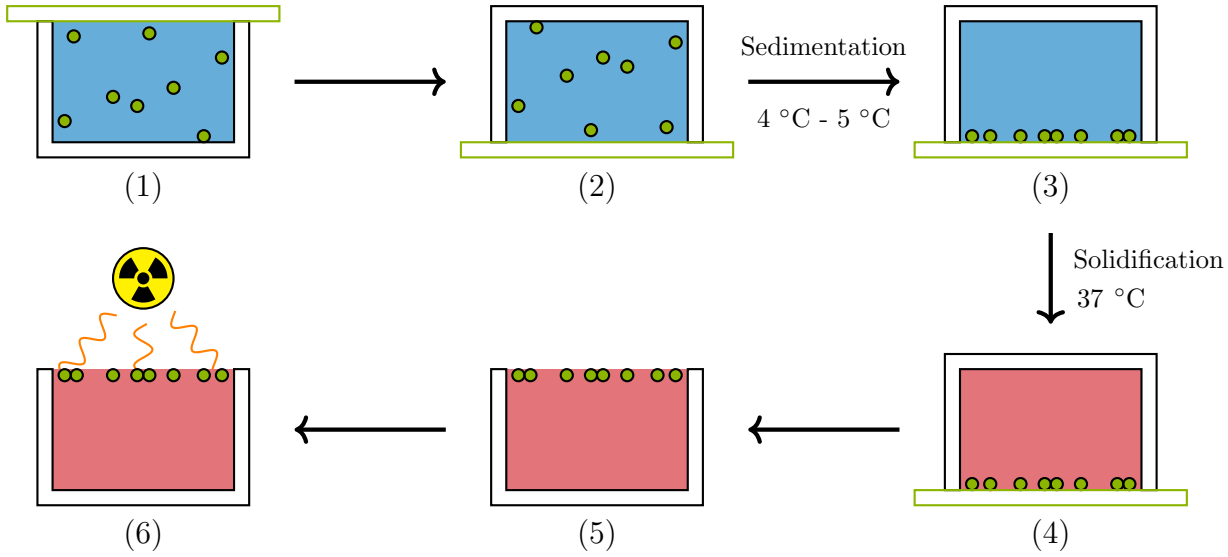

Figure 1.1: *A schematic illustration of all the steps in the protocol developed by Viktor Van den Bergh during his master's thesis to externally irradiate cells that are embedded in a hydrogel. The blue color indicates a solution, while the red color indicates a gel. The cells are illustrated in green. Due to the limited range of alpha particles in air, the source needs to be placed as close as possible near the gel.*

The first step in the protocol is the preparation of a solution in which the to-be-irradiated cells are embedded. The choice was made to prepare the gels with a concentration equal to 10^6 cells/mL such that the results of multiple irradiation experiments can be compared to each other. A cell concentration equal to 10^6 cells/mL is also the most commonly used cell concentration in *in-vitro* experiments. However, the higher the cell concentration, the harder the cell manipulations and the greater the impact of the cells on the material in which they are embedded. For example, when a concentration near 10^7 cells/mL is reached, the properties of the material in which the cells are embedded start to alter due to the high number of cells present. Subsequently, the cells inside the solution will be externally irradiated with alpha particles. However, due to the limited penetration depth of the alpha particles in the gel (i.e., ≈ 50 μm), the cells need to be in the top layer because otherwise the alpha particles will not be able to reach them. Hence, before the crosslinking inside the solution in which the cells are embedded is complete, and a polymer network is formed such that a gel is obtained, the sample is flipped upside down (step two) and placed inside a fridge at 4 °C - 5 °C. That way, due to the low temperature, the crosslinking in the solution will be delayed such that the cells inside the solution are able to sediment towards the bottom without being hindered by the crosslinks formed (step three). After the cells are sedimented, the solution is taken out of the fridge and placed inside an incubator at 37 °C to accelerate the crosslinking. Once the crosslinking is complete and a gel is formed (step four), the sample is flipped upside-down again (step five) and can be irradiated (step six) because now all cells will, in theory, be in the top layer within reach of the alpha particles.

In the subsequent sections, each step in protocol illustrated in Figure 1.1 will be

discussed in detail for a general hydrogel and will not be limited due to 1.5 mg/mL collagen gels only. The reason for this is that the same steps can and were used in this project for different hydrogels besides the 1.5 mg/mL collagen gels.

The first step in the protocol is the preparation of an initial cell solution that will be used to prepare the hydrogels with. That way, a hydrogel with a concentration equal to 10^6 cells/mL can be obtained. More details on the preparation of this initial cell solution will be given in the next section.

1.2 Preparation of the Cell Solution

The preparation of the initial cell solution always started from an existing HeLa cell culture, in a 25 cm^2 cell culture flask, that is obtained by following the steps described in this section. The cell culture flasks that were used in this project, were made from transparent polystyrene and consisted of a vented cap combined with a 0.22 μm hydrophobic filter. The filter allows gas exchange, but reduces the risk of contamination to a minimum [32].

First, the nutrient medium already present in the flask is removed to dispose of cellular waste products and dead cells. For further reference on the nutrient medium that was used in this project, see Appendix A. Next, all sides of the flask, but especially the bottom where the cells are located, are gently washed with 5 mL of Gibco™'s Dulbecco's phosphate-buffered saline (DPBS). DPBS is a balanced salted solution that maintains both the pH and the structural and physiological integrity of cells such that the risk of an osmotic shock is kept at a minimum [33, 34]. After removing the DPBS from the flask as well, 250 μL of Gibco™'s Versene solution is added. Versene is an ethylenediaminetetraacetic acidic (EDTA) solution which removes calcium ions from adhesion proteins and thus disrupts cell adhesion. The Versene solution that was utilized in this project contained 0.2 g EDTA(Na_4) per liter of phosphate-buffered saline (PBS) [35, 36, 37]. After incubating the cell culture flask for 2 - 3 minutes at 37 °C to accelerate the effect of the Versene, 5 mL of new nutrient medium (see Appendix A) is added to the flask. Subsequently, the nutrient medium and the Versene inside the flask are roughly flushed by pipetting the solution multiple times in and out the pipette to make sure all cells inside the flask are detached from each other and from the bottom. Next, 5 mL of the cell solution is removed from the flask:

- 4 mL of the cell solution is added to a new and empty plastic test tube. The cell solution inside this tube will be used to prepare the gel.
- 1 mL of the cell solution is added to a new and empty cell culture flask together with 4 mL of the nutrient medium discussed in Appendix A. This new flask is placed inside an incubator at 37 °C and will serve as the new cell culture flask to start from for the preparation of a new initial cell solution.

Even when no experiment in particular was performed, the cells were split each week by following the above-mentioned procedure.

When an irradiation experiment is performed, the concentration of the cell solution is required such that the right amount of cell solution can be mixed with the gel solution to obtain hydrogels with a concentration equal to 10^6 cells/mL. That way, the results of multiple irradiation experiments can be compared to each other. In the next section it will be explained how the cell concentration was determined.

1.3 Determining the Cell Solution Concentration

To determine the cell solution concentration, a hemocytometer, as shown in Figure 1.2, was used.

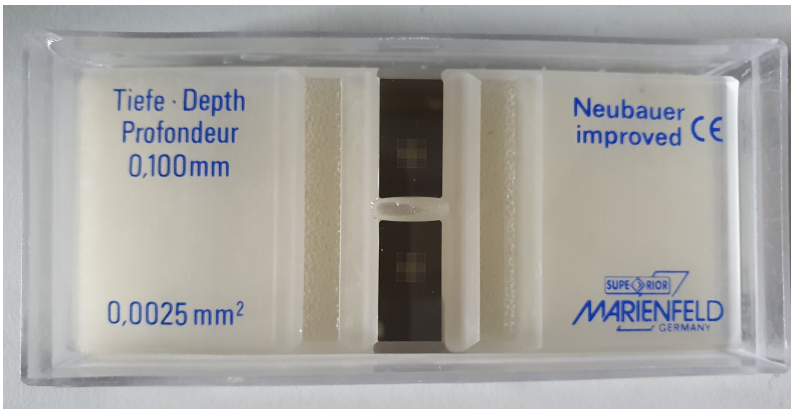

(a)

(b)

Figure 1.2: *A top view image and an illustration of the cross section of the hemocytometer that was used in this project. The small red rectangle in (b) indicates a cover glass that is placed on top of the hemocytometer.*

In the middle of the hemocytometer, on top of the plateau indicated in blue in Figure 1.2b, two identical 3 mm × 3 mm squares are engraved of which one is utilized to determine the cell concentration of the solution. An illustration of a single 3 mm × 3 mm square is given in Figure 1.3 [38, 39].

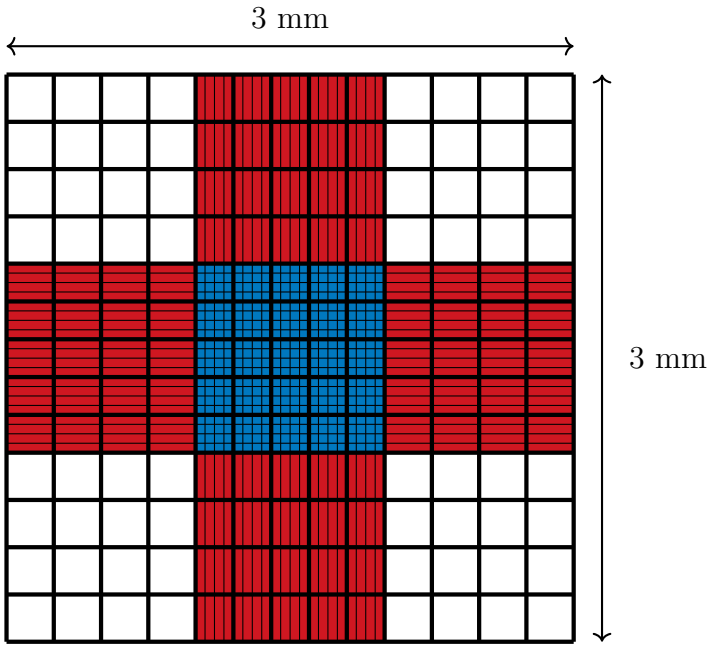

Figure 1.3: *Illustration of a 3 mm × 3 mm grid engraved in the middle of the hemocytometer that was used to determine the concentration of the cell solution.*

Each 3 mm × 3 mm grid consists of

- four 1 mm × 1 mm grids which on their turn are made out of sixteen 0.25 mm × 0.25 mm grids (indicated in white in Figure 1.3) [38, 39].
- four 1 mm × 1 mm grids which on their turn are made out of twenty 0.25 mm × 0.20 mm grids (indicated in red in Figure 1.3) [38, 39].
- one 1 mm × 1 mm grid which is made out of twenty-five 0.20 mm × 0.20 mm grids. Each 0.20 mm × 0.20 mm grid is on its turn made out of sixteen 0.05 mm × 0.05 mm grids (indicated in blue in Figure 1.3) [38, 39].

When pipetting 10 μL of a solution into one of the grooves indicated in green in Figure 1.2b, the entire volume between the plateau indicated in blue and the cover glass indicated in red will be filled as a result of capillary action [39]. The distance between the small plateau and the cover glass is exactly 0.1 mm. Hence, the cell solution volume above any square in the grid illustrated in Figure 1.3 can exactly be calculated. The solution that is pipetted into one of the grooves indicated in green in Figure 1.2b will be a ten-times diluted version of the cell solution in the plastic test tube. That way, less cells need to be counted to obtain the concentration.

The next step is the cell counting using a microscope. HeLa cells typically have a radius approximately equal to 10 μm [40, 41]. Hence, only the white squares in Figure 1.3 will be considered to count the cells because the blue squares or red rectangles would be too small to count appropriately. The small blue squares in the grid are typically used for smaller cells such as, for example, bacterial cells which have approximately a radius equal to 1 μm [41].

As a rule of thumb, only the cells located inside and on the upper or right side of the 0.25 mm × 0.25 mm square were considered. For example, seven cells can be seen either

inside the square or on one of the edges in the illustration shown in Figure 1.4. In this example, only the cells indicated in red and blue would be counted, meaning that this square only contains five cells, not seven.

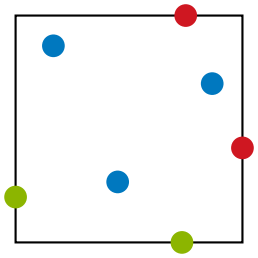

Figure 1.4: *Illustration of a 0.25 mm × 0.25 mm grid where seven cells can be seen either inside the square or on one of the edges. Applying the rule of thumb in this example, only five cells are counted, not seven.*

Subsequently, the number of cells in each of the white squares were counted and a mean value N was determined. The uncertainty associated to N was the greatest of the standard error on the mean of the four calculated values, or the error on the mean calculated assuming Poisson statistics.

Finally, due to the fact that the distance between the plateau indicated in blue and the coverglass indicated in red in Figure 1.2b is equal to 0.1 mm as stated earlier, the total cell solution volume above a single white 1 mm × 1 mm square is equal to 0.1 mm^3. Hence, the total cell concentration of the solution can be calculated as

$$\begin{aligned} \#\ \text{cells/mL} &= \frac{N \cdot d}{0.1}\ \text{cells/mm}^3 \\ &= N \cdot d \cdot 10^4\ \text{cells/mL}. \end{aligned} \tag{1.1}$$

As stated earlier, the cell solution was diluted ten times hence $d = 10$ in this project.

1.4 Sample Preparation

Once the initial cell solution is ready and its concentration is known, four samples were prepared in total: Two samples that will be irradiated and two control samples. The reason why two additional control samples are required, is to make sure the cells inside the gel are dying due to alpha irradiation and not due to external causes such as for example dehydration. All four samples were prepared in a Teflon holder shown in Figure 1.5.

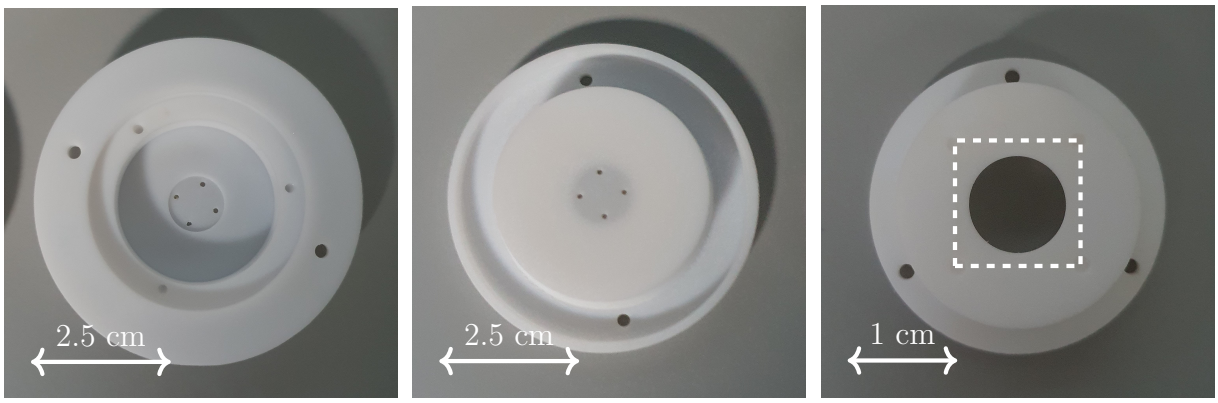

(a) **(b)** **(c)**

Figure 1.5: *Pictures illustrating the two parts of the Teflon holder. The front and back of the larger part is shown in respectively (a) and (b). The smaller part, which fits on top of the larger part, is shown in (c). The dashed white square indicates where a 170 micron thick glass slide is placed when assembling the Teflon holders (see subsection 1.4.1).*

1.4.1 Cell Sedimentation

The first step in the sample preparation, is to place a small, square and 170 micron thick glass slide on the dashed, white square that is indicated in Figure 1.5c. The larger part of the Teflon holder, shown in Figure 1.5a and Figure 1.5b, is then placed on top of the smaller part such that the glass slide is located in between both parts of the holder. Next, both the larger and smaller part are turned upside down such that three small screws can be inserted in the three holes visible in Figure 1.5c. The three screws are then tightened to make sure the larger and smaller part of the Teflon holder are firmly attached to each other with the glass slide in between them. In the next step, the Teflon holder is again turned upside down such that the four small holes in the middle (see Figure 1.5b) are visible when observing the Teflon holder from above. Once all four Teflon holders are assembled in this way, the gel solution is mixed with part of the initial cell solution (see section 1.2) such that a total concentration of 10^6 cells/mL is obtained. Throughout this project, four different hydrogels were prepared, each in a different way depending on the experiment. Hence, more details on the gel preparation will be provided when each of the experiments are discussed in detail[1]. Subsequently, through the four small holes in the larger part of the Teflon holder, part of the gel solution mixed with the initial cell solution is pipetted into the holder in two steps: First, 100 μL is pipetted into one of the four small holes which mainly fills the volume enclosed by the small glass slide and the larger part of the Teflon holder underneath the four holes. Secondly, an additional 100 μL is added on top to make sure each of the four holes is covered. In the next step, a plastic cover is placed on top of the Teflon holders such that they can be placed inside a fridge at 4 °C - 5°C. An illustration of the sample after placing it in the fridge is given in Figure 1.6.

[1]This will be in section 1.10, where the gel preparation will be discussed in subsection 1.10.1, and in chapter 2 where the gel preparation will be discussed in subsection 2.4.1.

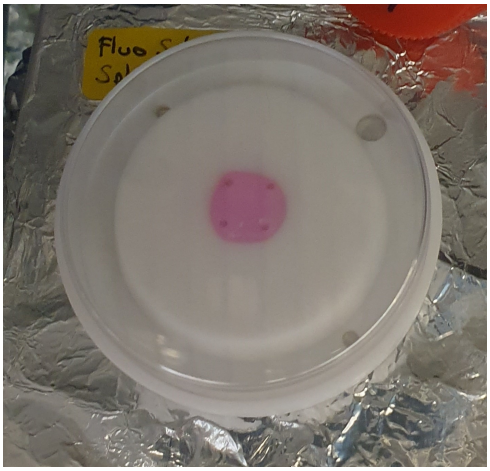

Figure 1.6: *Top view of a Teflon holder that has been placed in the fridge after pipetting 100 μL of the solution in one of the holes, an additional 100 μL on top of the holes and placing a plastic cover on top of it. That way, the cells embedded in the hydrogel solution can sediment towards the glass slide in between both parts of the holder without being hindered by the crosslinks formed. The pink dot at the center of the image is the 100 μL that was pipetted on top to cover all four holes.*

At this point in the sample preparation, the solution pipetted in the Teflon holder is still a liquid. The Teflon holders remain in the fridge at 4°C - 5°C for 1.5 hours to delay the crosslinking, allowing the cells to sediment towards the bottom (i.e., towards the glass slide in between the larger and smaller part of the Teflon holder). The less crosslinks formed in the gel, the better the cell sedimentation. If the cell sedimentation is unsuccessful, and the cells are as a consequence not positioned in the bottom layer near the glass slide, the alpha particles would not be able to reach the cells inside the gel due to their limited range.

After 1.5 hours refrigeration, the Teflon holders are placed inside an incubator at 37 °C for an additional 1.5 hours. That way, the crosslinking inside the solution is accelerated such that a gel is formed.

1.4.2 Before Irradiation

Once the gels remained in the incubator for 1.5 hours, two additional steps need to be taken to make sure the cells are (1) within reach of the alpha particles and (2) do not dehydrate while being irradiated.

First, the samples need to be flipped upside down such that the three small screws are again visible from above. That way, 8 mL of the nutrient medium discussed in Appendix A can be added into the upside-down plastic cover to make sure the cells in the gel do not dehydrate while being irradiated. In a subsequent step, the three screws are removed from the to-be irradiated sample together with the smaller part (i.e., the part shown in Figure 1.5c). Once the smaller part is removed, the small glass slide in between both parts of the Teflon holder is carefully removed as well using tweezers. In theory, all cells sedimented towards the bottom (i.e., near the small glass slide) as a consequence of placing the Teflon holders in the fridge, meaning that the cells should be in the top layer of the gel once the sample is turned upside down and the glass slide is removed. An illustration of the sample and a close up of the gel are shown in Figure 1.7.

(a) **(b)**

Figure 1.7: *The illustration in (a) shows the larger part of the Teflon holder that is placed in nutrient medium (indicated in blue) to avoid cell dehydration. An illustration of how the cells (indicated in green) should be positioned in the gel (indicated in red) after sedimentation is shown in (b). Both images only serve as an illustration and are not drawn to scale.*

Both the control sample and the sample that will be irradiated are placed in 8 mL of nutrient medium, but only the glass slide and smaller part of the to-be-irradiated sample are removed because otherwise the alpha particles will not be able to reach the cells due to the presence of the glass slide. Both of these parts are not removed from the control sample to avoid cell dehydration.

1.5 Experimental Setup

Both samples are ready for an irradiation experiment once the glass slide and smaller part of the holder are removed from the to-be-irradiated sample and both samples are placed in 8 mL of nutrient medium.

The experimental setup that was used in this project to irradiate all samples, was the Direct Irradiation with Alphas on Cells (DIRAC) setup developed in Viktor Van den Bergh's master's thesis [2]. A picture and an illustration of the setup is respectively shown in Figure 1.8a and Figure 1.8b. In each experiment, the source was brought as closely as possible to the gel.

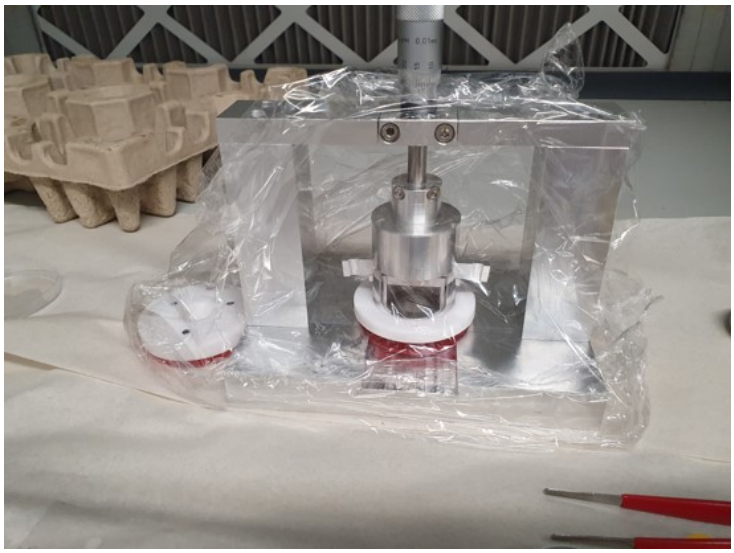

(a)

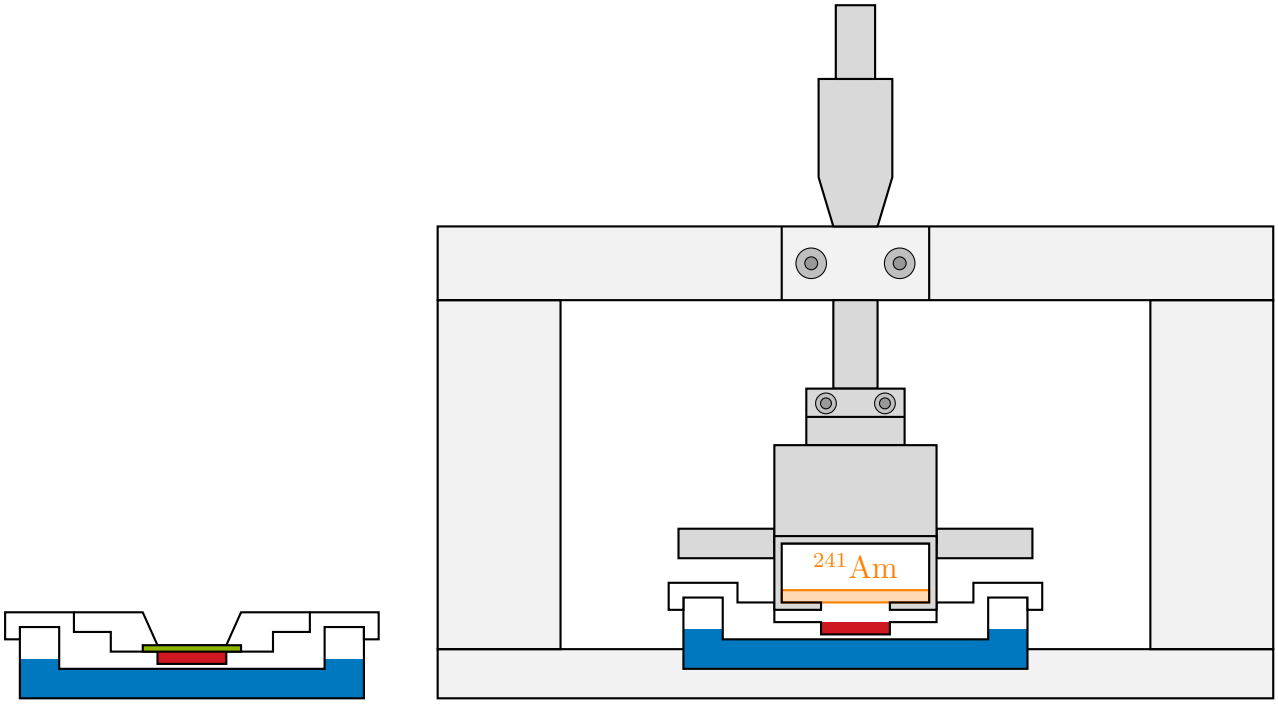

(b)

Figure 1.8: *A picture and an illustration of the DIRAC setup showing both the irradiated sample and the control sample. In the illustration in (b), the gel is indicated in red, the nutrient medium in blue, the ^{241}Am source in orange and the small glass slide in between the smaller and larger part of the Teflon holder is indicated in green in the control sample. However, in reality, both the gel and the nutrient medium share the same color. Hence, in order to distinguish both of them in the illustration in (b), the nutrient medium is deliberately indicated in blue while in the picture in (a) the nutrient medium has a red color. The image in (b) only serves as an illustration of the setup and is not drawn to scale.*

The plastic foil wrapped around the setup, as shown in Figure 1.8a, is to make sure cell dehydration is kept at a minimum, yet maintaining a limited air flow in order to avoid condensation on the source. As indicated in Figure 1.8b, an ^{241}Am[2] source was used to irradiate the gels instead of an ^{225}Ac source. The reason for this is due to the availability and convenience of handling semi-open ^{241}Am sources. That way, there is no extra hazard of recoiling daughters that should be taken into account. However, due to the fact that the main goal of this project is the optimization and further development of the cell-irradiation protocol, it does not make a difference whether an ^{225}Ac source or an ^{241}Am source is used in this stage of the project.

The ^{241}Am americium isotope decays by alpha decay with the two most intense alpha particle energies being 5485.560(120) keV and 5442.800(130) keV with intensities 84.80(50)% and 13.10(30)% respectively. However, as a result of the decay of ^{241}Am, not only alpha particles are emitted, but low-energy gamma rays are emitted as well. The two most prominent low-energy gamma rays have energies of 13.9 keV and 59.5409 keV[3]

[2]The same ^{241}Am source was used for each cell-irradiation experiment throughout this project. This source had an initial activity of 8010 Bq on 30/11/2022.

[3]The reference that was consulted did not mention an uncertainty on these two energy values [42].

with an intensity respectively equal to 37.10(30)% and 35.90(40)% [42].

1.6 Procedure After Irradiation: The Resazurin Assays

In each cell-irradiation experiment, one sample was irradiated for one hour and one sample for thirty minutes such that the impact of different irradiation times on the cells could be probed as well. Both irradiations were performed back-to-back. The first sample was irradiated for one hour. After irradiation, both gels from the irradiated and control sample were carefully removed from the Teflon holder and were then added to a different well of a twelve-well plate, made from transparent polystyrol, containing 1 mL of the nutrient medium discussed in Appendix A. Well A1, as indicated in Figure 1.9, contains the gel that was irradiated for one hour. Well A2 contains the gel that served as a control during the irradiation that lasted for one hour.

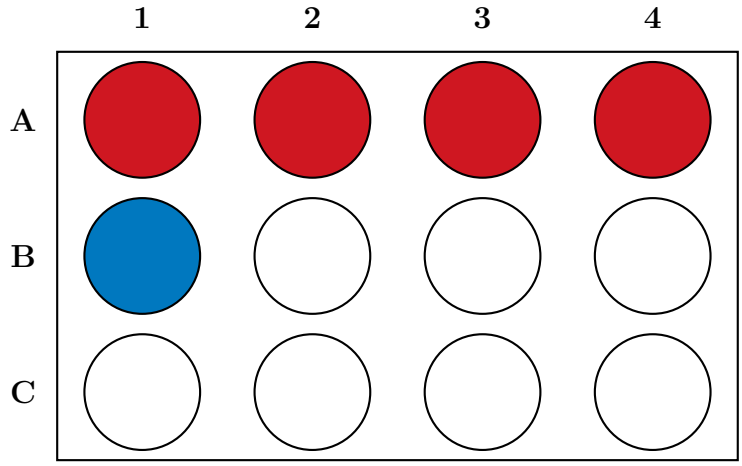

Figure 1.9: *Illustration of the twelve well plate that was used to store each gel after irradiation. Well A1 and A2 both contain 1 mL of nutrient medium together with respectively the gel that was irradiated for one hour and the corresponding control gel. After irradiating the second sample, the nutrient medium was removed from both these wells such that 1 mL of a ten-times diluted Resazurin solution could be added to each well in either red or blue to perform the Resazurin assays. The gel that was irradiated for thirty minutes and the corresponding control sample were then added to respectively well A3 and A4. The well indicated in blue only contains 1 mL of the ten-times diluted Resazurin solution and serves as a reference.*

The twelve-well plate, containing both gels, was then placed inside an incubator at 37 °C. Subsequently, the second sample and the corresponding control sample were prepared as described in subsection 1.4.2 such that the second sample could be irradiated for thirty minutes. Once the second sample is irradiated for thirty minutes, the nutrient medium from wells A1 and A2 is carefully removed using a pipette without removing the gel inside the wells. Subsequently, 1 mL of a ten-times diluted Resazurin solution with FluoroBrite™, required for the Resazurin assays that will be discussed in the next paragraph, is added to wells A1, A2, A3, A4 and B1 afterwards. The gel that was irradiated for thirty minutes

was then added to well A3 and the control sample corresponding to this measurement was added to well A4. Well B1, the one indicated in blue in Figure 1.9, served as a reference. It only contained 1 mL of the Resazurin solution but no irradiated gel nor a gel that served as a control.

Resazurin is a poorly fluorescent dye, but metabolic active cells reduce Resazurin to the highly fluorescent dye Resorufin [43]. Consequently, the more cells alive in a gel, the more Resazurin will be reduced to Resorufin. The number of cells in a gel is proportional to the amount of Resorufin. Moreover, each amount of Resorufin contributes to the total fluorescence intensity. Hence, the higher the amount of Resorufin, the higher the fluorescence intensity, meaning the amount of Resorufin is also expected to be proportional to the fluorescence intensity. In conclusion, it is found that the amount of cells alive in a gel is proportional to the measured fluorescence intensity:

$$\begin{aligned} \#\text{ Alive cells} &\propto \text{Amount of Resorufin} \\ &\propto \text{Fluorescence intensity.} \end{aligned} \tag{1.2}$$

Once the ten-times diluted Resazurin solution is added, the twelve-well plate shown in Figure 1.9 is placed inside an incubator at 37 °C for three hours in order to accelerate the conversion of the poorly fluorescent dye Resazurin to the highly fluorescent dye Resorufin by metabolic active cells. Once the twelve-well plate remained in the incubator for three hours, three times 100 μL is pipetted out of each well into a new 8×12 microplate as indicated in Figure 1.10. The microplate that was used for this project was a Greiner 96 microplate made from transparent polystyrol.

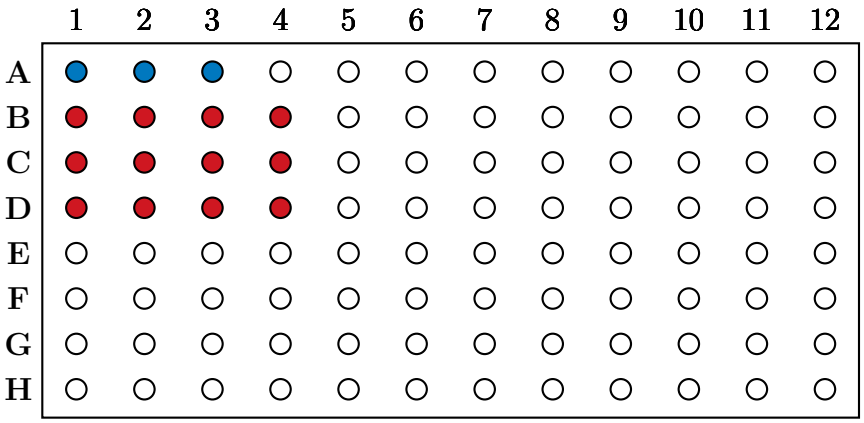

Figure 1.10: *Illustration of the* 8×12 *microplate that was used to measure the fluorescence intensity. Each well indicated in either red or blue contains 100 μL from a well in Figure 1.9.*

First, 100 μL of the solution in well B1 from the microplate illustrated in Figure 1.9 is pipetted in wells A1, A2 and A3 from the microplate shown in Figure 1.10. Next,

- 100 μL of the solution in well A1 from the microplate illustrated in Figure 1.9 is pipetted in wells B1, C1 and D1 from the microplate shown in Figure 1.10,
- 100 μL of the solution in well A2 from the microplate illustrated in Figure 1.9 is pipetted in wells B2, C2 and D2 from the microplate shown in Figure 1.10,

- 100 μL of the solution in well A3 from the microplate illustrated in Figure 1.9 is pipetted in wells B3, C3 and D3 from the microplate shown in Figure 1.10,
- 100 μL of the solution in well A4 from the microplate illustrated in Figure 1.9 is pipetted in wells B4, C4 and D4 from the microplate shown in Figure 1.10.

Subsequently, the fluorescence intensity of each well was measured using a fluorometer. The fluorometer emitted ten flashes of light with a wavelength equal to 540 nm (and a bandwidth of 9 nm). Part of the emitted photons were then absorbed by the solution in the wells which resulted in the emission of fluorescence photons with a wavelength equal to 590 nm (and a bandwidth of 20 nm). For further reference on fluorescence, fluorescence photons and the associated bandwidth, see Appendix B. The measured fluorescence intensity of the three wells corresponding to each of the prepared samples, and the blanco, where then combined into a single mean value. A statistical uncertainty was then deduced by calculating the standard deviation divided by the square root of three (i.e., the number of repeated measurements).

The remaining Resazurin solution in each well of the twelve-well plate was removed afterwards using a pipette and 1 mL of the nutrient medium discussed in Appendix A was added instead to each well that contained a Resazurin solution. The well plate was then placed in an incubator at 37 °C. In the subsequent days following irradiation, the same procedure can be repeated multiple times to probe the impact of the alpha particles on the cells over time, as indicated in the overview shown in Figure 1.11.

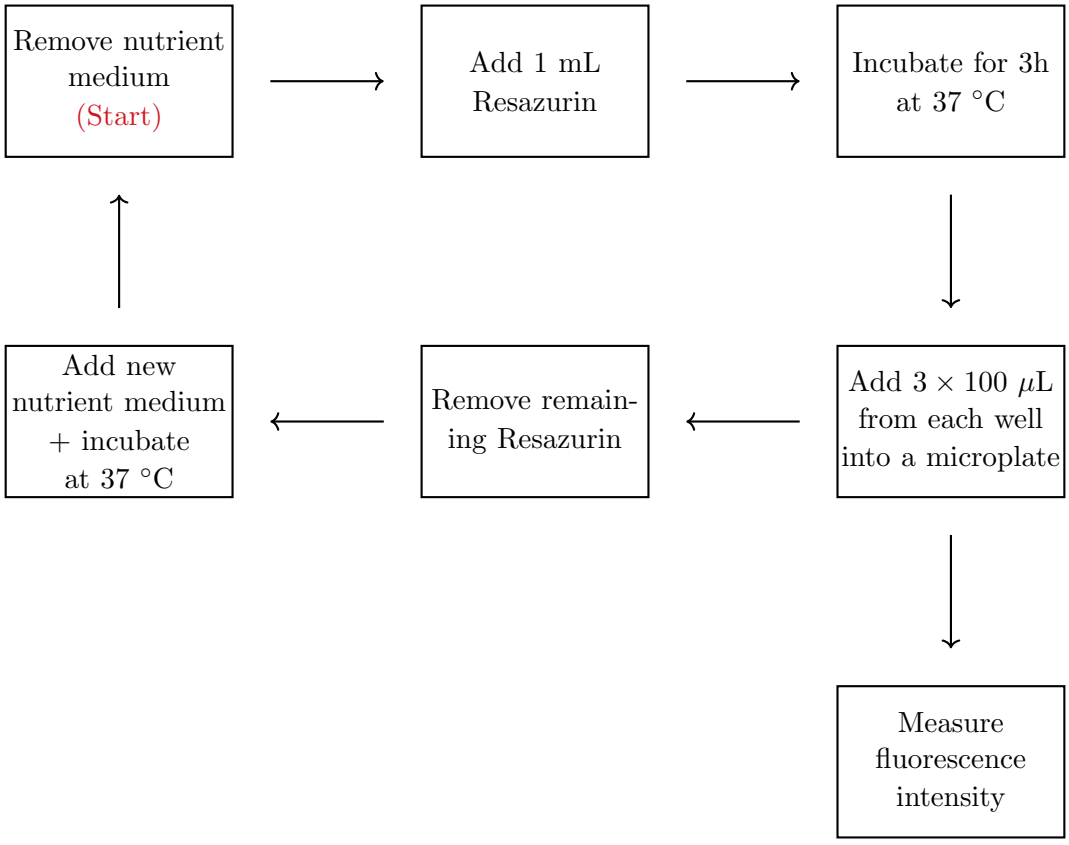

Figure 1.11: *An overview illustrating the required steps to perform the Resazurin assays.*

1.7 Summary of the Cell-Irradiation Protocol

The Resazurin assays discussed in the previous section conclude the cell-irradiation protocol. A flowchart summarizing each step in the protocol discussed in this chapter is provided in Figure 1.12.

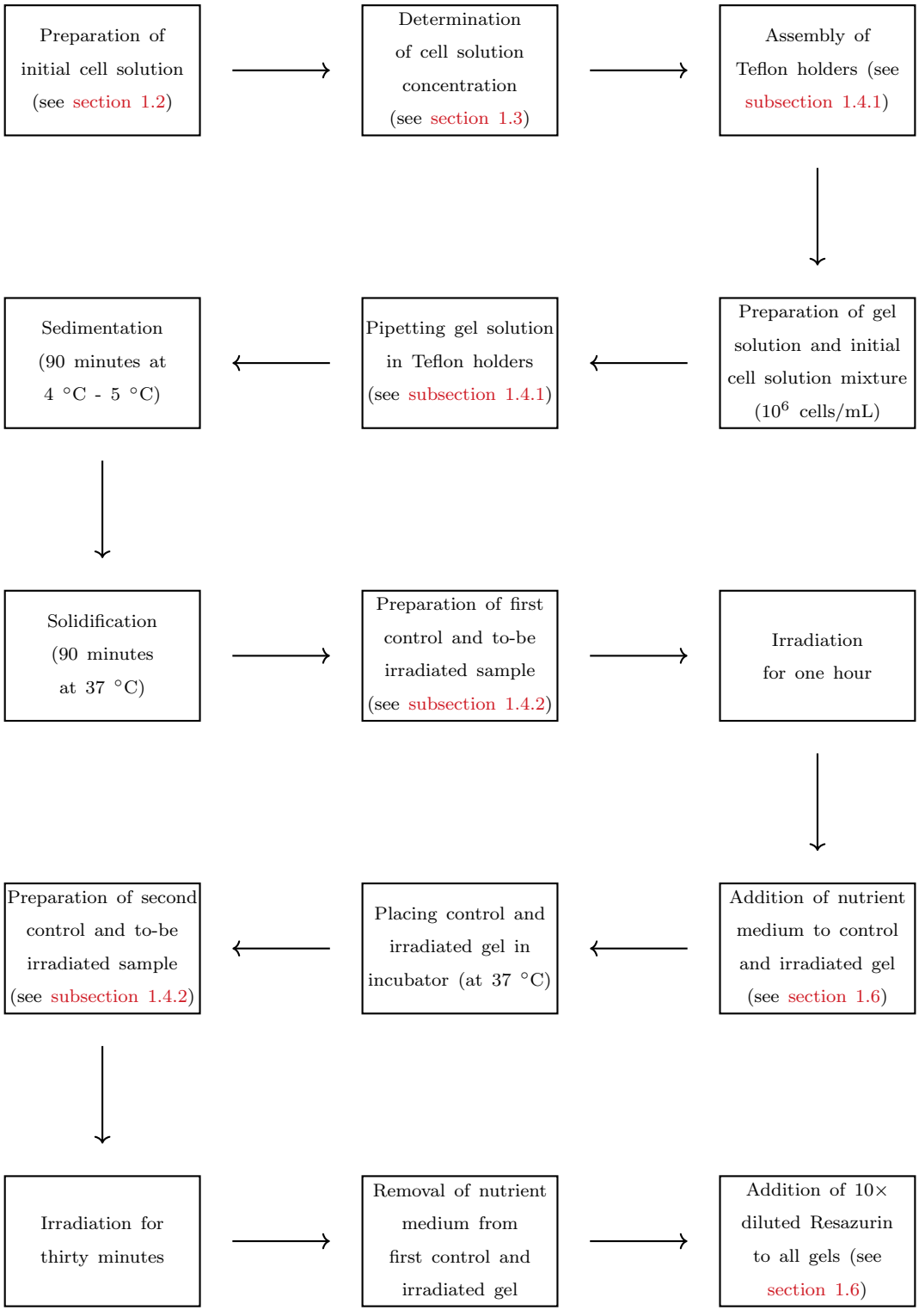

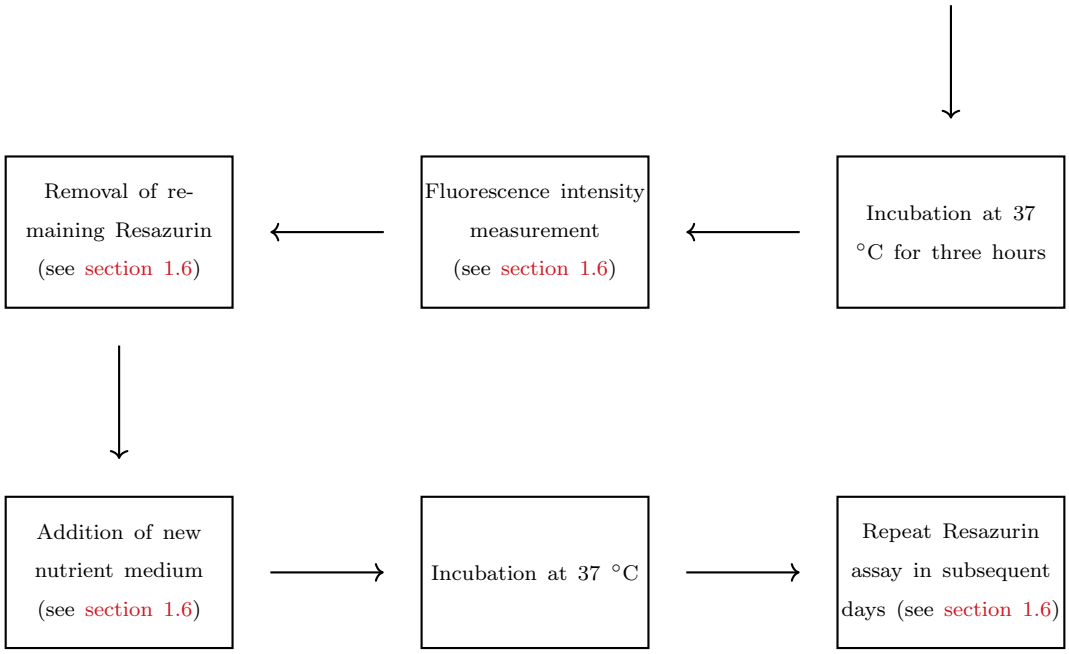

Figure 1.12: *A flowchart summarizing each step in the cell-irradiation protocol.*

1.8 Expected Results

Once multiple Resazurin assays are performed, and thus the fluorescence intensity of both the irradiated and control gels are probed over time, a graph similar to the one illustrated in Figure 1.13 is expected after approximately eight or nine days.

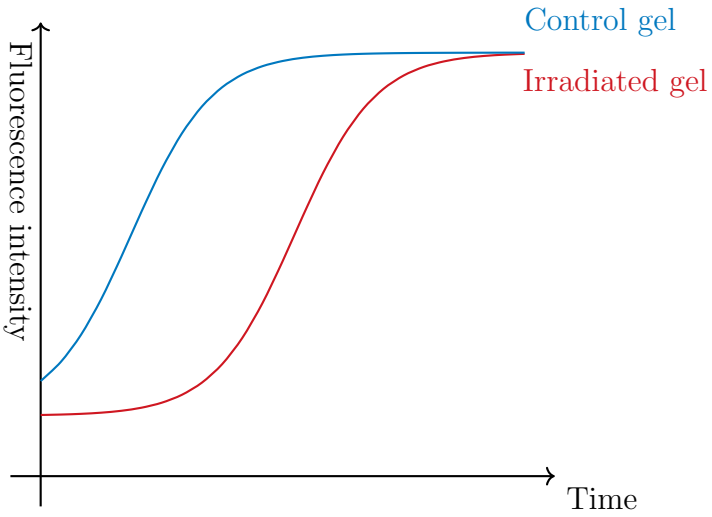

Figure 1.13: *Illustration of the expected result after an irradiation experiment. The time $t = 0$ corresponds to the day the irradiation experiment was performed.*

HeLa cells typically divide every 22 hours, meaning every 22 hours the amount of HeLa cells in each sample doubles [44]. The cell growth over time can thus mathematically be described with exponential growth. However, the amount of cells cannot increase

indefinitely due to the limited nutrient medium and space available. Consequently, after a finite amount of time the total number of cells in each sample will start to saturate [45]. At $t = 0$, a difference in fluorescence intensity is expected due to the direct damage caused by the alpha particles. The cells inside the gel of the control sample were not damaged and thus will keep dividing in the days following the irradiation experiment until saturation is reached. As a result, the measured fluorescence intensity is expected to keep increasing as well until saturation is reached. The fluorescence intensity measured from the irradiated gel, on the other hand, will not immediately increase as a consequence of the cells attempting to repair non-lethal damage caused by the alpha particles. It is even possible for the fluorescence intensity to slightly drop after the first day due to irreparable damage. However, afterwards, once the non-lethal damage is repaired or the cells died, the remaining cells in the irradiated sample will start dividing as well resulting in an increase in fluorescence intensity until the same saturation level is reached. The same saturation level is expected for both the control and irradiated gel because the same amount of nutrient medium is added to both each time a Resazurin assay is performed (see Figure 1.11) and the cells also have the same amount of space available in both gels.

1.9 Fluorescence Intensity Calibration

Once multiple Resazurin assays are performed, and a graph similar to the one in Figure 1.13 is obtained, a fluorescence calibration will be required. That way, the fluorescence intensities as function of time obtained from the Resazurin assays can be converted to the amount of cells that are alive after irradiation as a function of time. The required fluorescence calibration will be discussed in more detail in the subsequent subsections.

1.9.1 Preparation of the Initial Cell Solution

The calibration is obtained by making use of a serial dilution of which the fluorescence intensity is measured after three hours incubation with Resazurin. The first step in the preparation of the serial dilution is an initial cell solution obtained by following the steps given in section 1.2. However, there was one slight change near the end of the procedure described in this section: Instead of removing 4 mL of the cell solution from the flask, 5 mL of the solution was removed and added to a new and empty plastic test tube. Subsequently, the concentration was determined by making use of the procedure described in section 1.3 such that a value equal to $2.52(26) \times 10^6$ cells/mL was obtained. In order to increase the concentration even more, the cell solution was centrifuged for five minutes at 1500 rounds per minute. Afterwards, 3 mL of the solution was removed from the top, meaning the cell concentration of the remaining 2 mL solution in the test tube was equal to

$$\frac{5 \text{ mL}}{2 \text{ mL}} \cdot 2.52(26) \times 10^6 \text{ cells/mL} = 6.31(70) \times 10^6 \text{ cells/mL}. \tag{1.3}$$

The remaining 2 mL solution having a cell concentration equal to $6.31(70) \times 10^6$ cells/mL served as the initial cell solution from which the dilution series was prepared.

1.9.2 Preparation of the Serial Dilution

To obtain the dilution series required for the fluorescence calibration, a 8×12 microplate, as illustrated in Figure 1.14, was used. The microplate was a Greiner 96 microplate, made from transparent polystyrol.

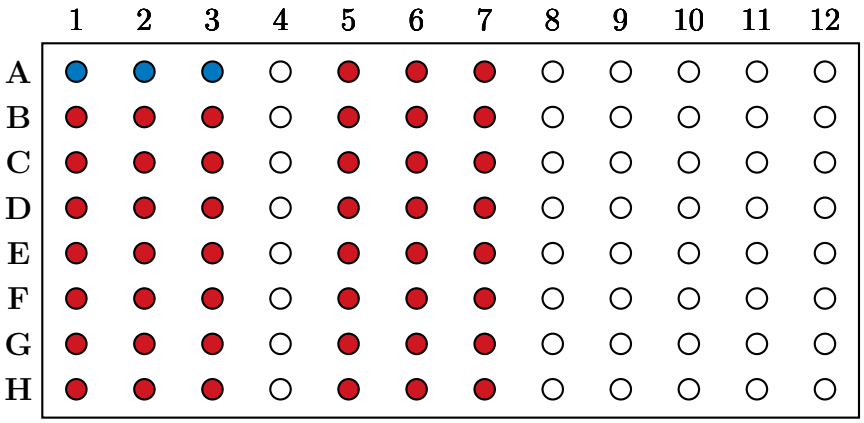

Figure 1.14: *Top view illustration of the* 8×12 *microplate that was used for the serial dilution. The wells indicated in red are part of the serial dilution and thus contain cells, while the wells indicated in blue only contain FluoroBrite™ and serve as a reference.*

First, each well indicated in either red or blue in Figure 1.14 was filled with 100 μL of FluoroBrite™. The nutrient medium discussed in Appendix A and the FluoroBrite™ solution are almost identical to each other except for one key difference: The FluoroBrite™ does not contain any phenol red, while the nutrient medium does. Consequently, using FluoroBrite™ for determining the calibration curve results in less fluorescence background noise compared to the nutrient medium discussed in Appendix A. Next, 100 μL of the $6.31(70) \times 10^6$ cells/mL solution was pipetted into well B1. Both the FluoroBrite™ present in the well and the cell solution were then thoroughly mixed by pipetting the solution fifteen times in and out the pipette. Subsequently, 100 μL of the solution in well B1 was pipetted in well C1. The solution was again pipetted fifteen times in and out the pipette in order to thoroughly mix the solution. Next, 100 μL of the solution in well C1 was pipetted in well D1, etc. This process was repeated each time starting from well B1 up until well H1. From well H1, 100 μL was pipetted into well A5 and the same procedure was repeated up until well H5. In total, three identical serial dilutions were prepared using the procedure explained above:

1. Starting in well B1 up until well H1, continuing in well A5 up until well H5,
2. Starting in well B2 up until well H2, continuing in well A6 up until well H6,
3. Starting in well B3 up until well H3, continuing in well A7 up until well H7.

The main advantage of this technique is that by pipetting 100 μL of the previous well in the subsequent well, the concentration of the cells is each time reduced by a factor two. This was done several times to allow the fluorescence of a range of cell concentrations to be measured. The three wells indicated in blue (A1, A2 and A3) only contain FluoroBrite™, no cells, and served as a reference. A summary of the cell concentration in each well indicated in either red or blue in Figure 1.14 is given in Table 1.1.

Table 1.1: *Summary of the cell concentration in each well indicated in either red or blue in Figure 1.14.*

Wells	Cell concentration [cells/mL]	Wells	Cell concentration [cells/mL]
A1, A2, A3	0	A5, A6, A7	$2.47(26) \times 10^4$
B1, B2, B3	$3.16(33) \times 10^6$	B5, B6, B7	$1.233(130) \times 10^4$
C1, C2, C3	$1.578(160) \times 10^6$	C5, C6, C7	$6.16(60) \times 10^3$
D1, D2, D3	$7.89(80) \times 10^5$	D5, D6, D7	$3.08(32) \times 10^3$
E1, E2, E3	$3.95(40) \times 10^5$	E5, E6, E7	$1.541(160) \times 10^3$
F1, F2, F3	$1.97(21) \times 10^5$	F5, F6, F7	$7.70(80) \times 10^2$
G1, G2, G3	$986(100) \times 10^2$	G5, G6, G7	$3.90(40) \times 10^2$
H1, H2, H3	$4.93(50) \times 10^4$	H5, H6, H7	$1.93(20) \times 10^2$

The well plate was then placed for two hours in the incubator at 37 °C to make sure all cells inside the solution are able to sediment towards the bottom of the plate. Subsequently, after removing 100 μL from each well, 100 μL of a ten-times diluted Resazurin solution with FluoroBrite™ was added to each well using a pipette. The amount of cells is proportional to the cell concentration. Hence, a linear relation between the cell concentration and the fluorescence intensity is expected as well (see Equation 1.2).

1.9.3 Results: The Calibration Curve

Once the well plate incubated for three hours at 37 °C, the fluorescence intensity of each well was determined using a fluorometer in a similar way as explained in section 1.6. The measured fluorescence intensity of each well is summarized in Table 1.2 and is given in arbitrary units (a.u.). The higher the number, the more fluorescence photons emitted by the cell solution in the wells were detected.

Table 1.2: *Summary of the measured fluorescence intensity of each well that was indicated in either red or blue in Figure 1.14. The intensities for each well are given in arbitrary units.*

	1	2	3	5	6	7
A	278	269	284	928	1194	1392
B	7723	7923	8518	612	468	342
C	7993	8021	7715	470	413	347
D	7312	7451	7038	371	279	328
E	6118	6369	5865	345	316	278
F	3704	3284	3373	305	305	303
G	2499	2322	2102	310	302	279
H	1424	1304	1364	302	289	295

The fluorescence signal of each dilution series was normalised to each of the control samples in wells A1, A2 and A3 respectively to correct for background noise, such as for example fluorescence photons emitted by the FluoroBrite™.

As discussed in subsection 1.9.2, three identical serial dilutions were prepared. Hence, as is also shown in Table 1.1, the cell concentration in wells B1, B2, B3 are all equal, the cell concentration in wells C1, C2, C3 are all equal, etc. In order to associate a fluorescence intensity to these cell concentrations, the average measured fluorescence intensity was calculated for each well with equal cell concentration. The results are summarized in Table 1.3.

Table 1.3: *Summary of the average fluorescence intensity of each well that was indicated in either red or blue in Figure 1.14. The given intensities are normalized and thus dimensionless quantities.*

Wells	Average fluorescence intensity	Wells	Average fluorescence intensity
A1, A2, A3	1	A5, A6, A7	4.23(40)
B1, B2, B3	29.08(50)	B5, B6, B7	1.72(24)
C1, C2, C3	28.58(60)	C5, C6, C7	1.483(110)
D1, D2, D3	26.26(70)	D5, D6, D7	1.176(70)
E1, E2, E3	22.11(70)	E5, E6, E7	1.132(60)
F1, F2, F3	12.47(40)	F5, F6, F7	1.0993(160)
G1, G2, G3	8.34(40)	G5, G6, G7	1.073(40)
H1, H2, H3	4.924(80)	H5, H6, H7	1.0665(120)

The uncertainties associated to the values in Table 1.3 are statistical uncertainties which were determined by calculating the standard deviation divided by the square root of number of repeated measurements, which is equal to three in this case.

Finally, when combining the results in Table 1.1 and Table 1.3, the fluorescence calibration curve shown in Figure 1.15 is obtained.

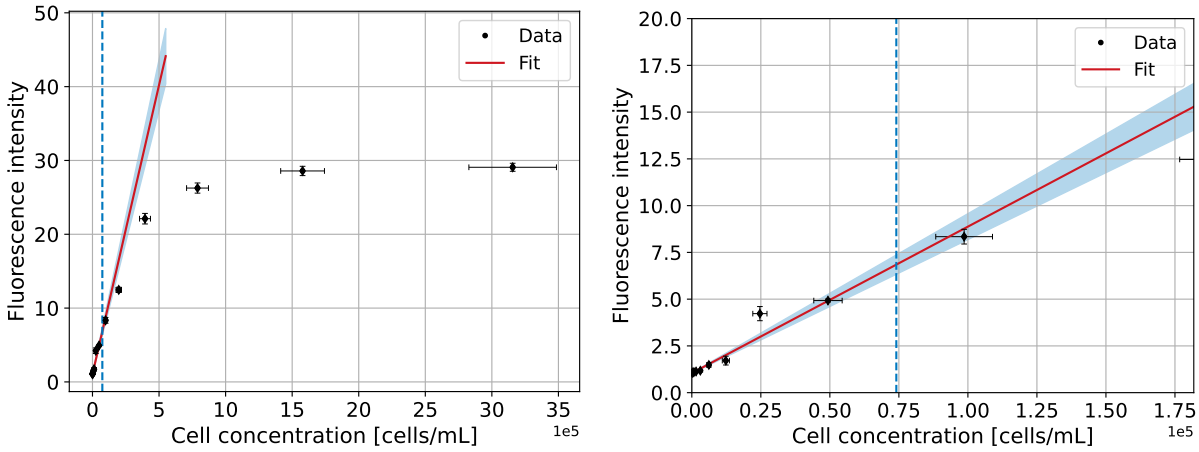

(a) **(b)**

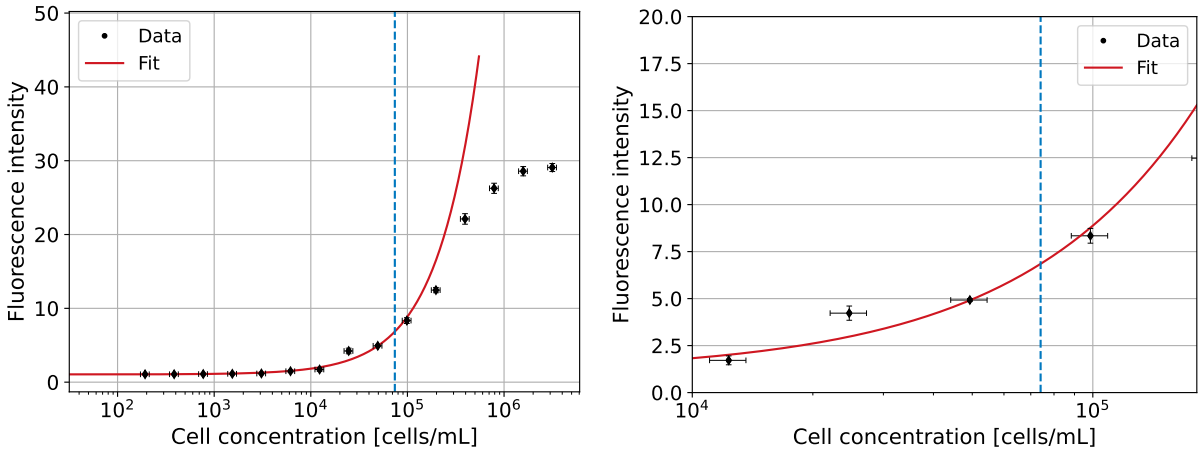

(c) **(d)**

Figure 1.15: *The fluorescence calibration curve. The fluorescence intensity expressed on the vertical axis in each graph is the average fluorescence intensity shown in Table 1.3. The cell concentration (in cells/mL) expressed on the horizontal axis is shown in Table 1.1. The region in blue indicates the uncertainty on the fit due to the fitparameters. The vertical dashed blue line indicates the expected cell concentration when performing the Resazurin assays during the cell-irradiation experiments. Both graphs in (a) and (c) show each data point, while the graphs in (b) and (d) show a close-up of the region of interest. The horizontal axis in (c) and (d) is a logarithmic scale.*

As a result of the steps taken in the preparation of the serial dilution, the cell concentration on the horizontal axis is thus defined as the number of cells per mL of the total volume. That way, by utilizing the cell concentration instead of the amount of cells in the fluorescence calibration, the impact of the available Resazurin on the measured fluorescence intensity is taken into account as well. Consequently, when utilizing the fluorescence calibration for the cell-irradiation experiments, the cell concentration is expected to be near

$$\frac{0.08 \cdot 10^6 \text{ cells}}{80\ \mu\text{L} + 1\ \text{mL}} \approx 74074\ \text{cells/mL} \tag{1.4}$$

as a result of adding approximately a 80 μL gel with a cell concentration equal to 10^6 cells/mL into a well containing 1 mL of Resazurin. This value is indicated with the dashed blue line in Figure 1.15 and is within the linear region.

Due to the proportionality relation between the cell concentration and the measured fluorescence intensity, a linear function of the form

$$y = ax + b \tag{1.5}$$

was proposed to fit the data. However, this linear relation is only valid if no saturation occurs. An equal amount of Resazurin was added in each well, but whenever the cell concentration in a well is too high, only a limited number of cells have access to the available Resazurin whereby only a limited number of cells can reduce the Resazurin to Resorufin. Hence, the number of cells will not be proportional anymore to the amount of Resorufin if the cell concentration is too high. Consequently, the five data points in Figure 1.15a (and Figure 1.15c) where the concentration is the highest were not taken

into consideration for the linear fit due to the fact that for these concentrations saturation can be observed. At the end of this section, more details are provided to argue why it was justified to remove these five data points to obtain the fit.

The data in Figure 1.15 was fit using the Python package *Orthogonal Distance Regression* (`scipy.odr`) [46] in order to take both the uncertainties on the cell concentration and the average fluorescence intensity into account. The values of a and b in the linear model in Equation 1.5 were respectively found to be equal to $7.83(68) \times 10^{-5}$ mL/cells and 1.0446(123). The associated reduced χ^2-value is equal to 2.13, indicating the fit and the data are almost in agreement with each other [47]. The relative residuals, (i.e., the residuals expressed in units of standard deviations) corresponding to the fit in Figure 1.15 are shown in Figure 1.16.

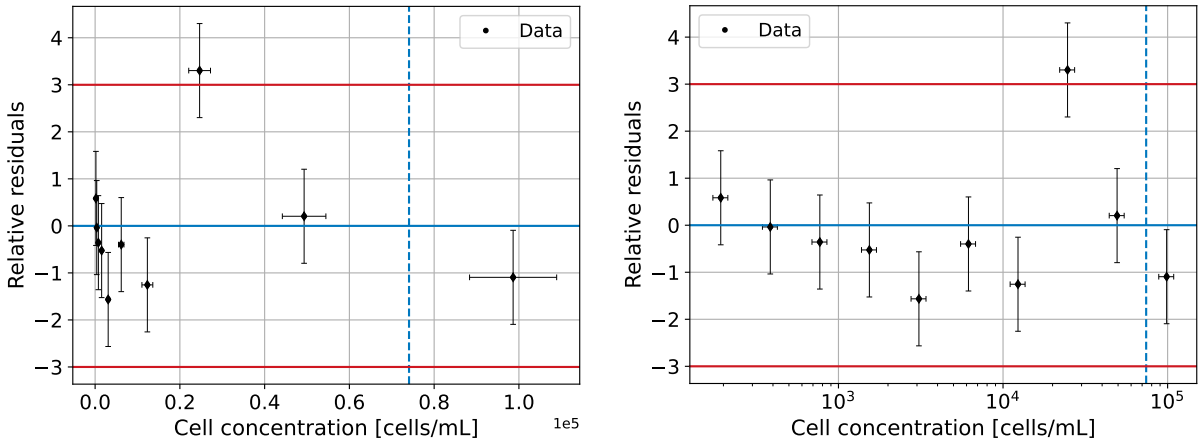

(a) **(b)**

Figure 1.16: *Plot of the relative residuals as function of the cell concentration (in cells/mL). The horizontal blue line indicates when the residuals are equal to zero. Both horizontal red lines indicate when the residuals are equal to three or minus three standard deviations. Only the residuals corresponding to data points used for the fit in Figure 1.15 are shown here. The vertical dashed blue line indicates the expected cell concentration when performing the Resazurin assays in the cell-irradiation experiments. Both graphs in (a) and (b) show the same residuals, but the horizontal axis in (b) is a logarithmic scale.*

Except for one residual, at a cell concentration near 0.25×10^5 cells/mL, all residuals are smaller than three standard deviations and larger than minus three standard deviations. Hence, the residual near 0.25×10^5 cells/mL in Figure 1.16 could explain the slightly high reduced χ^2-squared value. With the residuals shown in Figure 1.16, a more rigorous justification can be provided for not taking the five data points with highest concentration into consideration for the fit. More specific, in Figure 1.17, the same residuals from Figure 1.16 are shown. However, one additional residual was added as well: The residual corresponding to the data point with the smallest concentration out of the five data points with highest concentration that were left out to obtain the fit (i.e., the data point with a concentration near 2×10^5 cells/mL in Figure 1.15). The residual corresponding to this data point indicates a value near minus eleven standard deviations. This clearly indicates a deviation from the linear fit due to saturation which justifies not considering this data point for the fit. Moreover, due to the fact that the remaining four data points are even

further away from the linear fit, as can be observed in Figure 1.15, it was justified to not take these four data points into consideration either.

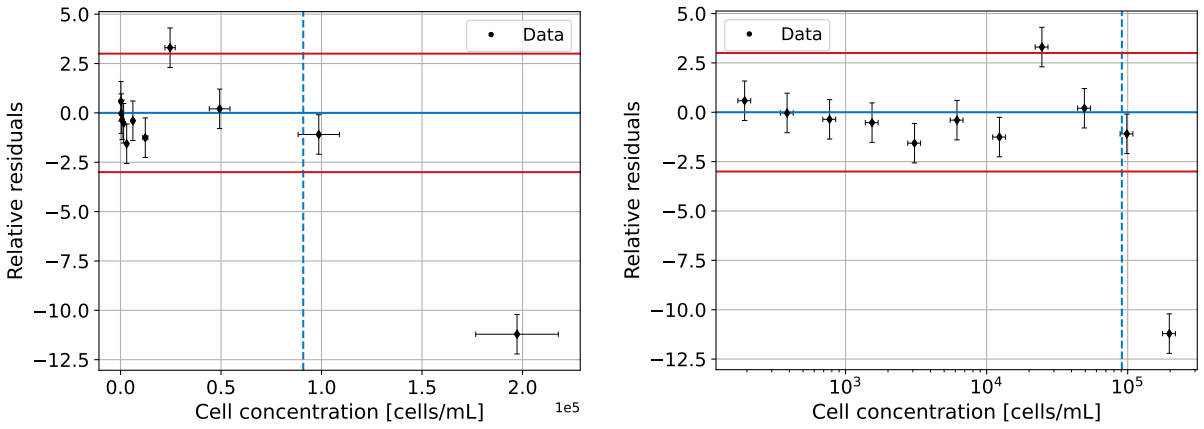

(a) (b)

Figure 1.17: *Plot of the relative residuals as function of the cell concentration (in cells/mL) from Figure 1.16 with the addition of the residual corresponding to the data point near* 2×10^5 *cells/mL in Figure 1.15. The horizontal blue line indicates when the residuals are equal to zero. Both horizontal red lines indicate when the residuals are equal to three or minus three standard deviations. The vertical dashed blue line indicates the expected cell concentration when performing the Resazurin assays in the cell-irradiation experiments. Both graphs in (a) and (b) show the same residuals, but the horizontal axis in (b) is a logarithmic scale.*

1.10 Shortcomings of the Cell-Irradiation Protocol

Once multiple irradiation experiments are performed by utilizing the cell-irradiation protocol discussed in this chapter, and thus multiple graphs similar to the one in Figure 1.13 are obtained, the time can be determined at which the difference in number of cells alive in the control sample compared to the number of cells alive in the irradiated sample is the largest. It will be at this time that in a later stage of the experimental endeavor the cell viability will be determined. However, the existing cell-irradiation protocol described in this chapter has some shortcomings that will be addressed in the remainder of this section.

1.10.1 2.0 mg/mL Collagen Gel Preparation

By following the steps of the cell-irradiation protocol described in section 1.2 up to section 1.7, a first irradiation experiment was performed. The hydrogels that were used for this irradiation experiment were collagen gels, which were prepared in a similar way compared to the gels that Lens Dedroog and Olivier Deschaume prepared in Viktor Van den Bergh's master's thesis [2]. However, one change was made: In Viktor's thesis the collagen hydrogels were prepared using a 1.5 mg/mL collagen solution. The gels turned out to be very fragile and easily damaged resulting in unwanted cell death. Hence, in order to create a stronger and stiffer hydrogel, a 2.0 mg/mL collagen solution was used

instead in this project [2].[4]

In order to prepare the collagen solution, four ingredients were utilized:

- A 6 mg/mL collagen type I stock solution of bovine origin,
- A 0.1 M NaOH solution,
- The nutrient medium discussed in Appendix A,
- The cell solution that was obtained by following the protocol discussed in section 1.2 of which the cell concentration is known.

First, the collagen stock solution needs to be diluted three times. Moreover, the stock solution is typically acidified with acetic acid and thus needs to be neutralized as well using the 0.1 M NaOH solution to obtain a neutral pH equal to 7.4(1) [48]. If the pH of the gel is too low, the cells will not be able to survive in it. As a rule of thumb to neutralize the collagen stock solution, 10 μL of a 0.1 M NaOH solution was added for each 66.66 μL collagen stock solution.

When preparing the samples for the irradiation experiments, typically 600 μL of the collagen-gel solution is required in order to prepare two samples. As a result, 200 μL of the collagen stock solution and 30 μL of the 0.1 M NaOH solution is required. The remainder of the 600 μL solution, i.e. 370 μL, consists of the nutrient medium discussed in Appendix A mixed with the cell solution that was obtained following the steps given in section 1.2. As was stated in the end of section 1.2, the choice was made to prepare the gels with a concentration equal to 10^6 cells/mL such that the results of different irradiation experiments can be compared to each other. Hence, if the concentration of the initial cell solution is equal to $a \times 10^6$ cells/mL, $\frac{600}{a}$ μL of the cell solution will be required. As a consequence, 370 μL $-$ $\frac{600}{a}$ μL of the nutrient medium discussed in Appendix A will be needed. However, if the cell concentration of the solution is too low, meaning that the required volume equal to $\frac{600}{a}$ μL would exceed the available 370 μL, the cell solution needs to be centrifuged first for five minutes at 1500 rounds per minute. Once the solution is centrifuged, part of the cell solution volume needs to be removed from the top in order to increase the concentration. More specifically, the initial volume of the cell solution is equal to 4 mL (see section 1.2). If the final volume of the cell solution is equal to V (in units of mL) when part of the initial 4 mL is removed from the top after centrifugation, the new concentration of the cell solution is equal to $\left(\frac{4\text{ mL}}{V} \cdot a\right) \times 10^6$ cells/mL.

In conclusion, in order to prepare 600 μL of the collagen-gel solution,

- 200 μL of the collagen stock solution,
- 30 μL of a 0.1 M NaOH solution,
- $\frac{600}{a}$ μL of the cell solution (or $\frac{600}{\frac{4\text{ mL}}{V} \cdot a}$ μL after centrifugation),
- 370 μL $-$ $\frac{600}{a}$ μL of the nutrient medium discussed in Appendix A (or 370 μL $-$ $\frac{600}{\frac{4\text{ mL}}{V} \cdot a}$ μL after centrifugation)

[4] The higher the collagen concentration in the gel, the more fibrils present and thus the more crosslinks formed which results in a stronger and stiffer gel.

is required where $a \times 10^6$ cells/mL is the concentration of the initial cell solution before centrifugation and V (in units of mL) the volume of the cell solution when part of the initial 4 mL is removed from the top after centrifugation.

1.10.2 Results

The results of the irradiation experiment, after having applied the fluorescence calibration obtained in section 1.9, are shown in Figure 1.18.

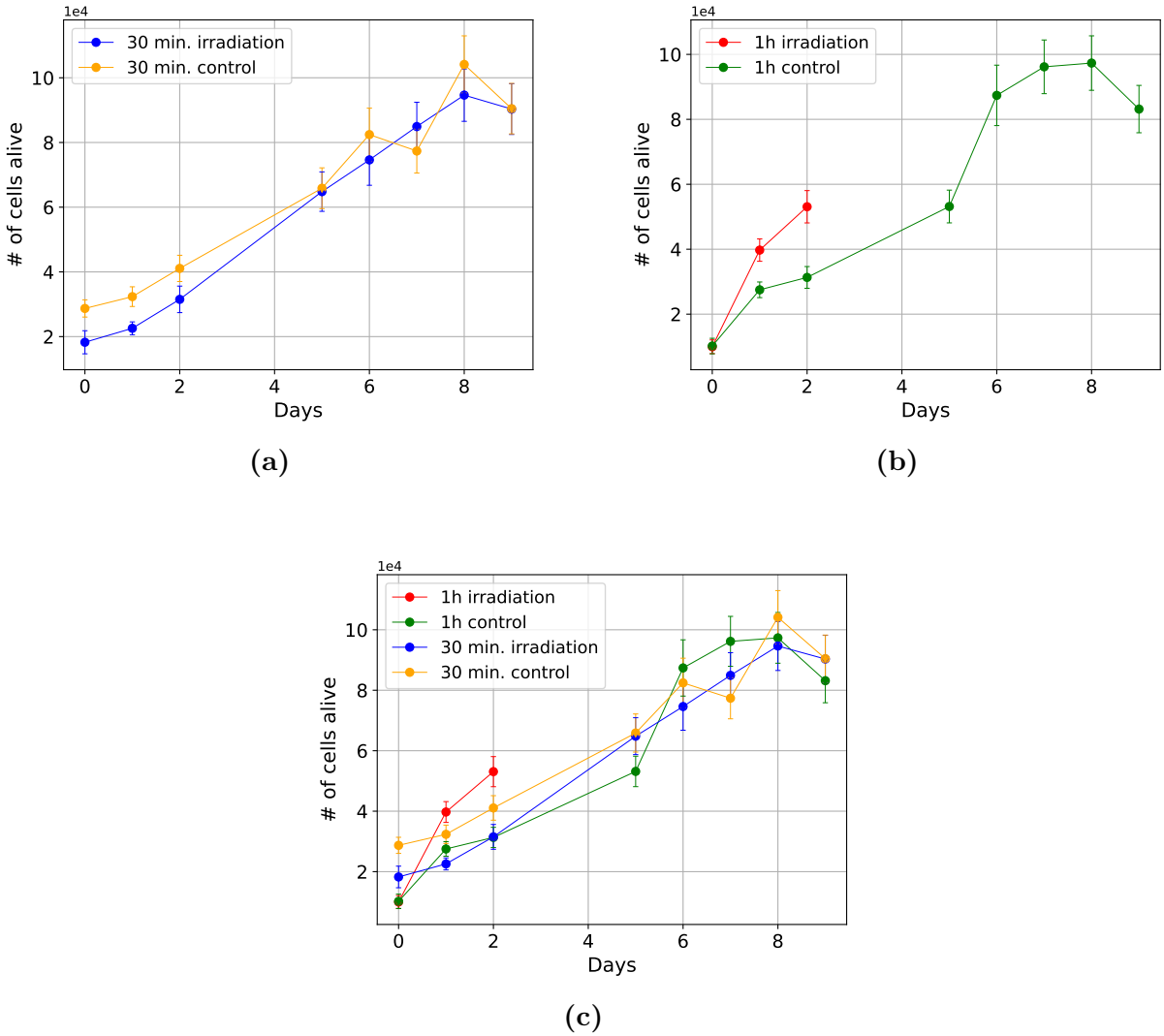

Figure 1.18: *Results of the irradiation experiment using 2.0 mg/mL collagen hydrogels. The graph in (a) shows the results of the sample that was irradiated for thirty minutes (in blue) together with the corresponding control sample (in yellow). The graph in (b) shows the results of the sample that was irradiated for one hour (in red) together with the corresponding control sample (in green). Finally, in (c), the results show in (a) and (b) are combined in a single graph.*

Due to a handling issue with the gel that was irradiated for one hour, the fluorescence intensity of the gel in this sample could only be measured up to two days after irradiation. Nonetheless, the graph in Figure 1.18b indicates results that are not in accordance with

what is expected: The data points corresponding to the sample that was irradiated for one hour indicate a higher number of cells that are alive compared to the corresponding control sample. Moreover, the data points on day 0, the day of the irradiation experiment, seems to suggest the alpha particles had no significant impact on the cells at all.

On the other hand, upon comparing the blue and yellow data points in the graph in Figure 1.18a, it can be observed that the data points corresponding to the sample that was irradiated for thirty minutes indicate a higher number of cells that are alive compared to the data points of the control sample which is in accordance with what is expected. Nonetheless, the difference between both samples is rather limited due to only a difference of 24(7)% in number of alive cells on day 0 which indicates a rather limited impact of the alpha particles. Upon comparing both measurements in the graph in Figure 1.18c on day 0, the highest number of cells alive is in the thirty-minute control sample while the lowest number of cells alive is in both the one-hour control and one-hour irradiated sample. However, both control samples should, in principle, have more or less the same amount of cells alive. This is clearly not what is observed and could be a result of additional damage caused to the cells.

To investigate why the results shown in Figure 1.18 are not in accordance with what is expected, three hypotheses were proposed:

1. The increase of the collagen concentration from 1.5 mg/mL to 2.0 mg/mL heavily impacted the cell sedimentation inside the hydrogel. Hence, due to the poor cell sedimentation, the emitted alpha particles are not able to reach the cells deeper inside the gel.

2. After irradiation, both the gel inside the control sample and the gel inside the sample that was irradiated need to be taken out of the Teflon holders to perform the Resazurin assay (see section 1.6). The gels are taken out of the holders using a pair of tweezers which probably causes more damage to the cells compared to the irradiation.

3. Often adhesion of gel fragments to the glass slide could be observed upon removing it from the gel. However, if the cells sedimented well and are positioned in the top layer of the gel, the cells will be torn off from the gel upon removing the glass slide. Consequently, the cells will adhere to the glass slide as well and thus will not be irradiated.

All three hypotheses were investigated in this project and it turned out that all three of these aspects required adjustments. More details will be given in the subsequent two chapters: First, in chapter 2, the issues regarding the cell sedimentation will be addressed. Secondly, in chapter 3, the modifications made to the glass slides and the Teflon holders will be discussed in detail to avoid respectively gel adhesion to the glass and the gel manipulation after irradiation.

"Think inside the box. That's right, I said inside. You know why? Because while everyone is chasing each other around outside the box, you know what the box is? Empty."

Phil Dunphy – Modern Family

2

Investigating the Cell Sedimentation

In this chapter the cell sedimentation in three different hydrogels will be discussed: In 2.0 mg/mL collagen gels, 5 weight percentage (wt%) polyethylene glycol (PEG) hydrogels and hydrogels containing 50% Matrigel.

As the results in section 2.5 will show, a poor cell sedimentation was observed in the 2.0 mg/mL collagen gels. Hence, this seems to confirm the first hypothesis stated near the end of subsection 1.10.2 that the cells are not within reach of the alpha particles due to the poor sedimentation in the gel. Consequently, two potential alternatives were proposed for the cell-irradiation experiments, i.e. 5 wt% PEG hydrogels and hydrogels containing 50% Matrigel, and the cell sedimentation in these hydrogels was investigated as well. The PEG hydrogels promise to be much stiffer (and thus stronger) compared to the 2.0 mg/mL collagen gels thus making them in the cell-irradiation protocol much easier to manipulate and more resistant to damage caused by gel manipulations. However, the higher density of these gels might result in a poorer cell sedimentation as well. A hydrogel containing 50% Matrigel, on the other hand, promises to be equally stiff compared to the 2.0 mg/mL collagen gels, but an excellent cell sedimentation is expected due to the unique properties of this material which will be discussed in more detail later in this chapter.

First, in section 2.1 and section 2.2, more details will be provided on PEG and Matrigel. Moreover, in both these sections, the claims made in this introduction regarding the characteristics of these materials will be motivated in a more exact way. Subsequently, in section 2.3, further reference on confocal microscopy will be provided as this technique was utilized to probe the cell sedimentation in each material. Lastly, after having discussed the gel and sample preparations of the 5 wt% PEG hydrogels and hydrogels containing 50% Matrigel in section 2.4, the results of the confocal microscopy measurements will be shown and discussed in the remainder of this chapter.

2.1 Polyethylene Glycol

Polyethylene glycol (PEG) is a linear polymer that can be expressed with the chemical formula $H(OCH_2CH_2)_nOH$, where $n \geq 4$ [49]. In this project, 5 wt% PEG hydrogels were prepared using 8-arm PEG, which is a multi-arm polyethylene glycol consisting of a hexaglycerol core on which eight arms are connected with a vinylsulfone group at the end of each arm [50]. The PEG polymers are crosslinked by adding dithiothreitol (DTT) that binds to the vinylsulfone groups at the end of each arm which allows the PEG molecules to be attached to each other such that a gel can be formed.

The main advantage of using PEG hydrogels is that the produced gels will be much stiffer, and thus stronger, compared to both the 1.5 mg/mL collagen gels Viktor used in his master's thesis and the 2.0 mg/mL collagen gels discussed in subsection 1.10.1. This can clearly be seen upon comparing the linear elastic (or storage) modulus[1] of both materials: For a 2.0 mg/mL collagen gel, a value equal to 20.4 Pa is obtained while for a 5 wt% PEG hydrogel a value equal to 3788.3 Pa is found. Hence, utilizing PEG gels would thus result in more robust hydrogels such that less additional damage is caused to the cells inside due to the gel manipulations during the cell-irradiation protocol. However, due to the fact that the PEG gels also have a much higher density compared to both the 1.5 mg/mL and 2.0 mg/mL collagen gels, the cell sedimentation might be much poorer as well which was investigated in this project.

2.2 Matrigel

The cell sedimentation was also investigated in hydrogels containing 50% Matrigel. Matrigel is a cell- and tissue-derived substance extracted from an Engelbreth-Holm-Swarm (EHS) mouse tumor that is rich in extracellular matrix proteins [52, 53]. In this project, Corning® Matrigel was used which contains

- 60% of laminin, which are complex adhesion proteins that are most typically found in the basement membrane [52, 54],
- 30% of collagen type IV, which is the major component of the basement membrane and is essential for structural maintenance [52, 55, 56],
- 8% of entactin, which is a molecule that interacts with laminin and collagen type IV and is important for structural organization [52],
- 2% of growth factors, which are signaling proteins stimulating, among other things, cell growth and tissue repair, and heparan sulfate proteoglycans which are receptors that are, among other things, important for growth factor action [52, 57].

The above-mentioned percentages are only approximately true. Hence, when comparing different Matrigel batches, the composition can slightly differ. Moreover, the composition

[1] The linear elastic (or storage) modulus is a measure for the amount of energy stored in a material and thus provides insight in the structure present inside the material. The higher this value, the stiffer the material. The linear elastic storage modulus is typically expressed in Pascal (Pa) [51]. Each storage modulus that will be given in this thesis, unless mentioned otherwise, was measured by Lens Dedroog by applying an oscillating strain (i.e., a torque) at an angular frequency of 1 rad/s using a stress controlled rheometer (MCR501 Anton Paar).

of the final 2% consisting of growth factors and heparan sulfate proteoglycans is not exactly known, only approximate values are given (see for example [52]).

Nonetheless, Matrigel promises from a theoretical point of view to be an excellent material for the cell-irradiation experiments due to its unique temperature range for gel formation. More specifically, when the proteins in Matrigel have enough energy, at temperatures between 22 °C and 35 °C, the functional domains of these proteins can interact with each other which eventually will result in a gel. At low temperatures, near 4 °C, the functional domains of the proteins do not have enough energy to interact with each other and, as a consequence, the Matrigel remains liquid at these low temperatures. When comparing the cell sedimentation in gels containing Matrigel to the collagen or PEG gels, an improved cell sedimentation is thus expected from a theoretical point of view due to the fact that Matrigel remains liquid while in the fridge. More specifically, even at a decreased rate, bonds are still formed in the collagen and PEG solutions at 4 °C - 5 °C which impacts the cell sedimentation to some extent [58]. Matrigel, on the other hand, remains liquid at these temperatures due to the fact the functional domains of the proteins simply do not have enough energy to interact with each other. Consequently, because the fridge is at a temperature of 4 °C - 5 °C, no bonds will be formed while in the fridge that will disturb the cell sedimentation.

However, the downside of working with Matrigel is that during the measurements, the Matrigel has to be held on ice at all times. The reason for this is that once the functional domains of the proteins have enough energy, which is typically near 10 °C, the Matrigel will start to solidify quicker than the collagen gels [52]. Once the gel formation is completed, the result will be a gel that is approximately equally stiff as the 2.0 mg/mL collagen gels, but less stiff compared to the PEG hydrogels. This can be seen upon comparing the linear storage moduli of both materials: For a 2.0 mg/mL collagen gel, a value equal to 20.4 Pa is obtained while for gels containing 50% Matrigel a value equal to 21.6 Pa can be found. Thus using hydrogels containing Matrigel as material for the irradiation experiments would, in theory, result in a stronger gel compared to the 1.5 mg/mL collagen gels that solves the cell-sedimentation problem as well. Hence, this hypothesis was tested by experimentally investigating the cell sedimentation using confocal microscopy.

2.3 Confocal Microscopy

A brief overview regarding the fundamentals of confocal microscopy will be given in this section based on the schematic illustration shown in Figure 2.1.

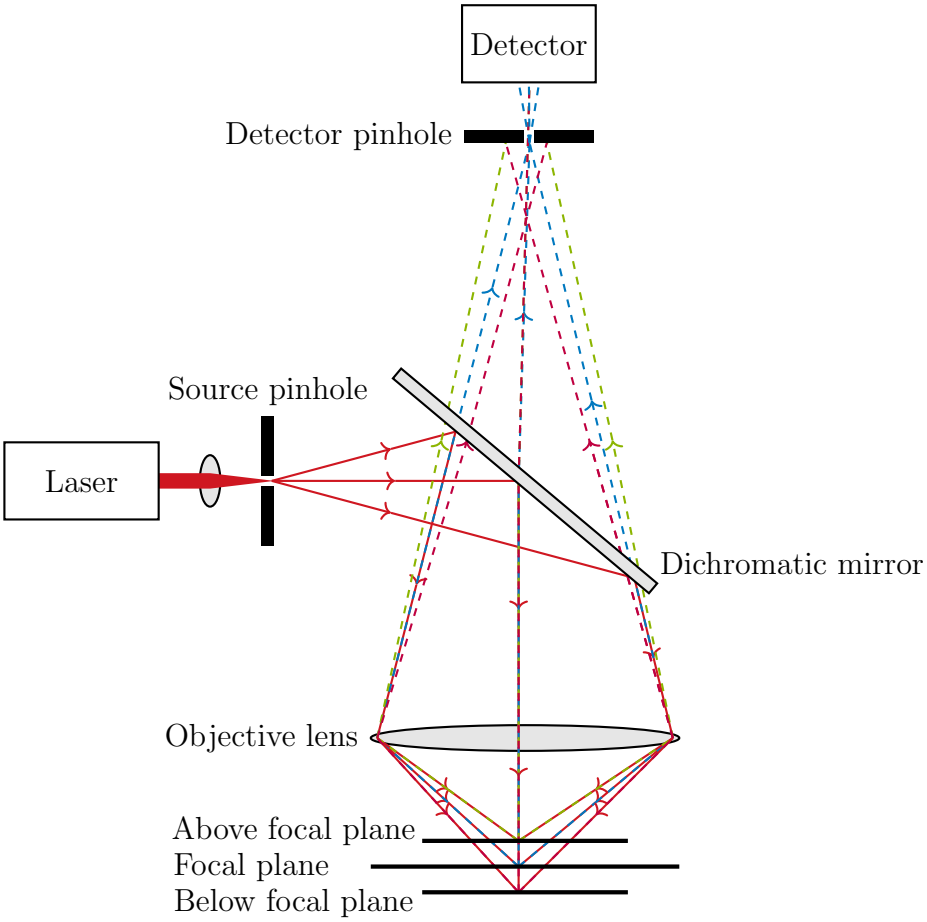

Figure 2.1: *Illustration indicating the fundamentals of confocal microscopy. The fluorescence photons emitted by the dyes in the sample are indicated by the dashed lines. Figure adapted from [59].*

In confocal microscopy, a laser emits light towards a beam splitter (i.e., the dichromatic mirror) which reflects the emitted photons towards an objective lens. Due to the presence of the source pinhole in front of the laser, in combination with the objective lens, the emitted photons are focused on a specific spot in the sample, as illustrated by the red lines in Figure 2.1. The wavelength of the photons emitted by the laser is chosen in such a way that the photons are absorbed by the fluorescent dye in the sample and fluorescence photons with a longer wavelength will be emitted from the dye as a consequence. The fluorescence photons are indicated in dashed lines in Figure 2.1. A dichromatic (or dichroic) mirror reflects light with a wavelength shorter than a certain wavelength and light with a larger wavelength will be able to pass. Hence, a suitable dichromatic mirror can be chosen which reflects the light emitted by the laser towards the sample and lets the emitted fluorescence photons pass due to their difference in wavelength [59, 60, 61].

Even though the light emitted by the laser is focused on a certain spot in the sample, some of the photons will still be absorbed by the dye slightly above or below the focal plane due to, for example, scattering in the sample. Consequently, fluorescence photons are emitted slightly above or below the focal plane which will result in a blurry image. Hence, in order to maintain a high-resolution image, the detector is provided with a detector pinhole which prevents most of the photons emitted slightly above or below

the focal plane from reaching the detector. However, the photons emitted in an almost vertical direction towards the detector, are still detected. This is indicated in Figure 2.1 by the green and purple vertical dashed lines reaching the detector. Consequently, the imaged cells will appear more elongated in the direction towards the detector than they in reality are (i.e., instead of spherical shapes, the cells in the gel will appear to have a more ellipsoid shape).

In this project, the cells embedded in the hydrogel were stained using two different dyes: Calcein AM and Ethidium homodimer in order to respectively image living cells and dead (or dying) cells. Calcein AM itself is not fluorescent. However, it can be transported through the cell membrane where it can be converted by metabolic active cells to the green-fluorescent dye Calcein [62]. Calcein is able to absorb photons with a wavelength near 494 nm and will emit fluorescence photons with a wavelength near 517 nm [63]. Ethidium homodimer, on the other hand, is a membrane-impermeable and high-affinity nucleic acid stain. When cells are dead or dying, their plasma membrane becomes disrupted and, as a consequence, the Ethidium homodimer is able to enter the dead or dying cells and bind to their DNA. When bound to the DNA, the Ethidium homodimer is able to absorb photons with a wavelength near 528 nm and will emit fluorescence photons with a wavelength near 617 nm which results in a red color [64]. The values for the wavelengths given in this paragraph correspond to the maxima of both the emission and absorption spectrum of the dyes.

Due to the difference in excitation wavelength between both dyes, it was not possible to image both living and dead cells at the same time. Hence, each sample was imaged three times and the obtained results were afterwards combined in a single image. Each time a different filter was used for imaging, resulting in the emission of photons with different wavelengths:

- First, photons with a wavelength equal to 488 nm were emitted in order to image all the living cells.
- Secondly, photons with a wavelength equal to 514 nm were emitted in order to image all the dead or dying cells.
- Thirdly, photons with a wavelength equal to 488 nm were emitted in order to image the bottom of the well containing the gel (see Figure 2.2 in the next section).

The same wavelength was used to image the living cells and the bottom of the well plate. However, when imaging the bottom of the well plate, no fluorescence photons were emitted meaning that the wavelength of the measured photons was also equal to 488 nm, resulting in a blue color. Hence, in the results shown in section 2.5, the living cells will appear in green, the dead or dying cells in red and the bottom of the well plate in blue.

2.4 Gel and Sample Preparation

The gel and sample preparation required for the confocal microscopy measurements are discussed in this section.

2.4.1 Gel Preparation

The first step in each gel preparation, is to obtain an initial cell solution and determine its concentration by following the steps provided in respectively section 1.2 and section 1.3. For each gel the choice was made to prepare them with a cell concentration equal to 10^6 cells/mL such that the sedimentation in different gels can easily be compared to each other.

First, the 2.0 mg/mL collagen gels investigated in the confocal microscopy measurements were prepared in an identical way as described in subsection 1.10.1. Subsequently, four ingredients were utilized to prepare the 5 wt% PEG hydrogels:

- 8-arm PEG with a molecular weight equal to 20000 g/mol,
- Dithiothreitol (DTT) with a molecular weight equal to 154.24 g/mol,
- A 0.3 M HEPES[2] buffer solution,
- An initial cell solution of which the cell concentration is known.

First, a 100 mg/mL PEG solution and a 20 mg/mL DTT solution are prepared. Both the 8-arm PEG and DTT are powders, hence both solutions are prepared by mixing the powders with the 0.3 M HEPES buffer solution to obtain a homogeneous suspension. For an irradiation experiment, 600 μL is required to prepare two samples. Half of the solution, i.e. 300 μL, consists of the 100 mg/mL PEG solution and 45 μL out of the total 600 μL consists of the 20 mg/mL DTT solution. The remainder of the volume, which is equal to 255 μL, is a mixture of the cell solution and the HEPES buffer solution such that a concentration equal to 10^6 cells/mL is obtained. Whenever all ingredients are then added together, the DTT will bind to the vinylsulfone groups at the end of each arm of the 8-arm PEG allowing the PEG molecules to be attached to each other such that a gel can be formed.

Lastly, to prepare a 600 μL solution for the hydrogels containing 50% Matrigel, 300 μL of Corning® Matrigel was utilized. The remaining 300 μL consists of a mixture of the cell solution and the nutrient medium discussed in Appendix A with a concentration equal to 2×10^6 cells/mL. That way, the total 600 μL gel solution volume will have a concentration equal to 10^6 cells/mL when the Matrigel is added to the cell solution and nutrient medium mixture.

However, it could be that the cell concentration of the initial cell solution is too low such that the required amount of cell solution to obtain a concentration equal to 10^6 cells/mL would exceed to available volume for the nutrient medium and cell solution combined. If this is the case, the solution needs to be centrifuged first for five minutes at 1500 rounds per minute. Afterwards, part of the cell solution volume is removed from the top such that the concentration of the solution increases. More specifically, assume

[2]HEPES is short for 2-[4-(2-hydroxyethyl)-1-piperazinyl]ethanesulphonic acid [65].

the initial cell solution has a concentration equal to $a \times 10^6$ cells/mL. If the volume of the cell solution is equal to V (expressed in mL) after removing part of the solution from the top after centrifugation, the new cell concentration of the solution will be equal to $\left(\frac{4\text{ mL}}{V} \cdot a\right) \times 10^6$ cells/mL due to the fact that the initial volume of the solution is equal to 4 mL (see section 1.2).

In conclusion, in order to prepare 600 μL of the PEG solution,

- 300 μL of a 100 mg/mL 8-arm PEG solution,
- 45 μL of a 20 mg/mL DTT solution,
- $\frac{600}{a}$ μL of the cell solution (or $\frac{600}{\frac{4\text{ mL}}{V} \cdot a}$ μL after centrifugation),
- 255 μL $-$ $\frac{600}{a}$ μL of the nutrient medium discussed in Appendix A (or 255 μL $-$ $\frac{600}{\frac{4\text{ mL}}{V} \cdot a}$ μL after centrifugation)

is required and to prepare 600 μL of a gel containing 50% Matrigel,

- 300 μL of Corning® Matrigel,
- 300 μL of a mixture containing the cell solution and the nutrient medium discussed in Appendix A such that the cell concentration is equal to 2×10^6 cells/mL

is required where $a \times 10^6$ cells/mL is the concentration of the initial cell solution before centrifugation and V (in units of mL) the volume of the cell solution when part of the initial 4 mL is removed from the top after centrifugation.

2.4.2 Sample Preparation

Two different samples were prepared for each material such that the impact of different refrigeration times on the cell sedimentation could be probed as well:

- One microplate was put into the fridge at 4 °C - 5 °C for one hour and thirty minutes. Afterwards, it was put in an incubator at 37 °C for one hour and thirty minutes.
- One microplate was not put into the fridge, but was immediately placed in an incubator at 37 °C for one hour and thirty minutes.

Only a third sample was prepared as well for the 2.0 mg/mL collagen gels. This third sample was put into the fridge at 4 °C - 5 °C for thirty minutes. Afterwards, it was put in an incubator at 37 °C for one hour and thirty minutes as well.

Each sample of which the cell sedimentation was investigated, was prepared in an identical way by pipetting 100 μL of the gel solution into two different wells of a 8×12 microplate (a Greiner 96 microplate, made from transparent polystyrol). An illustration of the microplate is given in Figure 2.2.

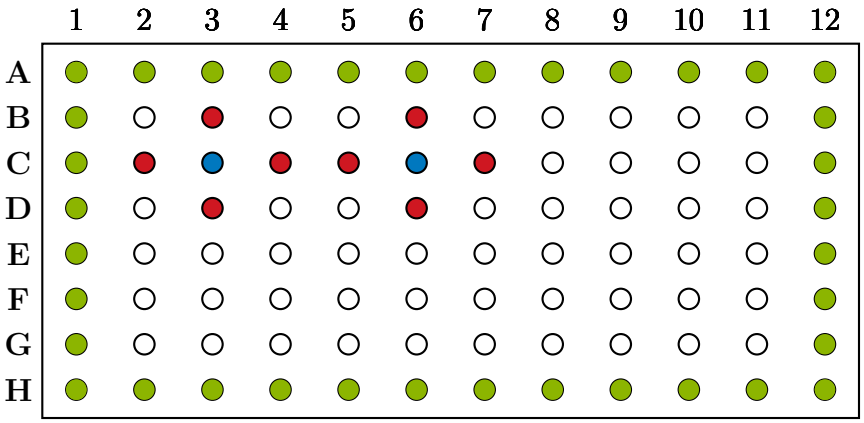

Figure 2.2: *Top view illustration of the microplates that were used for all samples. All wells indicated in red are filled with 100 μL of DPBS. The wells indicated in blue are filled with 100 μL of the gel solution obtained by following the steps in subsection 2.4.1. The wells indicated in green were deliberately not used to avoid cell dehydration.*

The wells indicated in blue in Figure 2.2 each contain 100 μL of the gel solution obtained by following the steps in the previous subsection. The wells indicated in red all contain 100 μL of DPBS to make sure the cells remain hydrated while performing the confocal microscopy measurements. The wells indicated in green were deliberately not used due to the fact that these wells are too close near the edge of the microplate which would increase the risk of cell dehydration. A different microplate was used for each sample.

In a next step, a staining solution was prepared containing 1 mL of DPBS, 2 μL of Calcein AM and 2 μL of Ethidium homodimer such that the cells are visible when imaging the gels. After the samples remained in the incubator for one hour and thirty minutes, 100 μL of the staining solution was pipetted in each well indicated in blue in Figure 2.2. Next, each microplate was placed inside the incubator at 37 °C for an additional hour in order to accelerate the effects of the Calcein AM and the Ethidium homodimer. After the samples remained for one hour in the incubator, the cell sedimentation could be investigated using the confocal microscope.

To ease the discussion of the results in the next section, each investigated sample will be referred to with a letter to indicate the material (i.e., C for collagen, P for PEG and M for Matrigel) and a number to indicate the time (in minutes) the sample remained in the fridge (i.e., 0, 30 and 90).

2.5 Results

The results of the cell sedimentation are shown in Figure 2.3 and Figure 2.4.

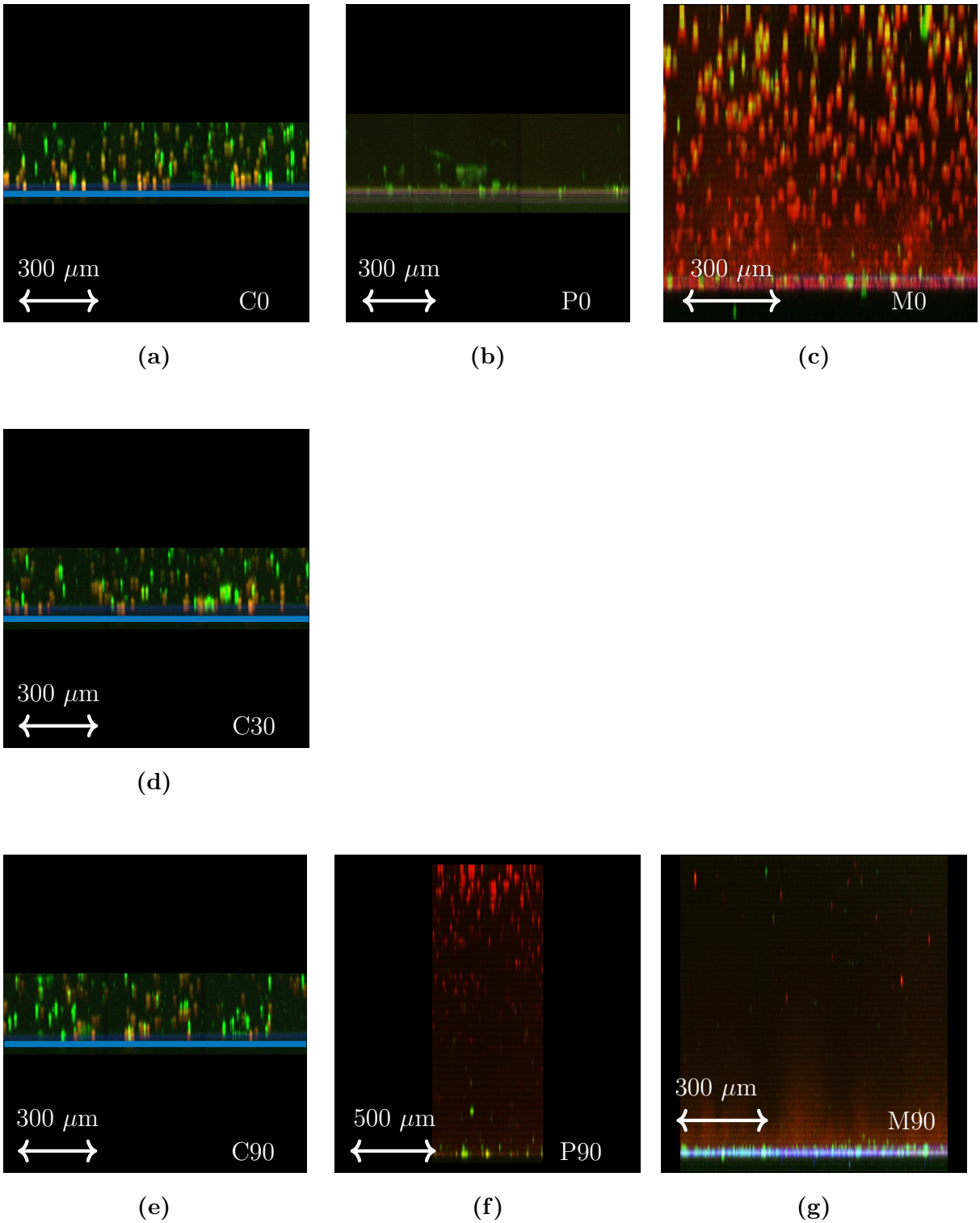

(a) **(b)** **(c)**

(d)

(e) **(f)** **(g)**

Figure 2.3: *A cross section of each gel in which the cell sedimentation was investigated. The first, second and third vertical column corresponds to respectively the collagen, PEG and Matrigel samples. The samples in the first, second and third horizontal row remained in the fridge for respectively 0, 30 and 90 minutes. The cells indicated in green and red correspond to respectively living cells and dead (or dying) cells. The horizontal line in each image corresponds to the bottom of the well. The horizontal blue line in the first vertical column was added manually afterwards.*

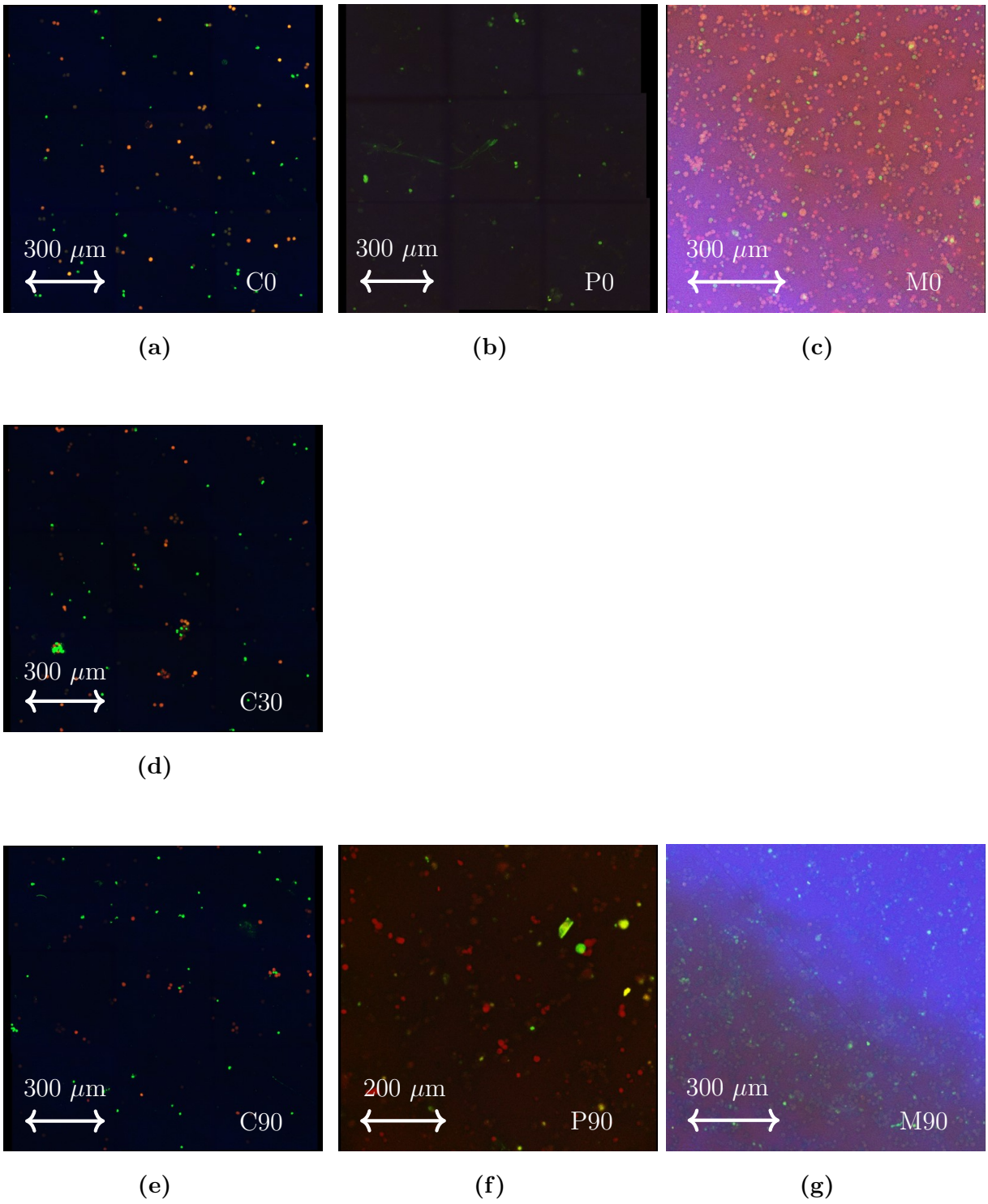

Figure 2.4: *A bottom view of each gel in which the cell sedimentation was investigated. The first, second and third vertical column corresponds to respectively the collagen, PEG and Matrigel samples. The samples in the first, second and third horizontal row remained in the fridge for respectively 0, 30 and 90 minutes. The cells indicated in green and red correspond to respectively living cells and dead (or dying) cells.*

In each image in Figure 2.3, the glass slide can be observed as well: For sample C0, C30 and C90 this is the horizontal blue line in the middle. For sample P0, the glass slide

is not blue but it is also the horizontal line located in the middle. For sample P90, M0 and M90 the slide is located at the bottom near the scale bar. The bottom view of each sample is shown in Figure 2.4. Each image shown in Figure 2.3 was obtained through interpolation using the image processing package Fiji in ImageJ [66].

For samples C0, C30 and C90, 58 focal planes along the z-direction (i.e., the depth of the sample) were measured in total using the confocal microscope. The focal planes are equidistant planes such that the distance between each pair of consecutive planes is equal to 5 μm. The steps taken in the x- and y-direction were both equal to 0.3780 μm resulting in voxels with a volume equal to $0.3780 \times 0.3780 \times 5$ μm^3. Upon comparing the cell sedimentation in samples C0, C30 and C90, barely any difference between the three images can be observed in the sense that all three samples show a poor cell sedimentation. In order for the 2.0 mg/mL collagen gel to be useful for the irradiation experiments, the cells need to be sedimented within a range of approximately 50 μm because otherwise the alpha particles of the ^{241}Am source will not be able to reach the cells inside the gel. However, as can clearly be observed in samples C0, C30 and C90, barely any of the cells properly sedimented. Moreover, the refrigeration time does not seem to affect the cell sedimentation due to the fact that in all three samples the cells did not properly sediment at all and are all scattered inside the collagen gel, even up to a distance of almost 300 μm away from the bottom of the well. Consequently, the 2.0 mg/mL collagen gels cannot be used for the cell-irradiation experiments.

For sample P0, on the other hand, 68 focal planes along the z-direction were measured but the distance between two consecutive focal planes, and the steps in the x- and y-direction, remained unchanged thus resulting again in voxels with a volume equal to $0.3780 \times 0.3780 \times 5$ μm^3. However, in sample P0, only a handful of living cells in green could be observed when examining the sample with the confocal microscope, while almost none of the dead or dying cells in red could be seen. Even in the bottom view shown in Figure 2.4, barely any living cells and none of the dead or dying cells can be observed. A possible explanation for the low cell count is the increased diffusion time of the dyes through the higher density PEG gel, meaning that after one hour incubation, few cells could be imaged. This hypothesis seems to be confirmed upon comparing samples P0 and C0: Both dead and living cells in sample C0 can clearly be observed even though the time between adding the staining and performing the microscopy measurement was exactly the same compared to sample P0. Moreover, comparing the incubation time of samples P0 and P90 seems to confirm this hypothesis as well: The confocal microscopy measurement of sample P0 lasted approximately for one hour and thirty minutes. The second sample (i.e., sample P90) was stained at the same time and remained in the incubator while the first sample was measured. Consequently, the second sample remained in the incubator for approximately two hours and thirty minutes while the staining was already added. It can clearly be seen that the cells in sample P90 are much better visible here compared to the cells in sample P0. Hence, this strengthens the hypothesis that in the first measurement the one hour of incubation after adding 100 μL of the staining solution turned out to be insufficient for both the Calcein AM and the Ethidium homodimer to reach the cells due to the higher density of the PEG.

Consequently, to make sure the sedimentation in sample P90 was thoroughly probed, such that both the cells near the bottom of the plate and the top of the well could all be imaged properly, only 42 different focal planes were measured along the z-direction. However, the choice was made to increase the step size in the x-, y- and z-direction to

investigate a larger volume of the gel. As a result, the volume of a single voxel in the image corresponding to sample P90 was equal to $0.7576 \times 0.7576 \times 50$ μm^3. Nonetheless, a poor cell sedimentation can also clearly be observed in sample P90. Even though some of the cells sedimented well towards the bottom of the well, most of the cells visible are a distance of 1000 μm or more separated from the bottom. In theory, the sample that was placed inside the fridge for one hour and thirty minutes should result in a better cell sedimentation compared to the sample that was immediately placed inside the incubator. This is due to the fact that the low temperature of the fridge should have sufficiently delayed the bonds formed between the DTT and PEG. Hence, allowing more cells to sediment towards the bottom of the well due to the fact that they are hindered to a lesser extent by the bonds formed in the solution. As a result, even though only a limited amount of cells were visible in sample P0, an even poorer cell sedimentation is thus expected here due to the poor sedimentation in sample P90. Consequently, the 5 wt% PEG hydrogels cannot be used for the cell-irradiation experiments either.

Lastly, sample M0 and M90 incubated thirty minutes longer compared to samples C0, C30, C90, P0 and P90 to make sure all cells were stained well and clearly visible. In total, 40 and 55 focal planes were measured for respectively sample M0 and M90. Moreover, the choice was also made to increase the voxel size such that a larger volume of the gel could be investigated. Hence, the step size in both the x- and y-direction was equal to 2.2679 μm and 1.1328 μm for respectively sample M0 and sample M90. The step size in the z-direction was for both images equal to 25 μm resulting in voxels with a volume equal to $2.2679 \times 2.2679 \times 25$ μm^3 and $1.1328 \times 1.1328 \times 25$ μm^3 for respectively sample M0 and sample M90. Upon comparing samples M0 and M90, a clear difference in cell sedimentation can be observed in both samples: The cells inside sample M0 are all scattered up to a distance of 900 μm away from the bottom of the well. Barely any sedimentation can be observed here. On the other hand, upon comparing the cell sedimentation in sample M90, an excellent sedimentation can be observed here. Barely any of the cells are scattered inside the gel.

2.6 Impact of the Sample Preparation Time

On top of the cell sedimentation as discussed in the previous section, it was noticed that the time required for the sample preparation of the collagen hydrogels seems to impact the cell sedimentation as well. More specifically, while preparing the gels following the protocol given in subsection 1.10.1, the last ingredient that was added to the solution was the collagen. The reason for this is that once the collagen is out of the fridge, the temperature of the collagen starts to rise and the crosslinking starts to accelerate. The more bonds that are formed, the more the cell sedimentation will be hindered. Hence, once the collagen is taken out of the fridge, the longer it takes to add it to the samples and then placing the samples in the fridge, the poorer the cell sedimentation will be. The impact of the time in between the moment the collagen is taken out of the fridge and the moment the samples are ready, can clearly be seen in the results shown in Figure 2.5

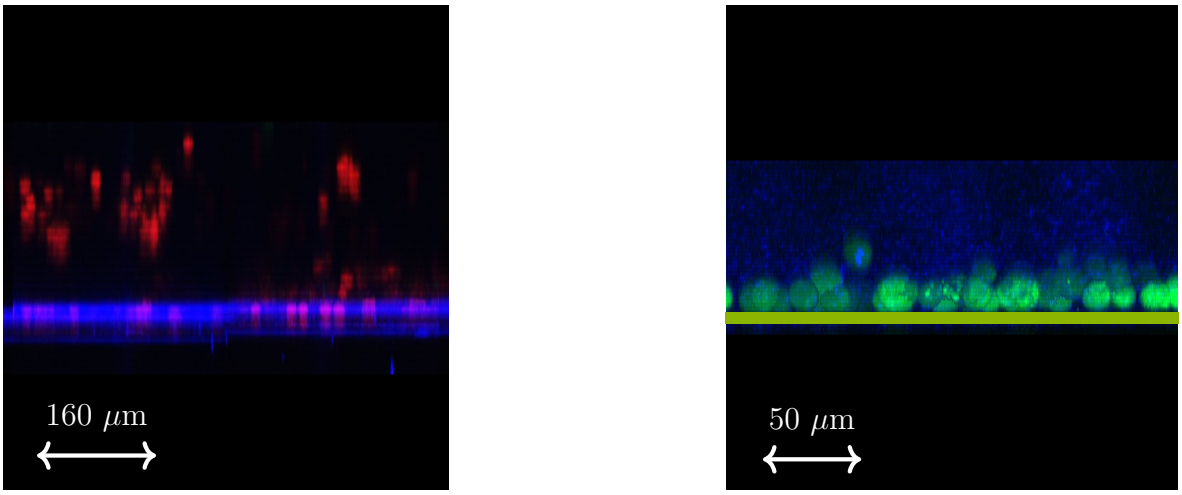

(a) **(b)**

Figure 2.5: *Comparison of the cell sedimentation in a 1.5 mg/mL collagen gel prepared in this project (shown in (a)) to the cell sedimentation in a 1.5 mg/mL collagen gel prepared in Viktor Van den Bergh's master's thesis [2] (shown in (b)). The image shown in (b) was made by Lens Dedroog. The horizontal green line was added manually afterwards to indicate the bottom of the well.*

Both images in Figure 2.5 show the cell sedimentation in a 1.5 mg/mL collagen gel. The sample of which the results are shown in Figure 2.5a were prepared in this project by following the steps given in subsection 1.10.1 (for the gel) and in subsection 2.4.2 (for the sample). However, there was one slight difference in the preparation of this sample compared to the procedure described in subsection 1.10.1: The collagen stock solution was diluted four times, instead of three times, to obtain a collagen concentration of 1.5 mg/mL and the required amounts of 0.1 M NaOH solution, nutrient medium and cell solution were then adjusted appropriately. The horizontal blue line in Figure 2.5a indicates the bottom of the well plate. The result shown in Figure 2.5b were obtained in Viktor Van den Bergh's master's thesis [2]. Here, in this image, the horizontal green line was added manually afterwards to indicate the bottom of the well. The region in blue corresponds to the second-harmonic generation[3] (SHG) signal of the collagen matrix. Both images shown in Figure 2.5a and Figure 2.5b were made using the ImageJ package Fiji [66].

Both samples of which the results are shown in Figure 2.5 were prepared following the exact same protocol with the same collagen batch[4]. This means that the only difference between both measurements was the sample preparation time and thus the time in between the moment the collagen was taken out of the fridge and the moment the samples were ready. However, the cell sedimentation in both images is entirely different: In the image shown in Figure 2.5a, some sedimentation can be observed but most of the cells

[3]More information on second-harmonic generation, and harmonic generation in general, will be provided in subsection 3.2.1.

[4]The characteristics of the collagen, and thus the characteristics of the collagen gels as well, are highly dependent on the batch that is used. The reason for this is that the collagen that is used in this project is extracted from a cow, but due to the fact that there are no two identical cows, the extracted collagen of two different cows will as a consequence also never be exactly the same. For further reference on the variations between different collagen batches, see for example [67] and [68].

still seem to be scattered up to approximately 320 μm away from the bottom of the well. On the other hand, in image Figure 2.5b the cell sedimentation seems to be excellent. Based on the results shown in Figure 2.5, one out of the following two conclusions can be drawn:

1. The success or failure of the cell sedimentation in the collagen gels is highly dependent on the time in between the moment the collagen is taken out of the fridge and the moment the gel solution is pipetted in the Teflon holders and the samples are placed inside the fridge. This first conclusion is based on the fact that the sedimentation is poor in image Figure 2.5a and excellent in image Figure 2.5b. This makes the cell sedimentation in the collagen gels unreliable.

2. The cell sedimentation is poor in both samples, but this cannot be known for sure due to the fact that in the image shown in Figure 2.5b the sedimentation of only a handful of cells was measured up to approximately 100 μm away from the bottom of the well. Hence, it could be that most of the cells are still scattered inside the gel at a distance larger than 100 μm away from the bottom of the well, but were simply not measured.

Nonetheless, both the results discussed in section 2.5 and in this subsection indicate either a poor cell sedimentation in the collagen gels or an unreliable sedimentation due to the fact that it highly depends on the time in between the moment the collagen is taken out of the fridge and the moment the samples are placed in the fridge.

In conclusion, the results given and discussed in this chapter indicate an excellent cell sedimentation in the gels containing 50% Matrigel. Consequently, the hydrogels containing Matrigel will serve as an alternative for the 1.5 mg/mL collagen gels Viktor Van den Bergh used in his master's thesis to perform the cell-irradiation experiments with. This conclusion was based on the fact that the cell sedimentation is excellent in these gels, as the results in Figure 2.3 showed, but also due to the fact that they are approximately equally stiff compared to the 2.0 mg/mL collagen gels (i.e. a linear storage modulus equal to 21.6 Pa for the gels containing 50% Matrigel compared to 20.4 Pa for the 2.0 mg/mL collagen gels). The gels containing Matrigel thus result in a stronger and more stiffer gel compared to the 1.5 mg/mL collagen gels. That way, less damage to the cells inside the gels is expected in the cell-irradiation protocol, besides the damage caused by irradiation.

"I'm not superstitious but I am a little stitious."
Michael Scott – The Office

3 Modifying the Cell-Irradiation Protocol

In this chapter, the second and third hypothesis stated near the end of section 1.10 will be addressed. In the first part of this chapter, a new approach will be discussed to perform the Resazurin assays without the need to remove the hydrogels from the Teflon holders after an irradiation experiment is performed. That way, additional gel manipulations during the irradiation experiments are reduced to a minimum such that additional damage caused to the cells inside the gel is reduced to a minimum as well. More details on this new approach will be provided in section 3.1.

In the remainder of this chapter, the gel adhesion to the glass slides will be discussed. More specific, after having described the fundamentals of multiphoton microscopy in subsection 3.2.1, the results of a multiphoton microscopy measurement will be shown first in subsection 3.2.2 to probe to what extent the cells in the gel adhere to the glass slide upon removing it. Subsequently, in section 3.3, the results of eight potential solutions are given to prevent the gel and cells from adhering to the glass slide. Lastly, in section 3.4, the result of a new multiphoton microscopy measurement is shown that was performed to probe the effectiveness of the most promising solution from the previous section.

3.1 Reducing the Gel Manipulation to a Minimum

3.1.1 A New Approach to Perform the Resazurin Assays

The main source of damage caused to the cells, in addition to the irradiation, is thought to be due to the manipulation of the gels with the tweezers after irradiation to perform the Resazurin assay. Hence, to reduce the additional damage caused to the cells to a minimum, this step in the protocol was modified by devising a new approach to perform the Resazurin assays. This new approach is shown in Figure 3.1.

(a) **(b)**

Figure 3.1: *Illustration of the new approach to perform the Resazurin assays. The picture in (a) shows a top view of the larger part of the Teflon holder where a small O-ring with a diameter equal to 1.6 cm is placed around the circular well at the center where the gel is located. That way, a small volume is created when (1) the smaller piece of the Teflon holder is tightened on top of the lager part using the three screws with the O-ring in between and (2) the four holes on the bottom of the holder are sealed. In the small volume that is created because of this, the Resazurin, indicated in purple in the illustration in (b), can be added on top of the gel.*

Instead of taking the gel out of the holder, it remains in the well at the center. Around the gel, an O-ring with a diameter equal to 1.6 cm is added (see Figure 3.1a) such that a small volume is created when the smaller part of the Teflon holder is re-attached to the larger part by re-using the three small screws. That way, the Resazurin solution can be added immediately on top of the gel as shown in Figure 3.1b. The four holes in the bottom of the well (see Figure 3.1a) are sealed as well to avoid leakage of Resazurin through the holes into the plastic Petri dish underneath the Teflon holder. This Petri dish is indicated in bold in Figure 3.1b. Moreover, on top of these modifications, the Matrigel concentration in the hydrogels was also increased from 50% up to 60% to obtain a stiffer gel to make sure the gel remained in the center of the Teflon holder when removing the glass slide. In comparison, both the hydrogels containing 50% Matrigel (see section 2.2) and the 2.0 mg/mL collagen gels that were prepared at the start of this project (see subsection 1.10.1) did not always remain in the well in the middle of the holder upon removing the glass slide and needed to be pushed back a bit towards the center. Hence, resulting in additional gel manipulations. Consequently, by increasing the Matrigel concentration from 50% up to 60%, the stiffness of the gel almost doubles, as the linear storage modulus increases from 21.6 Pa up to 48.3 Pa, such that the hydrogel perfectly remains in the middle of the holder upon removing the glass slide. That way, less additional manipulation of the gel is required and thus less additional damage to cells will be caused.

To test this new approach to perform the Resazurin assays, four samples were prepared by following the cell-irradiation protocol discussed in chapter 1. The gel inside all four Teflon holders was a gel containing Matrigel that was prepared by following the steps given in subsection 2.4.1 with the exception that it contained 60% Matrigel instead of

50%. The four holes on the bottom of the holder were sealed using plastic tape. However, in three of the samples, there was leakage of the Resazurin due to failure of the tape, the O-ring seal or both. Nonetheless, in the fourth sample, neither the tape nor the O-ring failed to do its job. In this sample the Resazurin had not leaked out of the small volume which indicates this new approach does seem to work, if properly executed.

3.1.2 Modifications Made to the Teflon Holders

The fourth sample indicated that the adjustments to the protocol show potential as an alternative approach to avoid additional gel manipulations if the holes on the bottom are properly covered and the smaller part of the holder is tightly enough attached to the larger part. Hence, more modifications were made, but this time to the Teflon holders, to make sure both of these requirements are met. However, before all four Teflon holders were modified, adjustments were only made to one holder such that the changes could be tested first.

First, the holes that were used for the small screws were made deeper and wider such that three long screws could be inserted instead, all the way through the holder. That way, a 3 mm thick stainless-steel plate could firmly be attached to the bottom of the holder using three bolts. Next, in between the bottom of the holder and the plate, a piece of parafilm is placed to make sure the four holes are tightly sealed. An illustration and some images of the adjustments are shown in Figure 3.2.

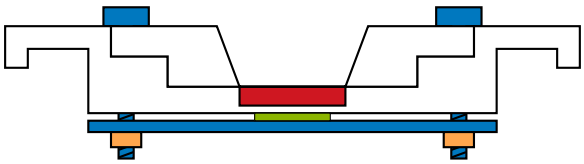

(a)

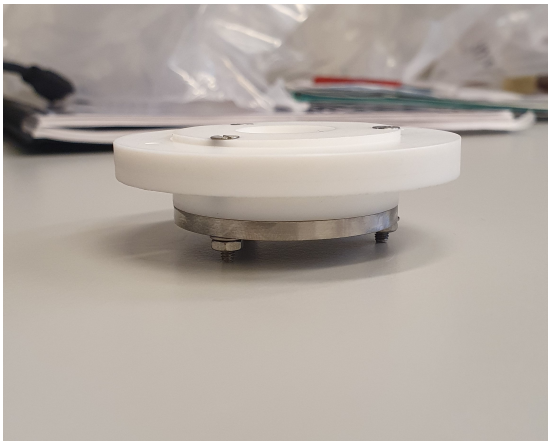

(b)

(c)

Figure 3.2: *A schematic illustration and some images of the adjustments made to the first Teflon holder. In (a), a schematic illustration is shown where the hydrogel is indicated in red, the screws and stainless-steel plate in blue, the parafilm in green and the bolts in orange. The images in (b) and (c) respectively show a side and bottom view of the adjusted holder.*

Subsequently, the adjustments made to the holder were tested. This was done by adding 1 mL of nutrient medium in the small volume, above the four holes, were the hydrogel is supposed to be. The holder was then placed in the incubator for an entire night. The day after, none of the nutrient medium had leaked out of the holder indicating the adjustments that were made worked.

However, when testing these changes, it was noticed that further modifications were still required. For example, the first change that was required, is an alternative for the bolts to tighten the smaller part of the holder to the larger part. The bolts are simply too small to properly handle them with gloves on in the fume hood. Hence, for the remaining three samples, instead of regular holes in the stainless-steel plate, different holes were drilled such that the long screws can directly be screwed and tightened into the plate without the need for additional bolts. Secondly, instead of drilling deeper and wider holes for the screws, only deeper holes were drilled in the other three holders. The reason for this, is that the longer screws are not practical to work with for the cell sedimentation when a glass slide is placed between both parts of the holder. Hence, with this additional change, the small screws can still be used for the cell sedimentation and the long screws for the Resazurin assay.

In conclusion, by increasing the amount of Matrigel from 50% to 60% and by changing the cell-irradiation protocol such that the Resazurin assay can be performed inside the holders as indicated in Figure 3.1, additional gel manipulations (and thus additional damage) was reduced to a minimum.

3.2 Gel adhesion to Glass Slides

In the remainder of this chapter, the third and final hypothesis stated at the end of chapter 1 will be discussed regarding the gel adhesion to the glass slides. In this section, the results of a multiphoton microscopy measurement will be discussed that was performed

to probe the severeness of the problem. Adhesion of gel fragments to the glass slide could be observed without a microscope, but the goal of the multiphoton microscopy measurement was to investigate to what extent the cells adhere to the glass slide as well upon removing it.

To investigate this problem, a sample was prepared by following the steps of the cell-irradiation protocol described in section 1.2 up to section 1.4, but the glass slide was not removed yet. The gel inside this sample was a gel containing Matrigel that was prepared by following the steps given in subsection 2.4.1 with the exception that it contained 60% Matrigel instead of 50%. Next, three different measurements were performed:

1. First, the cell sedimentation, before removing the glass slide, was investigated.
2. Next, the glass slide was removed and the gel fragments on the slide were imaged.
3. Finally, the remaining gel inside the holder was imaged as well.

However, before the results of these three measurements will be discussed, a brief overview on the basic principles of multiphoton microscopy will be given first.

3.2.1 Multiphoton Microscopy

Multiphoton microscopy makes use of harmonic generation to form images. The basic principle behind harmonic generation is shown in Figure 3.3.

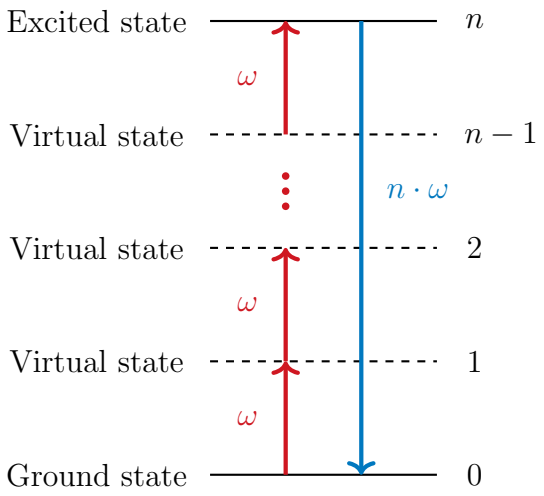

Figure 3.3: *An illustration showing the basic principle behind harmonic generation. Second-harmonic generation (SHG) is when $n = 2$, while third-harmonic generation (THG) is when $n = 3$.*

Whenever a sample is irradiated at a high rate with low energy photons, there is a chance that multiple photons are absorbed at once. This principle is illustrated in Figure 3.3 where n low-energy photons with angular frequency ω are absorbed to excite an electron to an excited state by making use of virtual states at a lower energy. The photon that is emitted afterwards, after de-excitation, has an angular frequency that is in theory equal to $n \cdot \omega$. However, in practice, the energy of the emitted photon is slightly lower compared to the energy of the n absorbed photons combined. The reason for this,

is that the electron in the excited state often de-excites first towards a lower energy level as a consequence of non-radiative relaxation (see Appendix B). Hence, the photon that is emitted as a result of de-excitation towards the ground state often has a slightly lower energy and thus a slightly lower angular frequency compared to the value $n \cdot \omega$ [69].

As stated earlier, multiphoton microscopy makes use of low-energy photons, meaning the photons have a rather long wavelength. Typically photons in the infrared region with a wavelength in between ±700 nm and ±1000 nm are used. The main advantage of low-energy photons is that (1) there is less adsorption by water and (2) these photons scatter to a much lesser extent resulting in a much deeper penetration in the sample compared to, for example, the single photon confocal microscopy measurements that were performed to obtain the results shown in chapter 2 [69].

The results that will be shown in the next section were obtained by using an Olympus BX61 WI-1200-M system. In each measurement, the sample was irradiated using linear polarised light where the photons had a wavelength equal to 1140 nm. The photons that were measured, were mainly second-harmonic-generation (SHG) photons (i.e., $n = 2$) and to a lesser extent third-harmonic-generation (THG) photons (i.e., $n = 3$).

3.2.2 Results

The result of the first measurement, i.e. the measurement were the cell sedimentation of the gel inside the holder was probed before removing the glass slide, is shown in Figure 3.4.

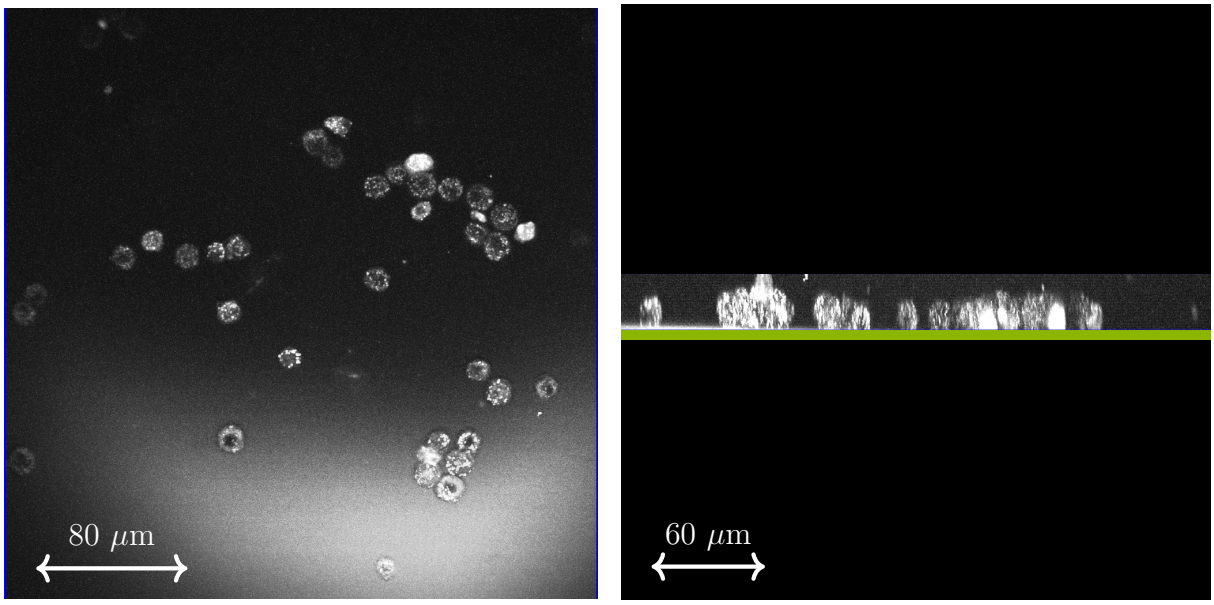

(a) **(b)**

Figure 3.4: *Results of the first measurement where the cell sedimentation inside the Teflon holder, before removing the glass slide, was investigated using multiphoton microscopy. The image in (a) shows a top view where clearly cells in the top layer of the gel, near the glass slide, can be observed. The image in (b) shows a cross section of the gel. The green line was manually added afterwards to highlight the position of the glass slide.*

Both images in Figure 3.4 show the cell sedimentation inside the holder before the

glass slide is removed. The illustration shown in Figure 3.4b is an image of the cells near the glass slide along the z-axis, i.e. the axis along the depth of the gel. Figure 3.4b was created by combining 60 equidistant focal planes into a single image through interpolation by using the image-processing package Fiji in ImageJ [66]. The distance between two consecutive pairs of focal planes was equal to 0.5 μm. The steps taken in the x- and y-direction were both equal to 0.31 μm, thus resulting in voxels with a volume equal to $0.31 \times 0.31 \times 0.5$ μm^3. The green line in the image in Figure 3.4b was added manually afterwards to highlight the position of the glass slide. By utilizing brightfield microscopy[1], it was observed that there were no cells in the gel beyond what is displayed in Figure 3.4b meaning all the cells sedimented well as a result of the Matrigel that was utilized and are now in the top layer of the gel.

In a next step, the glass slide was removed and both the slide and the remaining gel were imaged. The result of both of these measurements is shown in Figure 3.5.

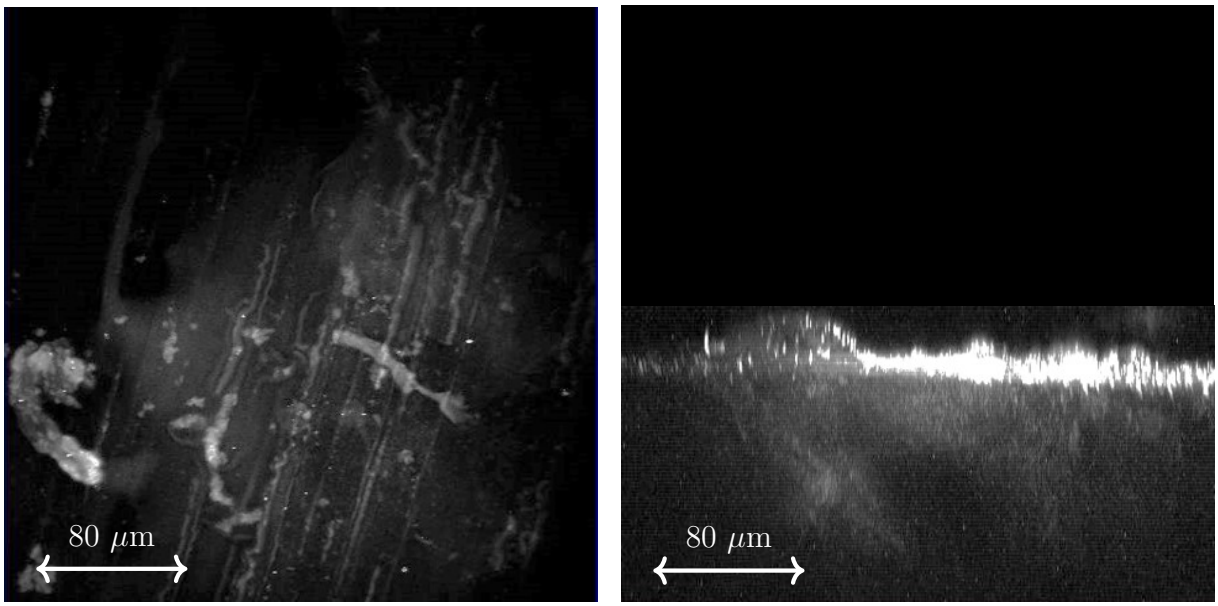

(a) **(b)**

[1]In brightfield microscopy, a sample is irradiated with bright, white light that travels through the sample onto a detector. The attenuation of the emitted light depends on the density of the material: More light is attenuated in denser regions compared to less denser regions which results in an image. Contrast in the observed image can, for example, be increased by using linear or circular polarized light [70].

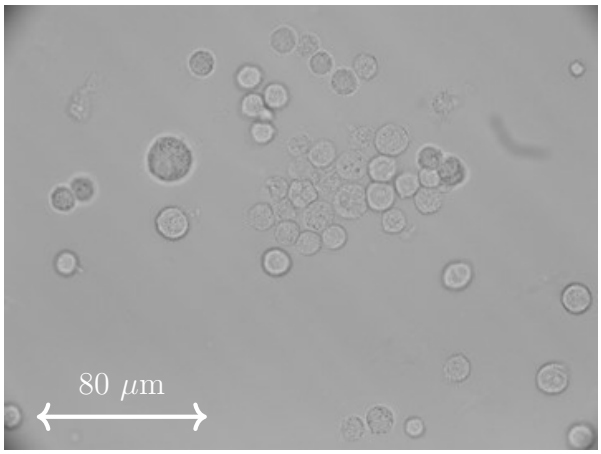

(c)

Figure 3.5: *Results of the second and third measurement where respectively the remaining gel in the holder and the glass slide after removal were imaged. In (a), clear tears in the gel and very few cells can be observed after removing the glass slide. In (b), a cross section of the remaining gel in the holder is shown where clearly an uneven surface can be observed as a consequence of the glass removal. In (c), an image of the glass slide is shown where many cells can be observed.*

Both images in Figure 3.5a and Figure 3.5b were also created through interpolation using the image-processing package Fiji in ImageJ [66]. In total, 83 equidistant focal planes were measured. The distance along the z-direction between each pair of consecutive focal planes was equal to 2 μm. The steps in the x- and y-direction were both equal to 0.621 μm thus resulting in voxels with a volume equal to $0.621 \times 0.621 \times 2$ μm^3. The image of the glass slide shown in Figure 3.5c was not created through interpolation, but was directly taken by the multiphoton microscope.

The image in Figure 3.5a shows a top view of the gel after the glass slide is removed. Clear tears can be observed as a consequence of the glass removal, but barely any cells. The image in Figure 3.5b shows a cross section of the remaining gel. A clear uneven surface can be observed in this image here as a consequence of the glass removal. On the glass slide shown in Figure 3.5c, many cells can be seen which seems to confirm the hypothesis that the cells are indeed torn off from the gel when the slide is removed in the cell-irradiation protocol, right before irradiation.

3.3 Preventing Gel Adhesion to the Glass Slides

In order to prevent gel adhesion to the glass slides, eight potential solutions were probed in this project: The first potential solution was to make use of glass slides that are thoroughly cleaned in a piranha solution. A piranha solution is an extremely corrosive solution and consists of a mixture between sulfuric acid and hydrogen peroxide. By cleaning the glass slides in a piranha solution, all oily substances are removed from the glass and might prevent gel adhesion. The second and third potential solution that were tested, consisted of providing the glass slides with a coating after having them cleaned first in a piranha

solution. Two different coatings were tried: A Jeffamine® M-600[2] coating and a PEG-silane[3] coating. Subsequently, two additional PEG coatings were prepared for the next four potential solutions: The first coating was a PEG diacrylate (PEGDA) coating that was crosslinked using 405 nm ultraviolet (UV) light. The second coating was a PEG and DTT mixture that was prepared in a similar way as described in subsection 2.4.1, but prepared on three different surfaces: On a Teflon plate, on a piece of Teflon tape and on a piece of parafilm. Lastly, in addition to the coatings and the piranha-cleaned glass slides, one slide was also wrapped in Teflon tape to test as well. More details on the preparation of the coatings will be provided in the next section.

3.3.1 Preparation of the Glass Slides

For the first three potential solutions, all of the glass slides where first thoroughly cleaned in a piranha solution. The ratio sulfuric acid : hydrogen peroxide was equal to 2 : 1. After the glass slides remained for 20 minutes in the piranha solution, the slides were rinsed multiple times with water that had undergone reverse osmosis and were dried. Once the slides are thoroughly cleaned, the Jeffamine® M-600 and PEG-silane coating were added.

To prepare the Jeffamine® M-600 coating on the glass slides, the inside of a plastic bowl was rinsed first with 10 mL of toluene. The toluene was then removed from the plastic bowl and 10 g of water that has undergone reverse osmosis was added. For an optimal coating, a 1 mg/mL concentration Jeffamine® M-600 is required. Hence, 102 μL was added due to the fact that the density of Jeffamine® M-600 is equal to 0.98 g/mL at 25 °C [71]. Once the 102 μL was added to the 0.1 g water in the plastic bowl, the solution was pipetted multiple times in and out to make sure the rather viscous Jeffamine® M-600 was thoroughly mixed with the water. In a next step, the glass slides were added to the solution and remained there for 18 hours. After these 18 hours, the slides were taken out and dried.

To prepare the PEG-silane coating, 10 mL of toluene was added to a bowl made out of glass. For an optimal coating, 5.5 μL PEG-silane per 1 mL toluene is required. Hence, 55 μL was added to the 10 mL toluene inside the bowl. Next, the glass slides were added to the solution and the lid of the bowl was sealed off with parafilm. The glass slides remained in the solution for 18 hours as well. After 18 hours, the slides were rinsed multiple times, each time with a different solution to avoid residues on the slides once they are dry. First, all glass slides were rinsed with toluene and placed in a second bowl. Next, each slide from the second bowl was rinsed first with acetone, then with methanol and then with water. After the slides were rinsed with water that had undergone reverse osmosis, they were dried as well. Finally, in the last step of the preparation, the slides were heated at 110 °C to make sure an optimal crosslinking is obtained.

The PEGDA coatings were prepared by adding 4 μL of a 50 wt% PEGDA solution, together with 12 μL of water that has undergone reverse osmosis as buffer and 4 μL of a 2.5 wt% lithium phenyl-2,4,6-trimethylbenzoylphosphinate (LAP) solution. The LAP solution is a photoinitiator, meaning that upon exposure to 405 nm UV light, free radicals will be created. Consequently, the PEGDA will be able to start crosslinking and a hydrogel

[2]A synonym for Jeffamine® M-600 is polypropylene glycol 500 mono-2-aminoethyl mono-2-methoxyethyl ether.

[3]The PEG-silane coating that was used in this project is 2-[Methoxy(polyethyleneoxy)propyl]trimethoxysilane; 90 wt%, consisting of 6-9 PEG-units.

layer will be formed on top of the glass slides [72]. The glass slides on which the PEGDA coatings were prepared, were already provided with a methacrylate-silane layer to make sure the PEGDA coating is firmly attached [73].

Subsequently, a coating containing 8-arm PEG with vinylsulfone groups at the end of each arm mixed with DTT as described in subsection 2.4.1 was prepared. However, there was one key difference: Instead of a 5 wt% PEG concentration, the choice was made to prepare a 7.5 wt% PEG gel to obtain a stronger hydrogel[4]. This means the quantities mentioned in subsection 2.4.1 need to be slightly altered: To obtain a volume equal to 20 μL for the coating, 15 μL of the PEG and HEPES mixture, and 2.25 μL of the DTT and HEPES mixture were added together. Next, to prepare the glass slides, a 10 μL droplet of the PEG and DTT mixture was pipetted on a surface and a glass slide was placed on top of it. Afterwards, the surface with the glass slide on top of it was placed in the incubator at 37 °C for thirty minutes to accelerate the crosslinking. Multiple coatings were prepared, but each time a different surface was used to probe the impact of a smooth surface compared to a more uneven surface. In total, three different surfaces were used: Parafilm, Teflon plate and a piece of Teflon tape. Each of the glass slides that was coated with a PEG layer was already provided with a 3-Aminopropyltriethoxysilane (APTES) coating. The purpose of the APTES coating is similar compared to the methacrylate-silane coatings which is to make sure the PEG layer is firmly attached to the glass slides.

Lastly, all eight potential solutions were tested by preparing eight samples containing a gel with 60% Matrigel and 40% of the nutrient medium discussed in Appendix A. The results are given and discussed in the next section.

3.3.2 Results

The results are shown in Figure 3.6.

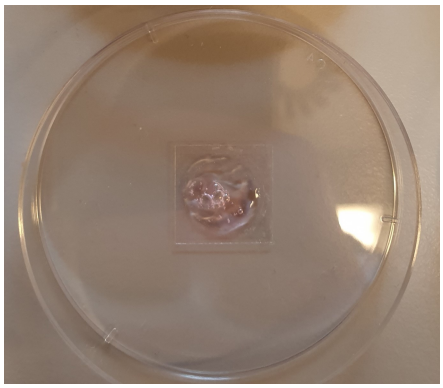

(a)

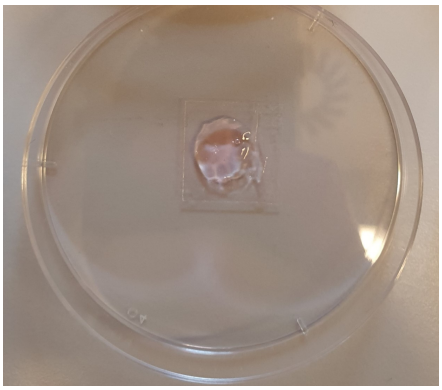

(b)

[4]The higher the PEG concentration, the more crosslinks will be formed in the gel and thus the stiffer the gel will be. This means a linear storage modulus larger than 3788.3 Pa is expected.

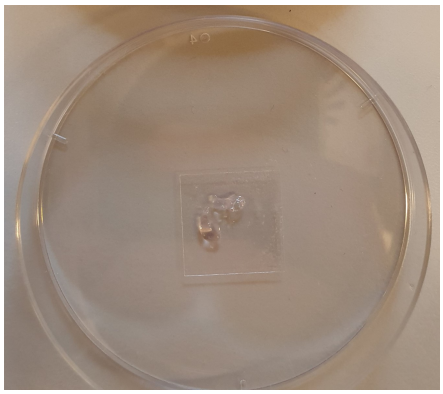

(c)

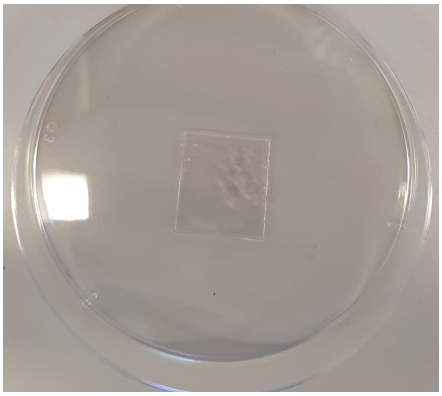

(d)

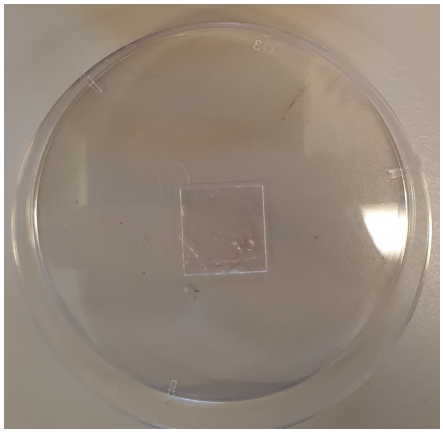

(e)

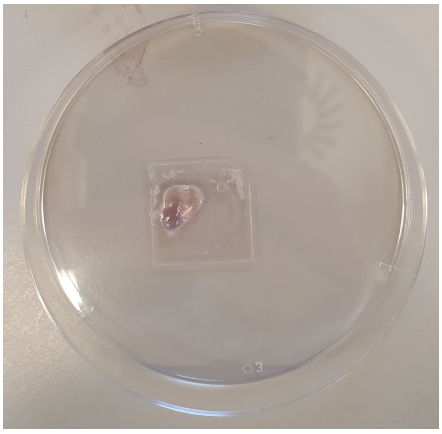

(f)

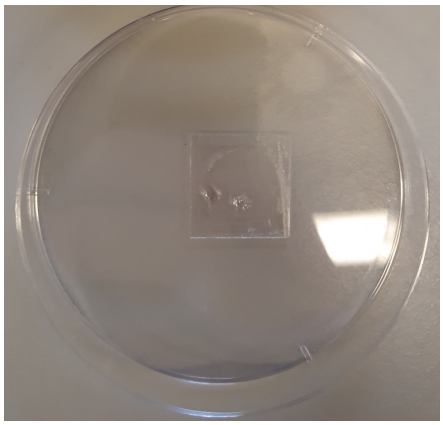

(g)

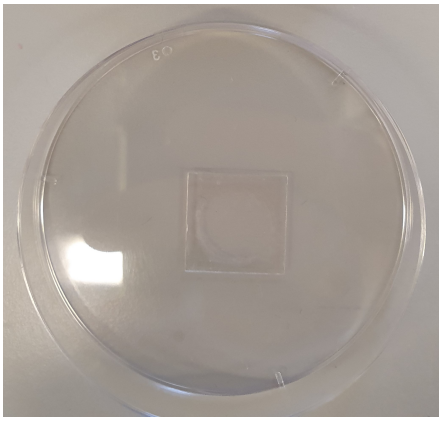

(h)

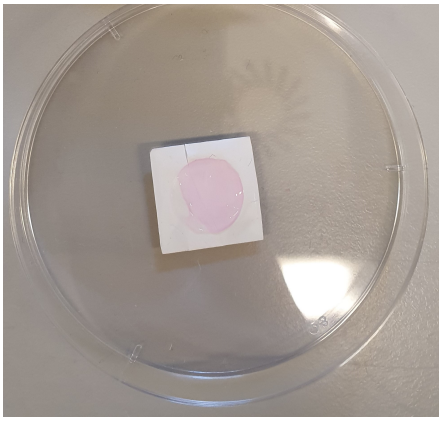

(i)

Figure 3.6: *The results of all eight potential solutions to prevent gel adhesion to the glass. Image (a) shows the glass slide cleaned in a piranha solution. Images (b) and (c) show a glass slide cleaned in a piranha solution and provided respectively with a Jeffamine® M-600 and PEG-silane coating. Both images (d) and (e) show a methacrylate-silane covered glass slide provided with an additional PEGDA coating. Images (f) up until (h) show an APTES coated glass slide provided with an additional PEG and DTT coating respectively prepared on a Teflon plate, a piece of Teflon tape and a piece of parafilm. Finally, image (i) shows the result of the glass slide wrapped in Teflon tape.*

Out of these eigth potential solutions, both the methacrylate-silane covered glass slides provided with an additional PEGDA coating (Figure 3.6d and Figure 3.6e) and the APTES coated glass slide provided with an additional PEG and DTT coating prepared on a piece of Teflon tape (Figure 3.6g) seemed to prevent gel adhesion to some extent. However, only the APTES coated glass slide provided with an additional PEG and DTT coating prepared on a piece of parafilm (Figure 3.6h) completely prevented gel adhesion. The reason for this might be a result of the unevenness of the surface on which the coating was prepared: Both slides in Figure 3.6g and Figure 3.6h are provided with the same coating, but the uneven parafilm surface seems to prevent gel adhesion to a greater extent compared to the more smooth surface of the Teflon tape.

3.4 Verification With Multiphoton Microscopy

No adhesion of gel fragments could be observed upon removing the APTES coated glass slide provided with an additional PEG and DTT layer prepared on a piece of parafilm. Nonetheless, an identical multiphoton microscopy measurement was performed, as described at the start of section 3.2, to probe to what extent the cells adhere to the glass. The results of the first measurement, where the cell sedimentation is investigated in the Teflon holder before removing the glass slide, are shown in Figure 3.7.

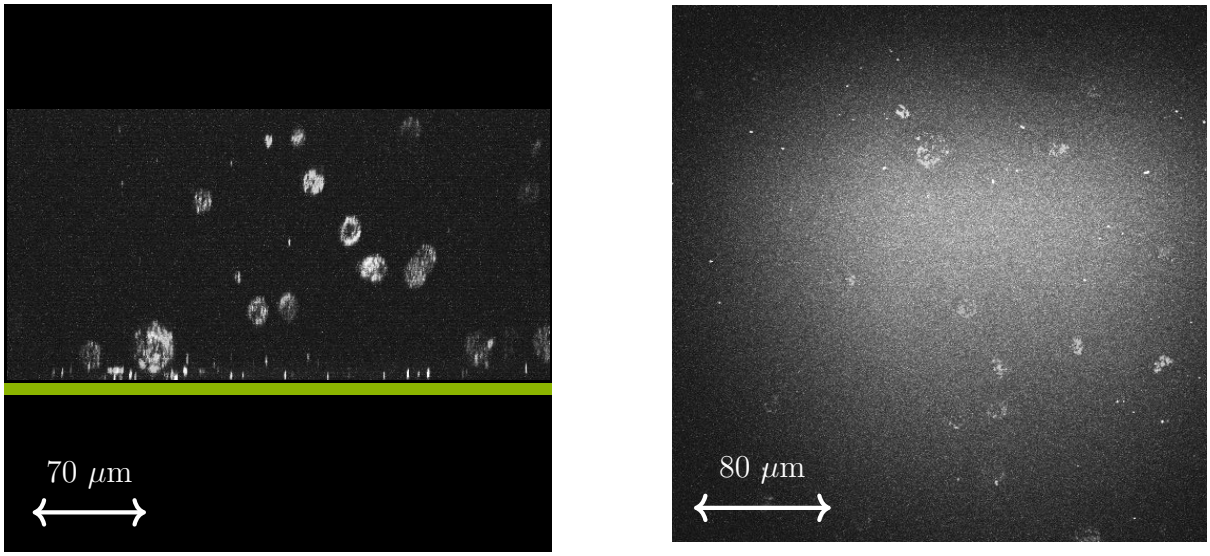

(a) **(b)**

Figure 3.7: *The results of the first measurement in which the cell sedimentation in the Teflon holder was investigated before removing the glass slide. The image in (a) shows a cross section of the gel, while the image in (b) a bottom view. The horizontal green line in (a) was added manually afterwards to indicate the position of the glass slide.*

Even though a clear cell sedimentation can be observed, the sedimentation is poorer compared to the results in earlier measurements such as for example in Figure 2.3 and Figure 3.4. The reason for this could be due to the temperature in the lab: Both measurements of which the results are shown in Figure 2.3 and Figure 3.4 were performed during winter. However, the measurement of which the results are shown in Figure 3.7 was performed during the spring, after a warm weekend (i.e., ±24 °C) thus resulting in a higher temperature in the lab. An increase in temperature heavily impacts the gel formation in a hydrogel containing Matrigel, as was discussed in section 2.2, even though all experiments were performed while working on ice. Hence, this could explain the difference in cell sedimentation.

Subsequently, the glass slide was removed and both the slide and the remaining gel were imaged. The result is shown in Figure 3.8. Only a few cells could be observed in the region of the gel of which the cross section is shown in Figure 3.8a. Nonetheless, APTES coated glass slides provided with an additional PEG and DTT coating does seem to prevent both gel and cell adhesion: Only a few cells (in Figure 3.8b and Figure 3.8c) and tiny gel fragments (in Figure 3.8c and Figure 3.8d) could be observed. Overall, a large improvement can be seen here compared to the image in Figure 3.5.

In conclusion, based on the results shown and discussed in this section and the previous section, the glass slides will be coated first with an APTES layer and provided afterwards with an additional PEG and DTT coating prepared on a piece of parafilm to prevent gel adhesion to the glass slides when a new cell-irradiation experiment is performed.

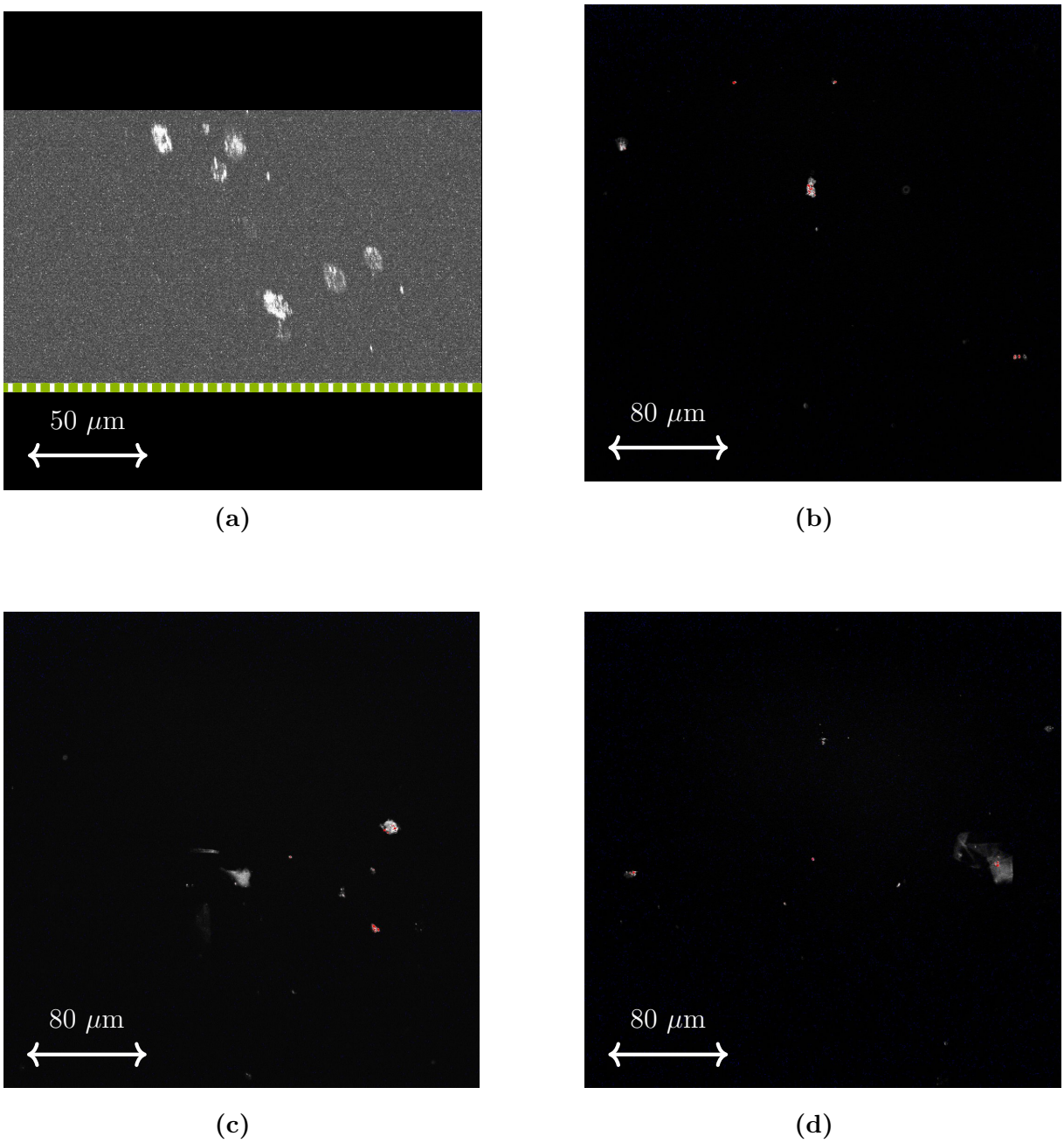

(a) **(b)**

(c) **(d)**

Figure 3.8: *The result of the second and third measurement. The image in (a) shows a cross section of the gel after removing the glass slide. Images (b), (c) and (d) show the glass slide on three different locations after it was removed. The dashed green line in (a) indicates where the glass slide was located before removing it.*

"Would I rather be feared or loved? Both, I want people to be afraid of how much they love me."

Michael Scott – The Office

4

Post-Modification Cell-Irradiation Experiments

In chapter 2, the issue regarding the cell sedimentation was discussed and a solution was obtained by utilizing hydrogels containing Matrigel. In chapter 3, the gel manipulation was reduced to a minimum by modifying the Teflon holders and increasing the Matrigel concentration from 50% up to 60%. That way, the Resazurin assays in the cell-irradiation protocol can be performed while the gels remain in the holders. Moreover, the regular glass slides were interchanged with APTES coated glass slides provided with an additional PEG and DTT layer, prepared on a piece of parafilm, to prevent the gel and cells from adhering when removing the glass slide. All three hypotheses stated at the end of section 1.10 were thus investigated and a solution for these issues was provided. Hence, with these modifications, two new irradiation experiments were performed.

First, in section 4.1, a brief overview of the sample preparation will be provided together with an additional adjustment made to the DIRAC setup. Subsequently, in the remainder of this chapter, the results of the two new irradiation experiments will be shown and discussed.

4.1 Sample Preparation and Adjustments to the Setup

In a similar way as explained in section 1.2 up to section 1.4, four samples were prepared: One sample that was irradiated for thirty minutes, one sample that was irradiated for one hour and one additional control sample for each of the two measurements. The solution that was pipetted into the Teflon holders, through one of the four holes on the bottom (see Figure 1.5), contained 60% Matrigel. The remaining 40%, consisted of a nutrient medium and cell solution mixture such that a concentration of 10^6 cells/mL is obtained, in a similar way as discussed in subsection 2.4.1. Subsequently, APTES coated glass slides provided with an additional PEG and DTT layer, prepared on a piece of parafilm, were used for each of the samples. The samples were then placed one hour and thirty minutes in the fridge, at 4 °C - 5 °C, to make sure the cells are able to sediment well. Afterwards,

the samples were placed for 105 minutes[1] in the incubator, at 37 °C, to accelerate the crosslinking. Finally, after irradiation, the Resazurin assays were performed using the new approach discussed in the previous chapter.

In addition, the plastic foil around the setup (see Figure 1.8a) was replaced by a plastic box with multiple holes made on the top. The goal of the plastic box is also to make sure cell dehydration is limited to a minimum, but now the box is not touching the Teflon holders which was the case when the plastic foil was used. Moreover, with the plastic box, a more constant and steady airflow could be provided to avoid condensation on the source. An image of the adjusted setup is shown in Figure 4.1.

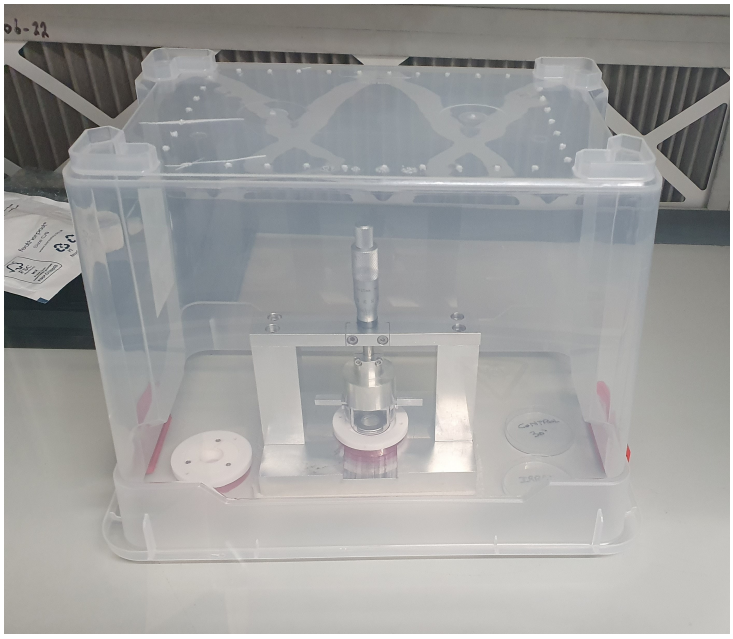

Figure 4.1: *An image of the DIRAC setup when the plastic foil is replaced by the plastic box.*

4.2 Results

The results of the first irradiation experiment with the modified cell-irradiation protocol, after having applied the fluorescence calibration (see section 1.9), are shown in Figure 4.2.

[1]The samples thus remained fifteen minutes longer in the incubator compared to previous gel preparations. This was to make sure a firm gel was obtained for the irradiation experiments.

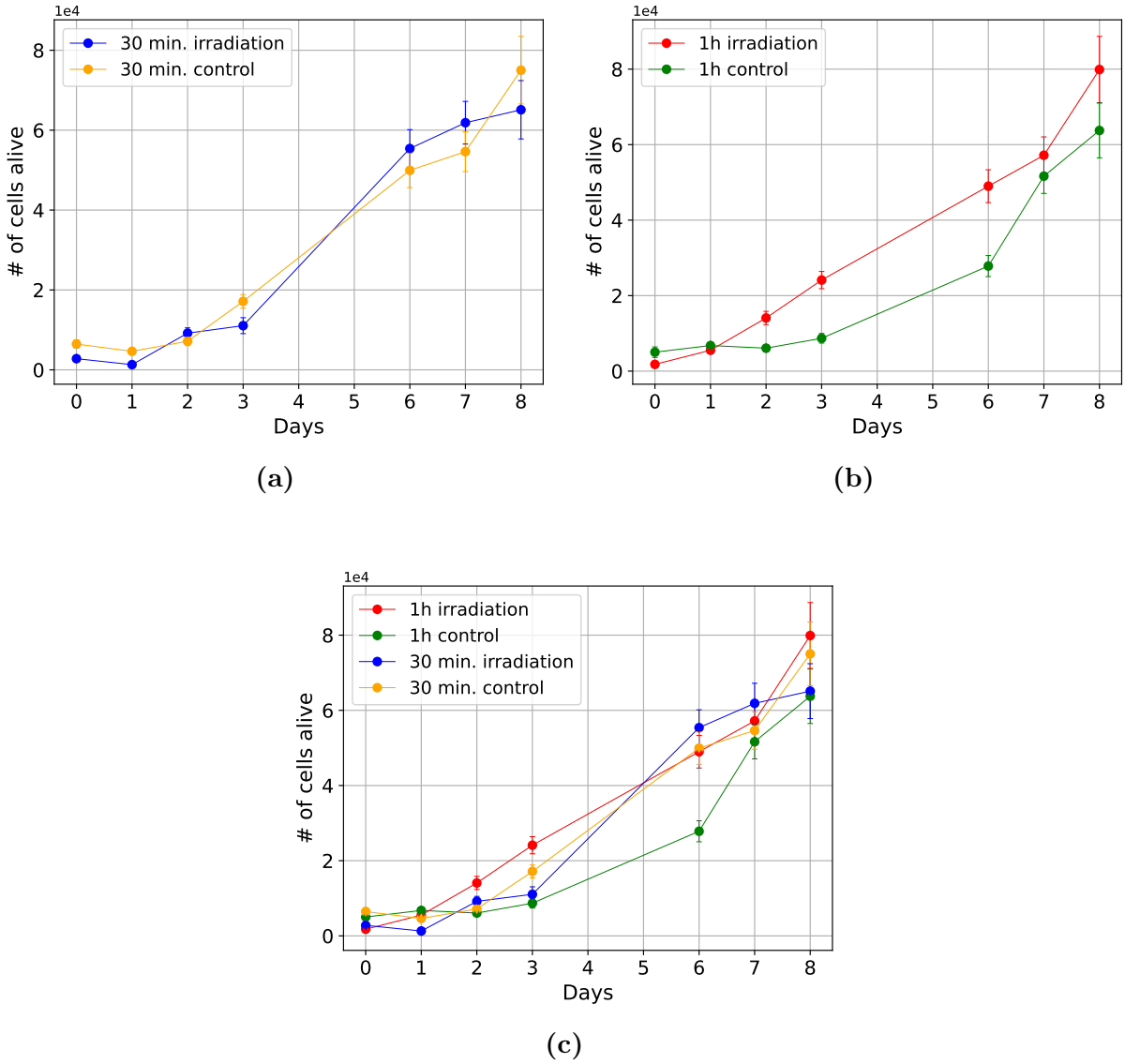

Figure 4.2: *The results of the first irradiation experiment with the modified protocol. The graph in (a) shows the sample that was irradiated for thirty minutes together with the corresponding control sample. The graph in (b) shows the sample that was irradiated for one hour together with the corresponding control sample. The graph in (c) shows the result of all four samples combined.*

The results are not entirely in accordance with what is expected: In graph Figure 4.2a, only a small difference between the irradiated and control sample can be observed over the subsequent eight days following the measurement. Moreover, on days 2, 6 and 7 the irradiated sample even indicates a higher number of cells alive compared to the control sample. The graph in Figure 4.2b, on the other hand, indicates that after two days more cells are alive in the sample that was irradiated for one hour compared to the control sample. Subsequently, the graph in Figure 4.2c also shows that there are more cells alive in the sample that was irradiated for one hour compared to the sample that was irradiated for thirty minutes (except on day 0, 6 and 7).

Nonetheless, a clear impact of the alpha particles can be observed on day 0 as can be seen in Figure 4.3.

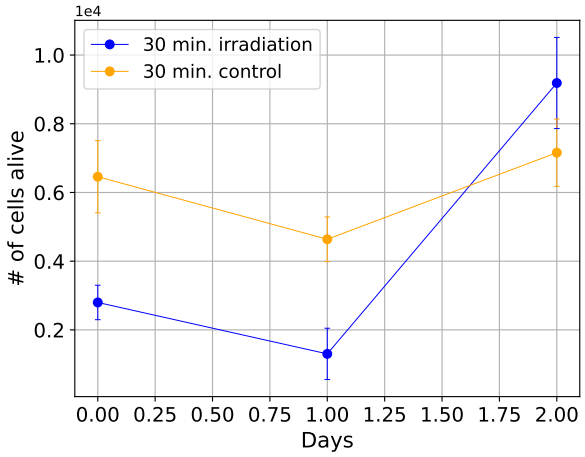

(a)

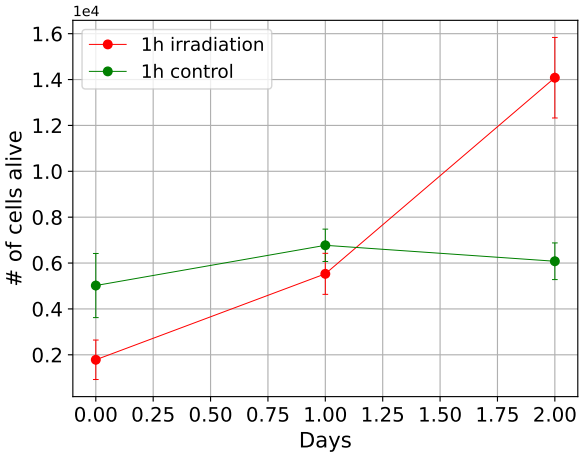

(b)

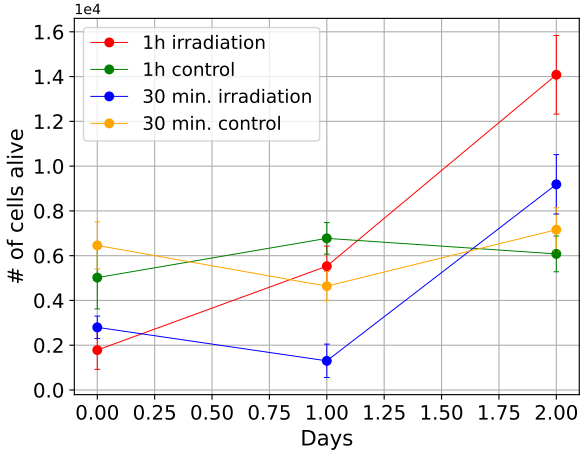

(c)

Figure 4.3: *The results of the first irradiation experiment with the modified protocol, but only the first three data points are shown here. The graph in (a) shows the sample that was irradiated for thirty minutes together with the corresponding control sample. The graph in (b) shows the sample that was irradiated for one hour together with the corresponding control sample. The graph in (c) shows the result of all four samples combined.*

A difference of 64(17)% in number of cells alive between the one-hour control and one-hour irradiated sample, and a difference of 57(7)% between the thirty-minute control and thirty-minute irradiated sample can be observed on day 0. This is a much higher difference compared to the number of cells alive in the measurement of which the results are shown in Figure 1.18: In this first irradiation experiment, only a difference of 24(7)% was observed on day 0 between the sample that was irradiated for thirty minutes and the corresponding control sample. Moreover, in Figure 4.3c, even the sequence between the four data points is in accordance with expectations on day 0: Both control samples indicate the highest number of cells alive and more or less a similar value can be seen here. The lowest number of cells alive can be seen in the sample that was irradiated for one hour. The modifications made to the protocol and the Teflon holders as discussed in the

previous two chapters thus seem to have improved the direct impact of the alpha particles on the cells. However, the data points in the subsequent days following the irradiation experiment are not in accordance with expectations.

On day 1, part of the Resazurin had leaked out of the control sample due to the O-ring that was not perfectly centered around the well. This issue could be solved in future measurements by making a small groove around the well in the larger part of the Teflon holder to make sure the O-ring remains in its place. With a groove, the risk of the O-ring sliding over the gel would also be reduced to a minimum. Nonetheless, even though this could have impacted the results in Figure 4.2a, it does not explain the results shown in Figure 4.2b: In the first four days, barely any increase in the number of cells alive can be observed in the control sample. This could be due to stress induced to the cells, because after these four days an increase in number of cells alive can be seen. Nonetheless, the cause for the stress induced to the cells was not known.

However, a more plausible hypothesis in order to provide an explanation for the results shown in Figure 4.3 is that small gel fragments could be observed floating in the Resazurin when performing the Resazurin assays. The repeated addition and removal of Resazurin and nutrient medium on top of the gel in the days following irradiation is thought to cause gel fragments, in which cells are embedded, to break off. Consequently, with each new Resazurin assay, the gel fragments floating in the liquid are removed, together with the remaining Resazurin, meaning the cells inside these gel fragments are removed as well. Gel fragments could be observed floating in both the irradiated and control samples meaning this could provide an explanation for the poor behaviour of the data obtained from all samples. Moreover, this hypothesis is also strengthened by the second cell-irradiation experiment of which the results are shown in Figure 4.4.

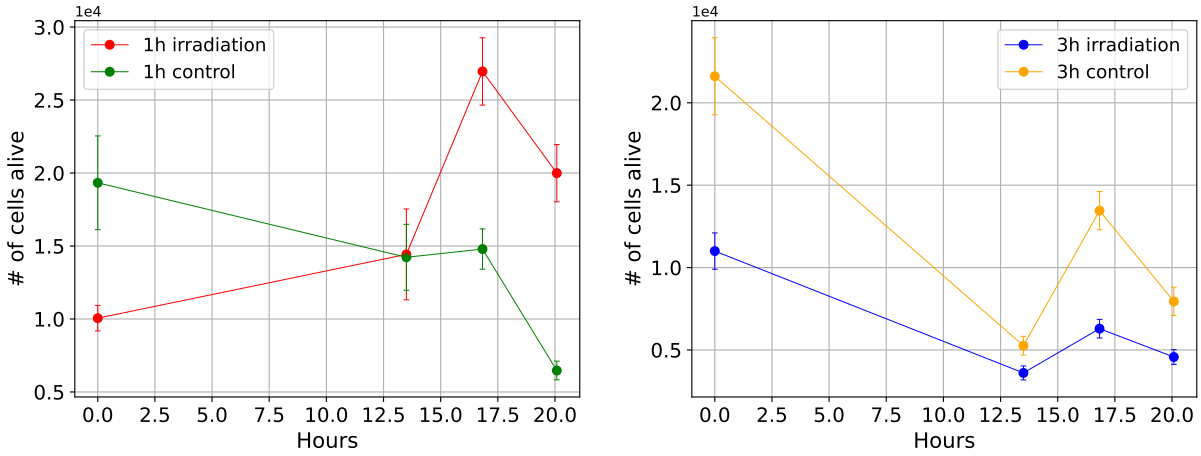

(a) **(b)**

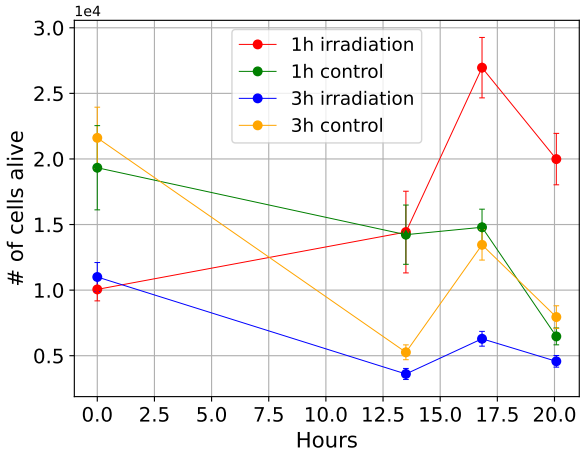

(c)

Figure 4.4: *The results of the second irradiation experiment with the modified protocol. Only the first day after irradiation was probed in this measurement. The graph in (a) shows the sample that was irradiated for one hour together with the corresponding control sample. The graph in (b) shows the sample that was irradiated for three hours together with the corresponding control sample. The graph in (c) shows the result of all four samples combined.*

Four identical samples were prepared as described in section 4.1. However, instead of irradiating them for one hour and thirty minutes, one sample was irradiated for three hours and the second one for one hour. Moreover, only the first day after irradiation was thoroughly probed by performing multiple Resazurin assays in a single day.

In a similar way compared to the results shown in Figure 4.3, a clear impact of the alpha particles can again be observed right after irradiation, indicating the modifications made to the cell-irradiation protocol does seem to have resulted in an improvement on day 0: A difference of 49(4)% in number of cells alive between the three-hour irradiated and three-hour control sample, and a 48(7)% difference in the one-hour irradiated sample compared to the one-hour control sample can be observed. The impact of the alpha particles is thus again almost double compared to the direct impact on the cells on day 0 in the first irradiation experiment of which the results are shown in Figure 1.18. However, the results of subsequent Resazurin assays are not in accordance with expectations: The data points obtained after the third Resazurin assay indicate a higher number of cells alive in the one-hour irradiated sample compared to the corresponding control sample. Moreover, the alternating decreasing and increasing behaviour of the data after the first Resazurin assay is also not in accordance with expectations.

Because the first day after irradiation was thoroughly probed with multiple Resazurin assays, the assays were performed back to back. Hence, once a Resazurin assay was finished, the Resazurin was removed from each holder and each gel was subsequently gently washed by pipetting PBS on top of it and removing it afterwards. This was done three times to make sure all Resazurin of the previous assay was removed before new Resazurin for the next assay was added. This means that for each of the subsequent data points obtained after the first Resazurin assay, the liquid on top of the gel was removed three times as often compared to the previous irradiation measurement. As a result, larger gel fragments could be observed floating in the Resazurin while performing the assays.

Hence, in combination with the poorer results in the subsequent days following irradiation compared to the results in Figure 4.2, this strengthens the suspicion that the poor results obtained after the first Resazurin assay in both measurements discussed in this section are a result of gel fragments breaking off from the the gel due to the repeated addition and removal of Resazurin and nutrient medium on top of the gel. The addition of a layer of agarose gel, on top of the gel in which the cells are embedded, could prevent gel fragments from coming loose while performing the Resazurin assays. This will be discussed in more detail in the next section.

4.3 An Additional Layer of Agarose Gel

Agarose is a polysaccharide which consists of repeating 3-linked-D-galactopyranose and 1,4-linked 3,6-anhydro-α-L-galactopyranose units. The main advantage of this hydrogel is that agarose is a stiff gel, which should prevent gel fragments from breaking off while performing the Resazurin assays. Yet it is very porous meaning that all nutrients in the nutrient medium and the Resazurin are still able to reach the cells underneath the agarose layer. More specific, in this project, a 1 wt% agarose solution was prepared together with PBS which results in a gel with a linear storage modulus near 50 kPa[2] and a pore size near 390 nm [74, 75].

Two agarose layers were prepared in this project: For the first layer, 100 μL was added on top of a gel while for the second layer 200 μL was added on top of a different gel in a second sample. Consequently, this resulted in an agarose layer with a thickness approximately equal to respectively 0.3 mm and 0.6 mm. Both agarose layers are shown in Figure 4.5.

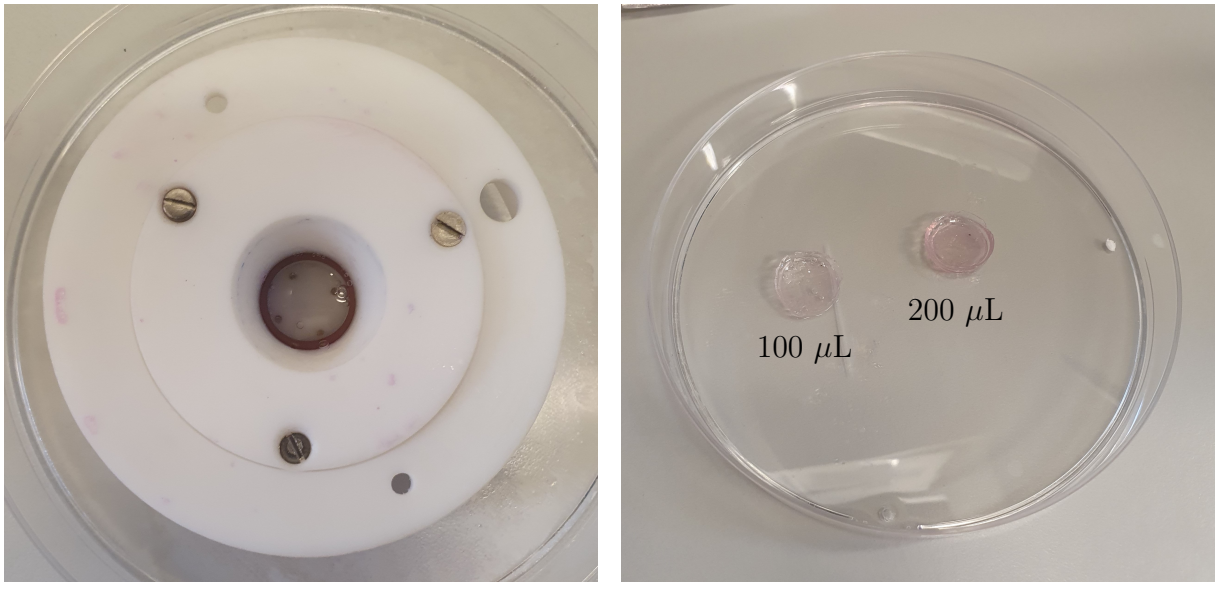

(a) **(b)**

Figure 4.5: *The results of the two agarose layers that were prepared in this project. In (a), the second agarose layer (i.e., when 200 μL was added) in a Teflon holder is shown. In (b), both agarose layers are shown after they were removed from the holders.*

[2]This value was not measured by Lens Dedroog, but obtained from literature [74].

Based upon the results shown in Figure 4.5, the addition of 100 μL on top of the gel in which the cells are embedded seems sufficient, due to the fact that 100 μL of agarose is sufficient to cover the entire gel surface. However, within the limited time scope of this thesis, it was not possible to experimentally verify with a new irradiation experiment the effectiveness of the additional agarose layer.

In conclusion, the modifications made to the protocol and the Teflon holders, as discussed in the previous two chapters, does seem to have improved the direct impact of the alpha particles on the cells: A clear difference between the control samples and the irradiated samples can be observed on day 0 in Figure 4.3 and Figure 4.4. However, measuring the impact of the alpha particles in the subsequent days following irradiation still proves to be challenging due to gel fragments breaking off when performing the Resazurin assays. Nonetheless, the addition of 100 μL agarose on top of the gel after irradiation could provide a solution for this issue. However, the effectiveness of the additional agarose layer should be probed in future irradiation measurements.

Part II

Production of Isotopes for Cell Irradiation

"The only time I set the bar low is for limbo."
Michael Scott – The Office

5 The Recoil-Implantation Generator

The main focus of this thesis thus far has been on the development of a cell-irradiation protocol. This chapter, on the other hand, is devoted to a generator that can be used for the production of isotopes for cell-irradiation experiments by implanting daughter nuclei emitted in alpha decay. The long-term goal of this generator is to produce the bismuth isotope ^{213}Bi and the radium isotope ^{223}Ra due to their promising results for cancer treatment in preclinical and clinical trials.

First, in section 5.1, a brief summary will be given on some basic concepts in nuclear physics that will be utilized in the remainder of this chapter. Then, in section 5.2, the working mechanism of the recoil-implantation generator will be explained in more detail. Subsequently, after providing more details on the experimental setup in section 5.3 to implant the emitted daughter nuclei, the results obtained with this setup will be shown and discussed in section 5.4. That way, in section 5.5, an efficiency for the recoiling process can be deduced from the obtained data. Lastly, in section 5.6, an optimal implantation time will be provided for the production of a ^{213}Bi source utilizing this approach.

5.1 Some Basic Concepts in Nuclear Physics

The activity A of a radioactive sample is a measure of the number of decays per unit time and is typically expressed in Becquerel (Bq) where 1 Bq = 1 decay/s. Mathematically, the activity can be expressed as

$$A = \left| \frac{dN}{dt} \right|, \tag{5.1}$$

where $N = N(t)$ is the number of nuclei present at time t. It can be shown[1] that

$$N(t) = N_0 \cdot e^{-\lambda t}, \tag{5.2}$$

where $N_0 = N(t = 0)$ is the initial amount of nuclei and λ the decay constant (i.e., the probability per unit time that a nucleus will decay). Hence, the activity can be written

[1] See for example [76].

as

$$\begin{aligned} A(t) &= \lambda N_0 \cdot e^{-\lambda t} \\ &= A_0 \cdot e^{-\lambda t}. \end{aligned} \tag{5.3}$$

Here the initial activity A_0 is defined such that $A_0 = A(t = 0) = \lambda N_0$.

Lastly, the half-life ($t_{1/2}$) is defined as the time at which half of the initial nuclei have decayed, meaning that

$$N(t = t_{1/2}) = \frac{N_0}{2}. \tag{5.4}$$

By combining this expression with Equation 5.2, the relation

$$\lambda = \frac{\ln(2)}{t_{1/2}} \tag{5.5}$$

can be obtained.

5.2 Basic Principle of the Generator

The basic principle behind the recoil-implantation generator is shown in Figure 5.1.

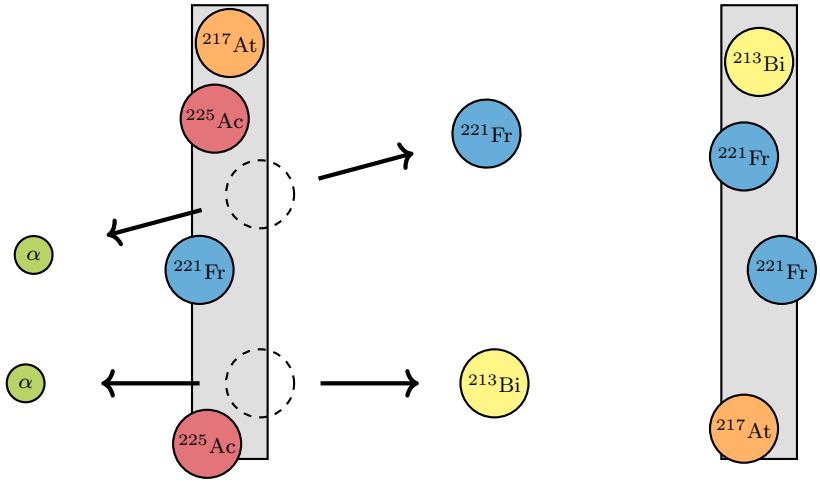

Figure 5.1: *Illustration of the basic principle behind the recoil-implantation generator. An ^{225}Ac implanted source foil (left) is placed in front of an initially empty aluminium disk (right). The implanted ^{225}Ac and daughter nuclei on the source foil will decay and if the recoiling daughters have enough energy, they may leave the source foil and fly towards the aluminium disk.*

The idea behind the recoil-implantation generator is to start from an empty aluminium disk and place it in front of an aluminium source foil on which ^{225}Ac is implanted. The ^{225}Ac will decay and emit an alpha particle in the process. However, due to the law of conservation of momentum, the daughter nucleus will recoil. If the recoiling daughter has enough energy, it may leave the sample and fly towards the aluminium disk in front of the foil. The idea behind the recoil-implantation generator is then to implant this recoiling daughter nucleus on the disk. The collected ^{221}Fr daughter nuclei on the disk will decay to ^{217}At and ^{217}At will decay towards ^{213}Bi that can be used for cell-irradiation experiments.

However, not every ^{225}Ac decay results in a daughter nucleus recoiling from the source foil. Consequently, ^{221}Fr and ^{217}At daughter nuclei will also be present on the source foil resulting in the implantation of ^{217}At and ^{213}Bi directly on the disk as well.

In a similar way, an aluminium source foil implanted with ^{227}Ac can be used as recoil-implantation generator as well: The recoiling daughter nuclei of ^{227}Ac can be caught on an empty aluminium disk and will on their turn decay such that eventually the radium isotope ^{223}Ra is obtained that can be used for cell-irradiation experiments. For further reference on the ^{225}Ac and ^{227}Ac decay chains, see Appendix C.

The goal of the two experiments that were performed in this project, regarding the recoil-implantation generator, is twofold: (1) To see whether it is possible to build a recoil-implantation generator and implant the recoiling ^{225}Ac daughters on an empty aluminium disk and (2) to see whether an efficiency for the recoiling process can be deduced from the obtained data, should it be possible to implant the recoiling daughter nuclei. A formal definition for a recoil efficiency will be provided in section 5.5. First, the experimental setup will be discussed.

5.3 The Experimental Setup

Each of the two performed experiments consisted of two parts. The first part is the implantation part where an empty aluminium disk is placed in front of the ^{225}Ac-implanted foil as illustrated in Figure 5.1. In the second part, the aluminium disk with the recoiled daughters is placed in front of a passivated implanted planar silicon (PIPS) detector[2]. The daughters decay and emit an alpha particle in the process. By measuring the spectrum of the emitted alpha particles, the collected daughters on the aluminium disk can be identified. This second part is illustrated in Figure 5.2.

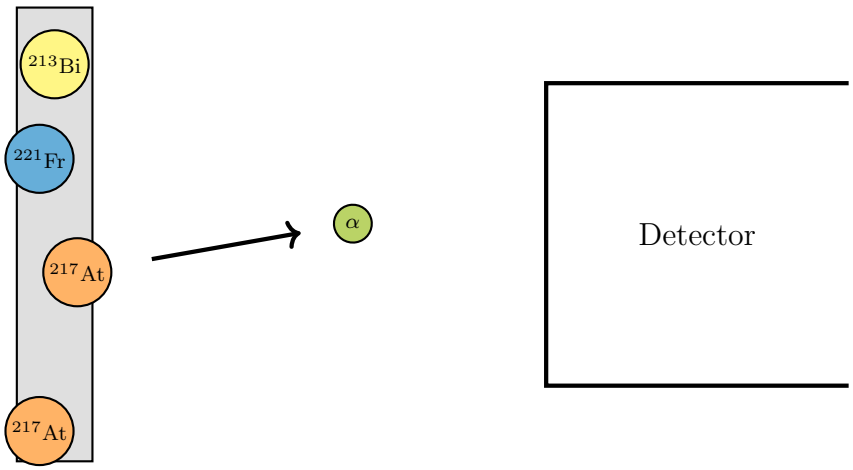

Figure 5.2: *Illustration of the second part of each experiment where the aluminium disk, on which the recoiled daughters are collected, is placed in front of a PIPS detector to measure the spectrum of the emitted alpha particles.*

The required experimental setup, to perform both parts of the measurement, was

[2]Further reference on the detector will be provided in subsection 5.3.2.

built from scratch in collaboration with Max Keppens[3]. A picture of the setup is shown in Figure 5.3.

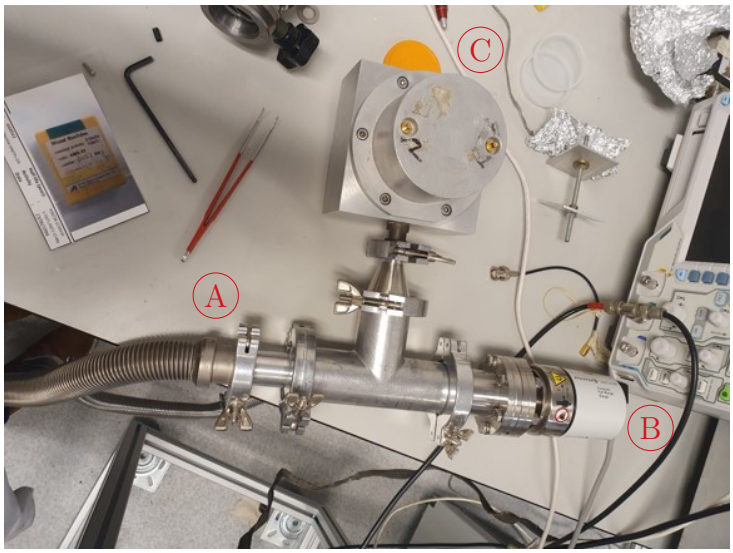

Figure 5.3: *Picture showing the setup of the recoil-implantation generator that was built from scratch in this project. The part indicated with A is the tube connected to the vacuum pump below, B indicates the pressure gauge and the part in C is the vacuum chamber containing the sample and PIPS detector.*

To make sure the recoiling daughters in the first part of the experiment, and the emitted alpha particles in the second part of the experiment, are not hindered by the molecules in the air, both parts were performed in vacuum. Hence, the setup was provided with a vacuum pump (A) and a pressure gauge (B) to make sure the vacuum was maintained during the measurements. For each experiment, a pressure of the order 10^{-3} mbar and 10^{-6} mbar was obtained for respectively the first and second part of the experiment. The part indicated with the letter C in the picture indicates a small chamber, that can be sealed off, in which the second part of both experiments was performed.

5.3.1 The ^{225}Ac-implanted Foil

For both experiments that were performed in this project, the same ^{225}Ac-implanted foil was used. This foil was implanted at CERN-MEDICIS[4] using the isotope separation online (ISOL) method [77]. This technique provides a way to produce, extract and select isotopes allowing the implantation of ^{225}Ac on a foil. However, despite the presence of a mass separator to distinguish between isotopes, some by-products still find their way to the foil as well. For example, besides ^{225}Ac, additional ^{227}Ac will be implanted as well. The presence of ^{227}Ac will become more clear in section 5.4 when the results will be discussed. Further reference on the ISOL method is provided in Appendix D.

[3]Max Keppens is a fellow master student at the IKS whose master's thesis is mainly focused on the production of ^{225}Ac for medical applications.

[4]MEDICIS stands for medical isotopes collected from ISOLDE. Both MEDICIS and ISOLDE are facilities located at CERN.

5.3.2 The Detector

The detector that was used for each of the measurements, was a passivated implanted planar silicon (PIPS) detector which is a silicon semiconductor detector. In a semiconductor, and in solids in general, atoms are embedded in a crystal lattice. Consequently, the electrons of these atoms result in a more collective behaviour compared to electrons in free atoms. Hence, due to the collective behaviour of the electrons, it is more appropriate to describe changes in energy using energy bands[5] instead of discrete energy levels as is the case in free atoms. Two energy bands in particular are of importance in explaining the working principle behind semiconductor detectors: The valence band and the conduction band. The valence band is defined as the highest occupied energy band, while the conduction band is defined as the lowest unoccupied energy band. The conduction band is thus always higher in energy compared to the valence band by definition. In between both energy bands is an energy band gap that determines the electrical conductance of a solid. For example, in an insulator, the band gap is large ($\sim$ 6 eV), meaning the electrons are tightly bound in the valence band and thus the probability that an electron will excite towards the conduction band is rather low. Semiconductors, on the other hand, have a small band gap ($\sim$ 1 eV). The electrons are mainly bound to the valence band, but when sufficient energy is provided, the electrons can be excited from the valence band towards the conduction band. Finally, in metals, the valence and conduction band overlap. As a result, electrons can move freely through the crystal, which explains the excellent conductivity of metals [6, 78]. An overview of the different band gaps is given in Figure 5.4.

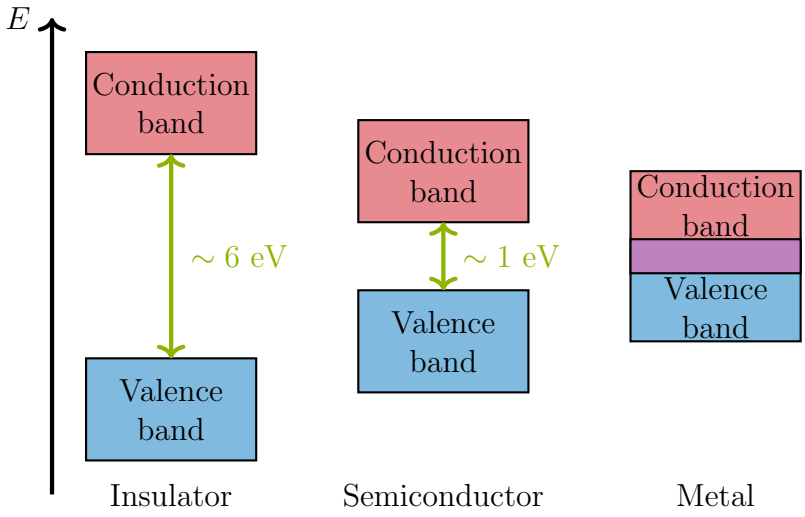

Figure 5.4: *Illustration of the conduction and valence band, together with the associated band gap, for an insulator, a semiconductor and a metal. Illustration is based upon the information retrieved from [6].*

5.3.3 Signal Acquisition

Semiconducting materials are thus excellent for detectors, due to the fact that additional energy is required for an electron to excite towards the conduction band. Hence, when-

[5]Energy bands are composed by degenerate discrete energy levels that are close in energy [6].

ever an alpha particle reaches the detector, it loses its energy inside the semiconducting material providing electrons in the valence band with sufficient energy to excite towards the conduction band. As a consequence of the excitation, a hole is created in the valence band resulting in an electron-hole pair. The higher the energy of the alpha particles, the more energy will be deposited to the medium and thus the more electron-hole pairs will be formed. The energy of the alpha particles is thus proportional to the number of electron-hole pairs formed. However, in order to detect the electron-hole pairs that are formed, a semiconductor detector makes use of a p-n junction on which a reverse bias voltage is applied [6, 78]. An illustration is shown in Figure 5.5.

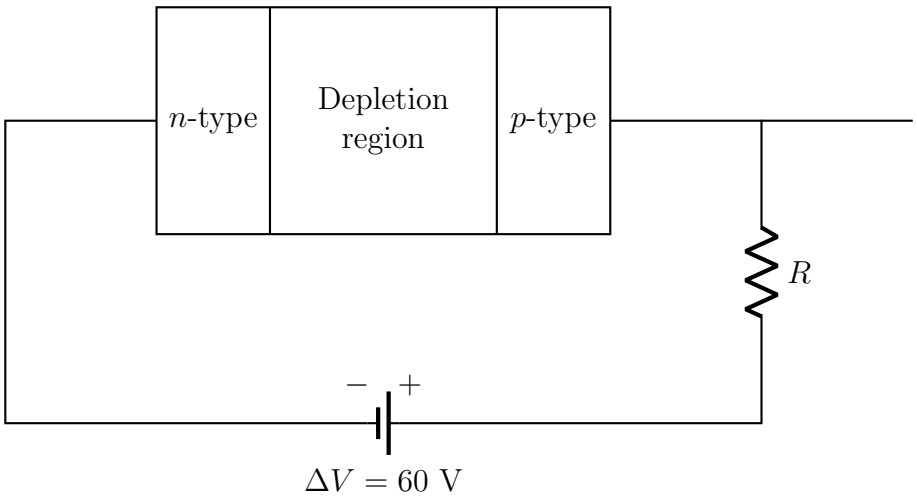

Figure 5.5: *An illustration showing a p-n junction on which a reverse bias voltage of 60 V is applied. The n-type region is a region with an excess of electrons, while the p-type region is a region with an excess of holes. In the depletion region, there are no free charges. Image is based upon the information retrieved from [6].*

A p-n junction consists of three parts: (1) An n-type region, (2) a p-type region and (3) a depletion region. The n-type region is a region with an excess of electrons, while the p-type region is a region with an excess of holes. In the depletion region, there are no free charges, but it is in this region that the alpha particles will deposit their energy such that electron-hole pairs can be formed. Hence, as a consequence of the excess negative charges in the n-type region and the excess holes in the p-type region, combined with the applied reverse bias voltage[6], an electric field will be present causing the electrons to drift towards the p-type region and the holes towards the n-type region. As a result, a current will flow in the circuit that is proportional to the amount of electrons collected in the p-type region and thus proportional to the number of electron-hole pairs formed in the depletion region as well [6, 78]. Moreover, the presence of a reverse bias voltage also results in a larger depletion region compared to a p-n junction without a reverse bias voltage.

[6]In this project, a reverse bias voltage equal to 60 V was applied.

5.3.4 Signal Processing

Once a current flows through the electrical circuit, the first obtained signal is a voltage pulse measured over the resistor R (see Figure 5.5). The height of the voltage pulse, on top of the bias voltage, is of the orders of millivolts and is proportional to the magnitude of the current in the circuit. In the next step, the signal arrives at the preamplifier, which consists of a resistor in parallel with a capacitor. The preamplifier (1) separates the signal from the bias voltage, (2) amplifies the signal and (3) reshapes it towards a decaying exponential shape. The height of the decaying exponential voltage pulse is still proportional to the height of the initial obtained voltage pulse [6, 79].

In a subsequent step, the exponential-shaped signal arrives at the digitizer. The algorithm used in the digitizer is a Digital Pulse Processing for Pulse Height Analysis (DPP-PHA) algorithm that is based upon the Jordanov trapezoidal filter [79]. The DPP-PHA algorithm amplifies the exponentially-shaped voltage pulse and reshapes it in a trapezoid. The height of the trapezoid is of the order of 1 V and is proportional to the height of the voltage pulse leaving the preamplifier. The digitizer also serves as a digital multi-channel analyzer, meaning that to each signal a channel number is assigned based on the height of the voltage pulse. The assigned channel number is proportional to the height of the voltage pulse, meaning the higher the voltage pulse, the higher the channel number will be. That way, a histogram can be constructed where on the vertical axis the number of counts is expressed and on the horizontal axis the channel number [79]. An overview of the different steps in the signal processing is shown in Figure 5.6.

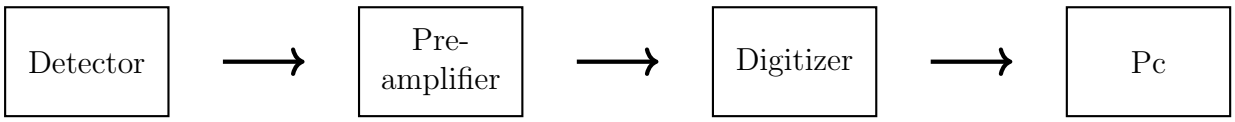

Figure 5.6: *A schematic overview of the signal processing. Information obtained from [79].*

In conclusion, when all the proportionality relations that were discussed in this subsection and the previous subsection are summarized, it is found that

$$\begin{aligned} \text{Energy } \alpha \text{ particle} &\propto \#\text{ Electron-hole pairs} \\ &\propto \text{Current flowing through resistor} \\ &\propto \text{Voltage measured over resistor} \\ &\propto \text{Height voltage pulse after preamplifier} \\ &\propto \text{Height trapezoid} \\ &\propto \text{Channel number} \end{aligned} \tag{5.6}$$

and thus a linear energy calibration is expected. The energy calibration was performed by Max Keppens and he obtained that

$$\text{Energy} = a \cdot \text{Channel number} + b, \tag{5.7}$$

where $a = 1.53718(33)$ keV/channel and $b = 15.710(93)$ keV. This calibration was also used for the results that will be shown in the next section.

5.4 Results

Two measurements were performed in total during this project on which an overview is given in Table 5.1.

Table 5.1: *An overview of the two measurements that were performed. The expected activity of the ^{225}Ac sample is based upon a $967(37) \times 10^2$ Bq activity on 27/05/2023 at 20:38 and was determined using Equation 5.3 in section 5.1. The expected activities given here are from the moment implantation started.*

	Measurement 1	**Measurement 2**
Expected activity ^{225}Ac sample	6.05(23) Bq	0.0899(35) Bq
Implantation time	2 hours	2 days, 23 hours and 38 minutes
Measurement time	5 hours and 42 minutes	3 days, 21 hours and 5 minutes

The results of measurement 1 are shown in Figure 5.7.

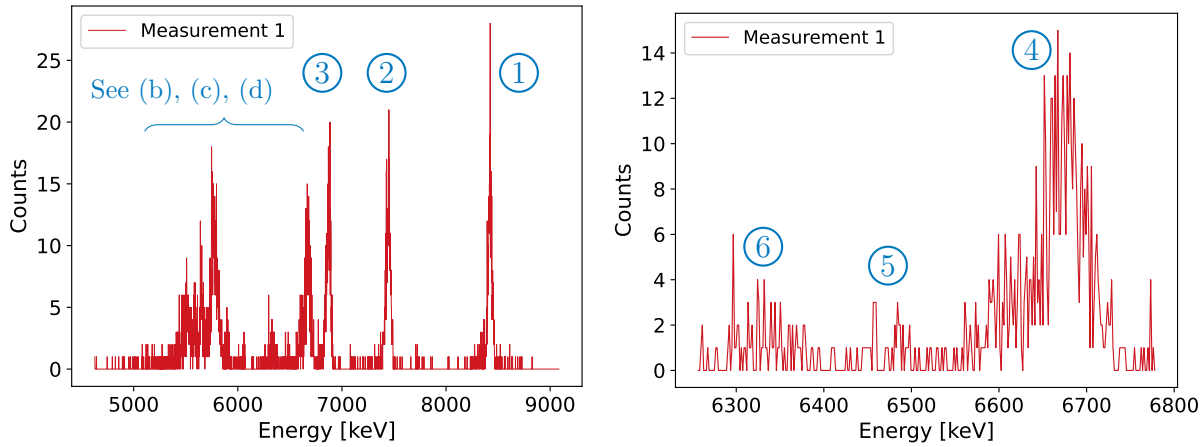

(a) **(b)**

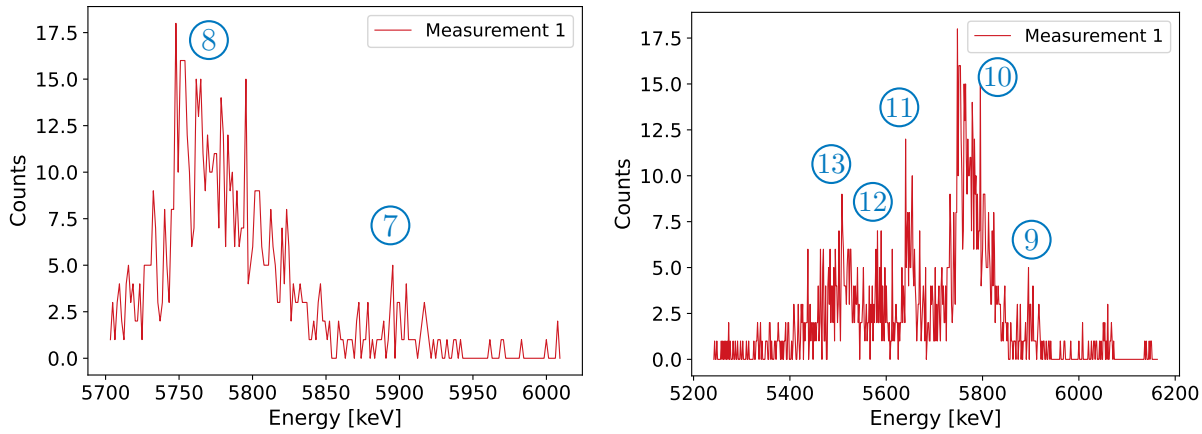

(c) **(d)**

Figure 5.7: *Results of the first measurement. The spectrum in (a) shows an overview of all the peaks that were measured. The spectra in (b), (c) and (d) show a closer view of respectively the energy regions 6300 keV - 6800 keV, 5700 keV - 6000 keV and 5200 keV - 6200 keV. The errorbars were left out to improve readability.*

Even though the activity of the ^{225}Ac sample was low (i.e., 6.05(23) Bq), clear peaks could be distinguished in the obtained spectrum. Each of the peaks was fitted with a Crystal Ball function in order to determine the corresponding energy value. The Crystal Ball function is defined by the function f such that

$$f(x) = \begin{cases} N \cdot \exp\left(\frac{-(x-\mu)^2}{2\sigma^2}\right), & \frac{x-\mu}{\sigma} > -\beta \\ N \cdot A \cdot \left(B - \frac{x-\mu}{\sigma}\right)^{-m}, & \frac{x-\mu}{\sigma} \leq -\beta \end{cases} \tag{5.8}$$

where

- $A = \left(\frac{m}{|\beta|}\right)^m \cdot \exp\left(\frac{-\beta^2}{2}\right)$,
- $B = \frac{m}{|\beta|} - |\beta|$,
- N is a constant.

The Crystal Ball function is a Gaussian function with a power-law tail in the lower energy region [80, 81]. The reason why this function was used to fit the peaks, and not a regular Gaussian, is that alpha particles have a low penetration depth and a high LET. This means they lose large amounts of energy when travelling a short distance, as was discussed in the introduction of this thesis. Consequently, when an alpha particle reaches the detector at an angle, it loses significantly more energy compared to an alpha particle whose trajectory is perpendicular to the detector due to the larger distance covered in the insensitive, top layer of the detector (i.e., the dead layer of the detector) before it is detected. Hence, an extra power-law tail is required to take this energy loss into account.

Thirteen peaks in total could be observed and linked to either the ^{225}Ac decay chain or the ^{227}Ac decay chain. For further reference on the ^{225}Ac and ^{227}Ac decay chain, see Appendix C. An overview of each decay related to each peak is shown in Table 5.2.

Table 5.2: *An overview of the decays related to each peak in the spectrum shown in Figure 5.7. The decays indicated in red are due to the ^{225}Ac decay chain, while the decays written in blue are due to the ^{227}Ac decay chain.*

Peak number	Most probably due to	Other possibilities
1	^{213}Po $\longrightarrow$ ^{209}Pb + ^{4}He	/
2	^{215}Po $\longrightarrow$ ^{211}Pb + ^{4}He	^{211}Po $\longrightarrow$ ^{207}Pb + ^{4}He
3	^{219}Rn $\longrightarrow$ ^{215}Po + ^{4}He	/
4	^{211}Bi $\longrightarrow$ ^{207}Tl + ^{4}He	/
5	^{219}Rn $\longrightarrow$ ^{215}Po + ^{4}He	/
6	^{221}Fr $\longrightarrow$ ^{217}At + ^{4}He	/
7	^{213}Bi $\longrightarrow$ ^{209}Tl + ^{4}He	/
8	^{227}Th $\longrightarrow$ ^{223}Rn + ^{4}He ^{223}Ra $\longrightarrow$ ^{219}Rn + ^{4}He	/
9	^{213}Bi $\longrightarrow$ ^{209}Tl + ^{4}He	/
10	^{227}Th $\longrightarrow$ ^{223}Rn + ^{4}He ^{223}Ra $\longrightarrow$ ^{219}Rn + ^{4}He	/
11	^{223}Ra $\longrightarrow$ ^{219}Rn + ^{4}He	^{227}Th $\longrightarrow$ ^{223}Ra + ^{4}He
12	^{223}Ra $\longrightarrow$ ^{219}Rn + ^{4}He	^{213}Bi $\longrightarrow$ ^{209}Tl + ^{4}He
13	^{223}Ra $\longrightarrow$ ^{219}Rn + ^{4}He	^{213}Bi $\longrightarrow$ ^{209}Tl + ^{4}He

The decays related to each peak were based on the energy of the peak that was obtained after fitting, the energy of the emitted alpha particles retrieved from [82] and the branching ratios of each decay. However, it is unclear whether the peaks labeled with number 12 and 13 are due to the ^{225}Ac decay chain or the ^{227}Ac decay chain. The branching ratio seems to suggest it is due to the ^{227}Ac decay chain, but to be sure, a second measurement was performed using the same ^{225}Ac implanted foil. As indicated in Table 5.1, an activity equal to 0.0899(35) Bq due to the ^{225}Ac present is expected. This means that in the second measurement, mainly the recoiling daughters from the ^{227}Ac decay chain will be implanted on the empty aluminium disk due to the longer half-life of ^{227}Ac. The result of the second measurement is shown in Figure 5.8.

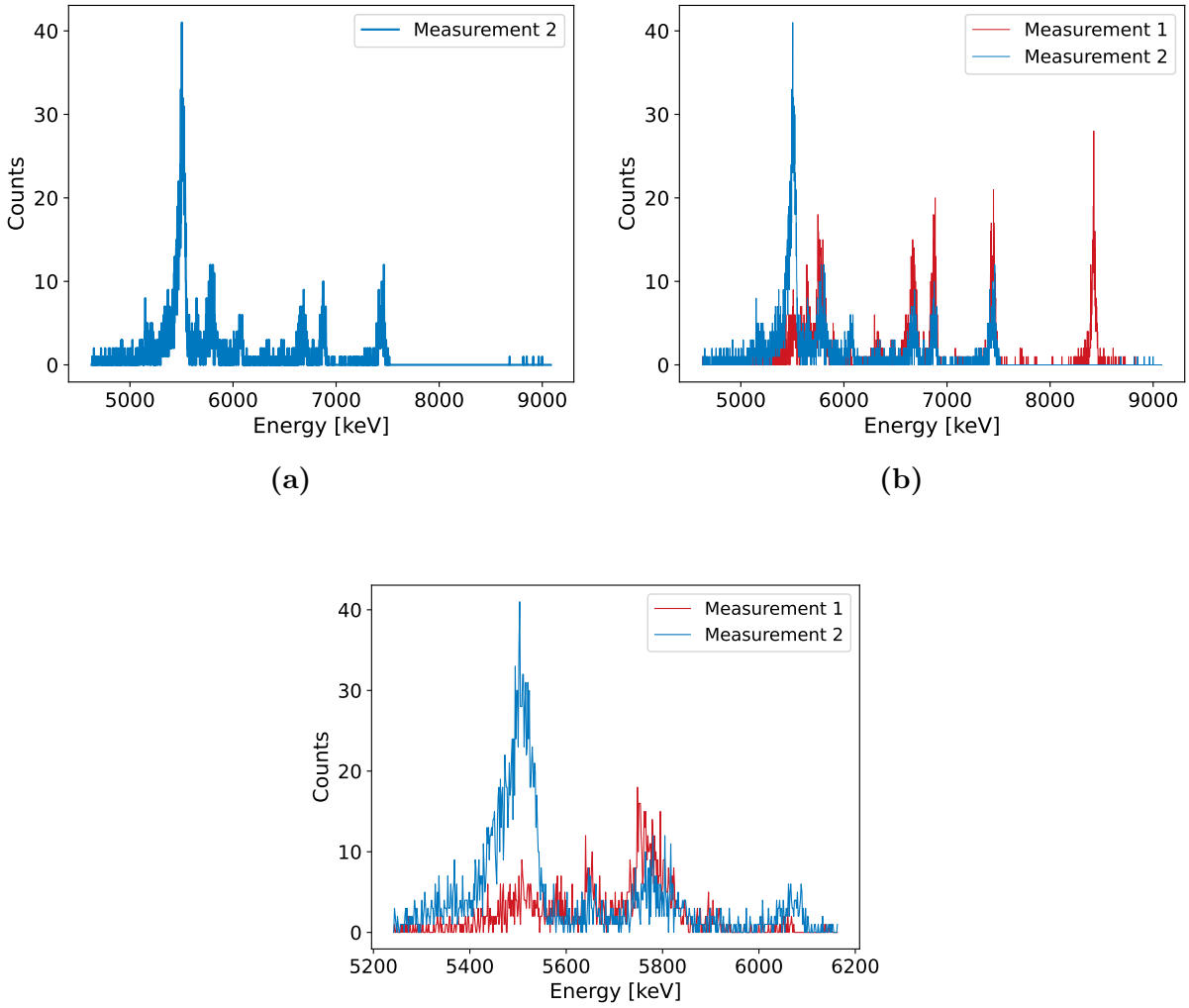

Figure 5.8: *The results of the second measurement. The graph in (a) shows the obtained spectrum in the second measurement and the graph in (b) shows both spectra from the first and second measurement combined. The graph in (c) shows the same spectrum as the one in (b), but for the energy region between 5200 keV - 6200 keV.*

As expected, barely any alpha particles emitted in the ^{225}Ac decay chain were detected. For example, in Figure 5.8b, a clear peak due to the decay $^{213}\text{Po} \longrightarrow {}^{209}\text{Pb} + {}^{4}\text{He}$ can be distinguished in the spectrum obtained in the first measurement (i.e., peak 1), but cannot be observed in the spectrum in the second measurement. The two peaks labeled in Figure 5.7 with number 12 and 13 could not be assigned with certainty to the ^{225}Ac or the ^{227}Ac decay chain. However, in Figure 5.8c, a clear blue peak can be observed now in the second measurement, meaning that both peaks are indeed due to the ^{227}Ac decay chain.

In conclusion, the first goal stated in the introduction of this chapter was to see whether it was possible to build a recoil-implantation generator and implant the recoiling daughter nuclei on an empty aluminium disk. The results given and discussed in this section show that this is indeed possible and thus indicating the potential of the recoil-implantation generator for the production of ^{213}Bi and ^{223}Ra for cell-irradiation experiments in the

future. In the next section, the efficiency of the recoiling process will be discussed in more detail.

5.5 The Recoil Efficiency

In order to quantify the efficiency of the recoiling process, the recoil efficiency ϵ_{Recoil} will be defined as

$$\epsilon_{\text{Recoil}} = \frac{A_{0,\text{Disk}}^{(\text{Bi-213})}}{A_{0,\text{Foil}}^{(\text{Ac-225})}}, \tag{5.9}$$

where $A_{0,\text{Disk}}^{(\text{Bi-213})}$ and $A_{0,\text{Foil}}^{(\text{Ac-225})}$ are the activities after implantation of respectively the ^{213}Bi on the aluminium disk and the ^{225}Ac on the foil. The remainder of this section will be dedicated to the derivation of a formula that can be used to determine the value of ϵ_{Recoil} based on the results shown in section 5.4. First, an expression for $A_{0,\text{Disk}}^{(\text{Bi-213})}$ will be derived. However, in this derivation, the assumption will be made that only the daughter nuclei in the decay $^{225}\text{Ac} \longrightarrow {}^{221}\text{Fr} + {}^{4}\text{He}$ are implanted on the aluminium disk during the first part of the experiment.

The activity is a measure of the amount of decays per unit time. Hence, if the measurement started at $t = 0$ and stopped at $t = t_m$, the total amount of ^{213}Bi isotopes, $N_{0\to t_m}^{(\text{Bi-213})}$, that decayed during the measurement can be determined as

$$N_{0\to t_m}^{(\text{Bi-213})} = \int_0^{t_m} A_{\text{Disk}}^{(\text{Bi-213})}(t)dt, \tag{5.10}$$

where $A_{\text{Disk}}^{(\text{Bi-213})}(t)$ is the activity on the disk at time t due to the ^{213}Bi present. Using Equation 5.3, this expression can be rewritten such that

$$\begin{aligned}\int_0^{t_m} A_{\text{Disk}}^{(\text{Bi-213})}(t)dt &= \int_0^{t_m} A_{0,\text{Disk}}^{(\text{Bi-213})} \cdot e^{-\lambda_{\text{Bi-213}}t}dt \\ &= \frac{A_{0,\text{Disk}}^{(\text{Bi-213})}}{\lambda_{\text{Bi-213}}} \cdot \left(1 - e^{-\lambda_{\text{Bi-213}}t_m}\right)\end{aligned} \tag{5.11}$$

is obtained due to the fact that $A_{0,\text{Disk}}^{(\text{Bi-213})}$ is a constant value and thus can be taken out of the integral. On the other hand, the total amount of ^{213}Bi isotopes that have decayed during the measurement can be deduced from the data in section 5.4 as well: Whenever a ^{213}Bi isotope decays, an electron and electron antineutrino are emitted in the process such that a ^{213}Po daughter remains (see Appendix C). However, due to the short ^{213}Po half-life of 3.7 μs, an alpha particle is emitted almost instantly that can be measured. Hence, by counting the total number of alpha particles emitted in the decay of ^{213}Po, the total number of ^{213}Bi isotopes that have decayed during the measurement can be deduced. Let $A_{\text{Disk}}^{(\text{Po-213})}$ be the activity due to the ^{213}Po present on the disk. Then

$$\begin{aligned}A_{\text{Disk}}^{(\text{Po-213})}(t) &= b_{\beta^-} \cdot A_{\text{Disk}}^{(\text{Bi-213})}(t) \\ C_{\alpha}^{(\text{Po-213})}(t) &= b_{\beta^-} \cdot \epsilon_{\text{Geo}} \cdot A_{\text{Disk}}^{(\text{Bi-213})}(t)\end{aligned} \tag{5.12}$$

where b_{β^-} is the branching ratio in the decay chain towards ^{213}Po (i.e., 97.9%, see Appendix C), ϵ_{Geo} the geometric efficiency to take the solid angle into account and $C_{\alpha}^{(\text{Po-213})}$

is the detected number of alpha particles per unit time due to the decay of ^{213}Po. Hence, in combination with Equation 5.10, it is found that

$$\begin{aligned} N_{0\rightarrow t_m}^{(\text{Bi-213})} &= \int_0^{t_m} \frac{C_\alpha^{(\text{Po-213})}(t)}{b_{\beta^-} \cdot \epsilon_{\text{Geo}}} dt \\ &= \frac{1}{b_{\beta^-} \cdot \epsilon_{\text{Geo}}} \cdot \int_0^{t_m} C_\alpha^{(\text{Po-213})}(t) dt, \end{aligned} \tag{5.13}$$

due to the fact that b_{β^-} and ϵ_{Geo} are constant values and thus can be taken out of the integral. The integral obtained in the final line is equal to $N_{0\rightarrow t_m}^{(\text{Po-213})}$, the total number of alpha particles detected due to the decay of ^{213}Po. This value can be obtained from the data shown in Figure 5.7 by summing all measured counts in the peak labeled with number 1.

Finally, by combining Equation 5.10, Equation 5.11 and Equation 5.13, the value of $A_{0,\text{Disk}}^{(\text{Bi-213})}$ can be determined as

$$\begin{aligned} \frac{A_{0,\text{Disk}}^{(\text{Bi-213})}}{\lambda_{\text{Bi-213}}} \cdot \left(1 - e^{-\lambda_{\text{Bi-213}} t_m}\right) &= \frac{N_{0\rightarrow t_m}^{(\text{Po-213})}}{b_{\beta^-} \cdot \epsilon_{\text{Geo}}} \\ A_{0,\text{Disk}}^{(\text{Bi-213})} &= \frac{N_{0\rightarrow t_m}^{(\text{Po-213})} \cdot \lambda_{\text{Bi-213}}}{b_{\beta^-} \cdot \epsilon_{\text{Geo}} \cdot \left(1 - e^{-\lambda_{\text{Bi-213}} t_m}\right)}. \end{aligned} \tag{5.14}$$

The value of $A_{0,\text{Foil}}^{(\text{Ac-225})}$, on the other hand, can be deduced from the initial activity when the foil was implanted at MEDICIS. On 27/05/2023 at 20:38, the activity of the foil was found to be equal to $967(37) \times 10^2$ Bq, as was stated earlier in Table 5.1. The measurement discussed in section 5.4 started on 13/10/2023 at 11:41. Hence, using Equation 5.3, the value of $A_{0,\text{Foil}}^{(\text{Ac-225})}$ was found to be equal to 6.01(23) Bq.

By combining the above-mentioned results, the recoil efficiency can be determined as

$$\epsilon_{\text{Recoil}} = \frac{N_{0\rightarrow t_m}^{(\text{Po-213})} \cdot \lambda_{\text{Bi-213}}}{b_{\beta^-} \cdot \epsilon_{\text{Geo}} \cdot A_{0,\text{Foil}}^{(\text{Ac-225})} \cdot \left(1 - e^{-\lambda_{\text{Bi-213}} t_m}\right)}, \tag{5.15}$$

where

- $N_{0\rightarrow t_m}^{(\text{Po-213})} = 478(22)$. The uncertainty associated with this value is the statistical Poisson uncertainty.
- $\lambda_{\text{Bi-213}} = \frac{\ln(2)}{t_{1/2}^{(\text{Bi-213})}}$. Here is $t_{1/2}^{(\text{Bi-213})}$ the half-life of ^{213}Bi which is equal to 45.610(60) minutes [83].
- $b_{\beta^-} = 0.979$, due to a branching ratio of 97.9% [82].
- $A_{0,\text{Foil}}^{(\text{Ac-225})} = 6.01(23)$ Bq.
- $t_m = 342(1)$ minutes, due to the fact that the measurement lasted for five hours and forty-two minutes.

The value of the geometric efficiency ϵ_{Geo} was determined using a Monte-Carlo based code provided by Michael Heines from the IKS. A Gaussian source (i.e., the disk on which the recoiled daughters are collected) and a circular target (i.e., the PIPS detector) with a radius equal to 9.98(50) mm were assumed here. The distance between the disk and the detector was equal to 9.18(50) mm. One of the input parameters the code required, was the standard deviation of the Gaussian distribution of the source. However, this value was not known. Hence, the choice was made to determine the value of the geometric efficiency ϵ_{Geo} for three different standard deviations:

- In the first calculation, one standard deviation of the Gaussian distribution corresponded to the radius of the collimator in front of the implanted disk,
- In the second calculation, two standard deviations of the Gaussian distribution corresponded to the radius of the collimator in front of the implanted disk,
- In the third calculation, three standard deviations of the Gaussian distribution corresponded to the radius of the collimator in front of the implanted disk.

As a result, three value for ϵ_{Geo} were obtained such that subsequently three values for ϵ_{Recoil} could be determined using Equation 5.15. An overview of the obtained values for both ϵ_{Geo} and ϵ_{Recoil} is provided in Table 5.3.

Table 5.3: *An overview of the three values for the geometric efficiency (ϵ_{Geo}) obtained by utilizing Michael Heines' code together with the corresponding recoil efficiency (ϵ_{Recoil}) obtained from Equation 5.15. In calculation one, two and three the radius of the collimator in front of the implanted disk corresponded to respectively one, two and three standard deviations of the Gaussian distribution.*

Calculation	ϵ_{Geo}	ϵ_{Recoil}
1	0.114(21)	0.182(40)
2	0.144(27)	0.143(28)
3	0.1536(180)	0.135(26)

Finally, with the three values for ϵ_{Recoil} shown in Table 5.3, a weighted mean was calculated together with the associated uncertainty[7] and it was found that $\epsilon_{\text{Recoil}} = 0.1467(171)$. However, the real value of the recoil efficiency, is in practice lower compared to this value. The reason for this is that in the calculation of ϵ_{Recoil} the assumption was made that only the recoiling ^{221}Fr daughters in the decay $^{225}\text{Ac} \longrightarrow {}^{221}\text{Fr} + {}^{4}\text{He}$ are collected on the disk. However, in the implantation part of the experiment, not only the ^{221}Fr daughters of ^{225}Ac are collected on the disk but the ^{217}At daughter of ^{221}Fr and ^{213}Bi daughter of ^{217}At are collected on the disk as well. Consequently, these daughter nuclei contribute to the value of $N_{0\rightarrow t_m}^{(\text{Po-213})}$ as well. Nonetheless, the activity of sources produced at MEDICIS, such as for example the implanted ^{225}Ac foil utilized in this project, is typically near 100 kBq. Hence, upon combining the definition of the recoil efficiency in Equation 5.9 together with the obtained value for ϵ_{Recoil}, the activity of the implanted disk due to the ^{213}Bi present is expected to be near $0.1467(171) \cdot 100$ kBq $= 14.67(171)$ kBq.

[7] Further reference on the weighted mean and the associated uncertainty is given in Appendix E.

5.6 Estimating an Optimal Implantation Time

The activity of the ^{241}Am source utilized for the cell-irradiation experiments is estimated to be near 8 kBq (see section 1.5). Hence, with a new ^{225}Ac implanted foil produced at MEDICIS with an activity near 100 kBq, a ^{213}Bi source with almost double the activity compared to the ^{241}Am source is expected. However, due to the short half-life of ^{213}Bi (i.e., 45.610(60) minutes) compared to the long ^{241}Am half-life (i.e., 432.60(60) years), the gels will not uniformly be irradiated anymore when performing one-hour or three-hour irradiation experiments [83]. Moreover, each time an irradiation experiment is performed, the ^{213}Bi should be implanted anew. By utilizing the Bateman equations, an estimate for the optimal implantation time can be determined.

Assume there are n isotopes such that isotope 1 decays to isotope 2, isotope 2 decays to isotope 3, ..., isotope $n-1$ decays to isotope n. The Bateman equations state that

$$\begin{aligned} \frac{dN_1}{dt} &= -\lambda_1 N_1 \\ \frac{dN_i}{dt} &= \lambda_{i-1} N_{i-1} - \lambda_i N_i, \qquad \text{for } i = 2, ..., n \end{aligned} \tag{5.16}$$

where $N_i = N_i(t)$ and λ_i are respectively the amount of nuclei present at time t and the decay constant of isotope i [84]. If $N_1(t=0) \neq 0$ and $N_i(t=0) = 0$, for $i = 2, ..., n$, it can be shown[8] that

$$N_n(t) = \frac{N_1(t=0)}{\lambda_n} \sum_{i=1}^{n} \lambda_i \alpha_i \exp\big(-\lambda_i t\big) \tag{5.17}$$

where

$$\alpha_i = \prod_{\substack{j=1 \\ j \neq i}}^{n} \frac{\lambda_j}{\lambda_j - \lambda_i}. \tag{5.18}$$

For this project, the amount of ^{213}Bi nuclei present on the aluminium disk while implanting can be estimated using the above equation for $n = 4$ due to the fact that only the first part in the ^{225}Ac decay chain is required: $^{225}\text{Ac} \rightarrow {}^{221}\text{Fr} \rightarrow {}^{217}\text{At} \rightarrow {}^{213}\text{Bi}$ (see Appendix C). Hence, as a result, the amount of ^{213}Bi isotopes present on the disk while implanting as a function of time is shown in Figure 5.9.

[8] See for example [85].

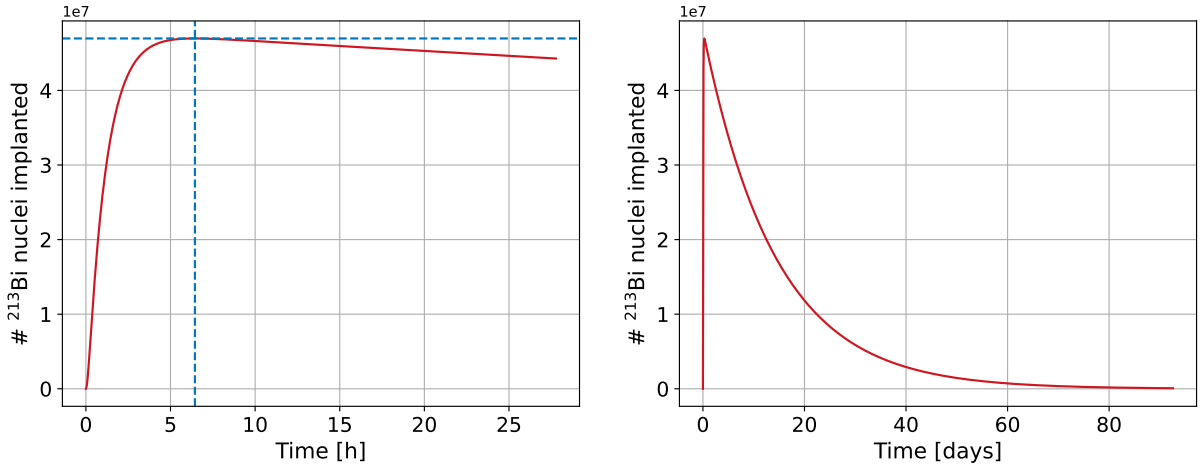

(a) **(b)**

Figure 5.9: *The amount of ^{213}Bi nuclei present on the disk as a function of time while implanting. The graph in (a) shows the region where the function reaches a maximum value. The graph in (b) shows the global behavior of the function. The vertical and horizontal dashed lines indicate the maximum of the function.*

Both graphs show the same quantity but for a different time interval and were drawn by using 100 kBq (i.e., the typical activity of a source foil implanted at MEDICIS) multiplied by the geometric efficiency corresponding to the implantation part of the experiment as initial value for $N_1(t = 0)$. This value for the geometric efficiency was determined in an identical way as discussed in the end of the previous section using Michael Heines' code, except there was one difference here: Now a distance equal to 3.52(50) mm was utilized corresponding to the distance between the implanted ^{225}Ac source foil and the empty aluminium disk. With this approach, the assumption is thus made that only daughter nuclei due to the decay $^{225}\text{Ac} \rightarrow {}^{221}\text{Fr} + {}^{4}\text{He}$ are implanted on the disk, which is the same assumption that was made when deriving an expression for the recoil efficiency. Nonetheless, with these initial parameters, an optimal implantation time equal to six hours, 26 minutes and 40 seconds of implantation was obtained resulting in approximately 4.70×10^7 implanted ^{213}Bi isotopes. The optimal implantation time and the maximum amount of implanted ^{213}Bi isotopes are indicated in Figure 5.9 with respectively the vertical and horizontal dashed blue line. It follows from Equation 5.17 that the optimal implantation time is independent of the initial amount of nuclei, $N_1(t = 0)$. The reason for this is when optimizing $N_n(t)$, the time extracted from the expression

$$\frac{dN_n}{dt} = 0 \tag{5.19}$$

is independent of $N_1(t = 0)$.

When utilizing a ^{213}Bi source produced in this way to perform cell-irradiation experiments, the ^{213}Bi should be implanted anew for each experiment due to its short half-life (i.e., 45.610(60) minutes) [83]. However, from a practical point of view, both the cell-irradiation and the implantation do not necessarily need to take place on the same day: If the ^{213}Bi implantation is started in the evening, the day before an irradiation experiment, the foil can be implanted all night long up until noon when the samples are ready and the

gels can be irradiated. Consequently, this would result in a total implantation time near 18 hours. However, based on the information retrieved from Figure 5.9, the implanted amount of ^{213}Bi isotopes would only result in a 3% difference compared to the implanted amount of ^{213}Bi nuclei indicated with the dashed blue lines in Figure 5.9.

In conclusion, the results shown and discussed in this chapter indicate that it is indeed possible to implant the recoiling ^{225}Ac daughter nuclei on an aluminium disk. Moreover, an efficiency for the recoiling process could be estimated based on the obtained data by deriving an expression for the recoil efficiency ϵ_{Recoil}. This value was found to be equal to 0.1467(171), which could yield a ^{213}Bi source with an activity of 14.67(171) kBq for 100 kBq of ^{225}Ac. By utilizing the recoil-implantation generator, a ^{213}Bi source can thus be produced for future cell-irradiation experiments when a new ^{225}Ac implanted source foil with a higher activity is available. However, the short ^{213}Bi half-life requires that the ^{213}Bi should be implanted anew for each cell-irradiation experiment. Nonetheless, the implantation can start in the evening, the day before an irradiation experiment is planned, as it will only result in a difference of 3% compared to the optimal amount of implanted ^{213}Bi isotopes.

"Don't feel bad about this... Part of the journey is the end."

Tony Stark – Avengers: Endgame

Conclusion

Part I – Development of a Cell-Irradiation Protocol

The goal of the first part of this thesis was the further development of a cell-irradiation protocol to externally irradiate HeLa cells embedded in a hydrogel. This protocol is a first step in a larger experimental endeavor to probe the radiobiological effects of the recoiling ^{225}Ac daughter nuclei.

The first part of this thesis started with a cell-irradiation experiment by following the protocol developed in earlier work (see [2]). This protocol made use of 1.5 mg/mL collagen gels in which the cells were embedded. However, it was noticed in earlier work that these hydrogels were too fragile and too easily damaged by the gel manipulation in the protocol, thus resulting in too much additional damage [2]. Hence, instead of using a 1.5 mg/mL collagen gel, a 2.0 mg/mL collagen was utilized in this project to obtain a stronger and more damage-resistant gel. However, the obtained results were not in accordance with the expectations such that three hypotheses were formulated to provide an explanation for these results.

For the first hypothesis, the cell sedimentation in three materials was investigated using confocal microscopy: Both 1.5 mg/mL and 2.0 mg/mL collagen gels, a 5 wt% PEG gel and a hydrogel containing 50% Matrigel. An excellent cell sedimentation was only observed in the hydrogels containing Matrigel. Matrigel thus proved to be not only a stronger alternative for the 1.5 mg/mL collagen gels, but an improved cell sedimentation was observed as well.

For the second hypothesis, the Matrigel concentration was increased from 50% up to 60% and modifications to the Teflon holders were made such that the protocol could be adjusted to reduce additional damage due to gel manipulations to a minimum: With these changes, the Resazurin assays could be performed inside the Teflon holders such that the gels did not need to be taken out of the holders anymore with a pair of tweezers.

Lastly, for the third hypothesis, the issues regarding gel adhesion to the glass slides upon removing them was investigated using multiphoton microscopy. To prevent gel adhesion to the glass slides, eight potential solutions were probed. Out of these eight potential solutions, both the methacrylate-silane covered glass slides provided with an additional PEGDA coating and the APTES coated glass slide provided with an additional PEG and DTT coating prepared on a piece of Teflon tape seemed to prevent gel adhesion to some extent. However, only the APTES coated glass slide provided with an additional PEG and DTT coating prepared on a piece of parafilm completely prevented both the gel and the cells from adhering. This was also verified with an additional multiphoton microscopy measurement. Moreover, during the investigation of this third hypothesis, it was also noticed that the temperature of the lab seems to impact the cell sedimentation in the gels containing Matrigel.

With the modifications made to both the protocol and the Teflon holders, two new cell-irradiation experiments were performed. A clear impact of the alpha particles on the cells could be observed on the day of irradiation, which indicates the modifications did seem to have resulted in an improvement. However, measuring the impact of the alpha particles in the subsequent days following the irradiation experiments still proved to be difficult due to gel fragments breaking off from the gel while performing the Resazurin assays. The addition of an additional agarose layer on top of the gel could provide a solution for this issue. Nonetheless, future irradiation experiments are required to investigate the effectiveness of the agarose layer.

Lastly, once the impact of the alpha particles on the cells can appropriately be measured in the subsequent days following irradiation, the time can be probed at which the difference in number of cells alive in the irradiated sample and the control sample is the largest. That way, in the next step of the experimental endeavor, the cell viability can be probed at this time.

Part II – Production of Isotopes for Cell Irradiation

In the second part of this thesis, the development of a recoil-implantation generator was discussed that can be used for the production of isotopes for cell-irradiation experiments. More specific for the production of ^{213}Bi and ^{223}Ra due to their promising results in clinical and preclinical trials. The goal of this part was twofold: (1) To see whether it is possible to build a recoil-implantation generator and implant the recoiling ^{225}Ac daughters on an empty aluminium disk and (2) to see whether an efficiency for the recoiling process can be deduced from the obtained data, should it be possible to implant the recoiling daughter nuclei.

Two experiments were performed of which the results were shown and discussed. Even though the activity of the ^{225}Ac implanted foil was low, clear peaks in the obtained spectra could be observed and identified based on the corresponding energy value and the branching ratio in the decay chain. Hence, it is indeed possible to implant the recoiling daughter nuclei on an empty aluminium disk. Moreover, based on the obtained spectra, an efficiency for the recoiling process could be derived in the form of a recoil efficiency ϵ_{Recoil}. This value was found to be equal to 0.1467(171), meaning that a ^{213}Bi source produced in this way is estimated to have an activity equal to 14.67(171) kBq due to the fact that an ^{225}Ac source produced at MEDICIS typically has an activity near 100 kBq.

For future measurements, when more ^{225}Ac is available with a higher activity compared to the foil that was used in this project, both parts of this thesis can be combined in a single cell-irradiation experiment: A ^{213}Bi source can be produced using the recoil-implantation generator such that the impact of this source on the cells embedded in the gel can be probed. However, the short ^{213}Bi half-life requires that the ^{213}Bi should be implanted anew for each cell-irradiation experiment. Even though an optimal implantation time equal to six hours, 26 minutes and 40 seconds was found, the implantation can start in the evening, the day before an irradiation experiment is planned, as it will only result in a difference of 3% compared to the optimal amount of implanted ^{213}Bi isotopes.

Bibliography

[1] Cleveland Clinic. Metastasis (Metastatic Cancer), December 2021. URL: https://my.clevelandclinic.org/health/diseases/22213-metastasis-metastatic-cancer, accessed on 04/01/2024.

[2] Van den Bergh V. Towards Alpha Dosimetry with Laser Ionized and Mass Separated ^{225}Ac: Setup Development and Source Characterization, 2022. URL: https://cds.cern.ch/record/2843398, accessed on 11/10/2023.

[3] National Cancer Institute. Types of Cancer Treatment. URL: https://www.cancer.gov/about-cancer/treatment/types, accessed on 03/01/2024.

[4] Laios K. et al. The Physician Who First Applied Radiotherapy, Victor Despeignes, on 1896. *Hell. J. Nucl. Med.*, 17(1):45–46, 2014.

[5] American Cancer Society. Getting External Beam Radiation Therapy. URL: https://www.cancer.org/cancer/managing-cancer/treatment-types/radiation/external-beam-radiation-therapy.html, accessed on 04/01/2024.

[6] Knoll G.F. *Radiation Detection and Measurement*. John Wiley & Sons, fourth edition, 2010.

[7] Miller R. et al. 9.13 - Brachytherapy Physics. In *Comprehensive Biomedical Physics*, volume 9, pages 315–381. Elsevier, 2014.

[8] L'Annunziata M.F. *Radioactivity: Introduction and History, from the Quantum to Quarks*. Elsevier, second edition, 2016.

[9] Liu L. et al. On the Depth of Penetration of Photons and Electrons for Intravascular Brachytherapy. *Cardiovascular Radiation Medicine*, 1(1):72–79, 1999.

[10] Andersson J.D. et al. Targeted Alpha Therapy: Progress in Radionuclide Production, Radiochemistry, and Applications. *Pharmaceutics*, 13(1), 2021.

[11] Bodei L. et al. Radiopharmaceutical Therapy in Ccancer: Clinical Advances and Challenges. *Nat. Rev. Drug Discov.*, 19:589–608, 2020.

[12] Van Rooyen J. Nuclear Physics for Nuclear Engineers, August 2018. URL: https://www.researchgate.net/publication/340378277_Nuclear_Physics_for_Nuclear_Engineers_Nuclear_Physics_for_Nuclear_Engineers, accessed on 05/01/2024.

[13] Kassis A.I. The Amazing World of Auger Electrons. *Int. J . Radiat. Biol.*, 80(11-12):789–803, November-December 2004.

[14] Murshed H. Radiation Biology. In *Fundamentals of Radiation Oncology*. Academic Press, 2019.

[15] Kratochwil C. et al. Targeted Alpha Therapy, an Emerging Class of Cancer Agents: A Review. *JAMA Oncol.*, 4(12):1765–1772, December 2018.

[16] Apostolidis C. et al. An Overview of Targeted Alpha Therapy with ^{225}Actinium and ^{213}Bismuth. *Curr. Radiopharm.*, 11(3):200–208, December 2018.

[17] D'huyvetter M. et al. Targeted Alpha Therapy Using Short-lived Alpha-particles and the Promise of Nanobodies as Targeting Vehicle. *Expert Opin. Biol. Ther.*, 16(8):1035–1047, August 2016.

[18] McDevitt M.R. et al. Realizing the Potential of the Actinium-225 Radionuclide Generator in Targeted Alpha-particle Therapy Applications. *Adv. Drug Deliv. Rev.*, 60(12):1371–1382, September 2008.

[19] Bakos G. et al. Atomic Nanogenerators in Targeted Alpha Therapies: Curie's Legacy in Modern Cancer Management. *Pharmaceuticals*, 13(4):76, April 2020.

[20] Brechbiel M.W. et al. An Overview of Targeted Alpha Therapy. *Tumour Biol.*, 33(3):573–590, June 2012.

[21] Chérel M. et al. Overview of the Most Promising Radionuclides for Targeted Alpha Therapy: The "Hopeful Eight". *Pharmaceutics*, 13(6):906, June 2021.

[22] SCK CEN. IBA en SCK CEN bundelen krachten om de productie van actinium-225 mogelijk te maken, September 2021. URL: https://www.sckcen.be/nl/nieuws/iba-en-sck-cen-bundelen-krachten-om-de-productie-van-actinium-225-mogelijk-te-maken, accessed on 02/01/2024.

[23] Apostolidis C. et al. ^{225}Ac-PSMA-617 for PSMA-Targeted α-Radiation Therapy of Metastatic Castration-Resistant Prostate Cancer. *Journal of Nuclear Medicine*, 57(12):1941–1944, December 2016.

[24] Cieszanowski A. et al. Diagnosis and Treatment of Peritoneal Carcinomatosis – A Comprehensive Overview. *Pol. J. Radiol.*, 88:e89–e97, February 2023.

[25] Vankeirsbilck J. Internship at the Interdisciplinary Group at IKS, November 2021.

[26] Meurrens N. Alpha Particle Microdosimetry Simulations For Cell-irradiation Experiments, October 2023.

[27] Bashir S. et al. Fundamental Concepts of Hydrogels: Synthesis, Properties, and Their Applications. *Polymers (Basel).*, 12(11), 2020.

[28] Hong W. et al. Mechanics and Physics of Hydrogels. *Soft Matter*, 8:8006–8007, 2012.

[29] Katt M.E. et al. *In Vitro* Tumor Models: Advantages, Disadvantages, Variables, and Selecting the Right Platform. *Front. Bioeng. Biotechnol.*, 4(12), 2016.

[30] National Institute of Health. HeLa Cells: A Lasting Contribution to Biomedical Research, October 2022. URL: https://osp.od.nih.gov/hela-cells/, accessed on 06/06/2024.

[31] Wang X. et al. Nanostructured Dense Collagen-Polyester Composite Hydrogels as Amphiphilic Platforms for Drug Delivery. *Advanced Science*, 8(7), 2021.

[32] Avantor™ Delivered By VWR™. VWR Cell Culture Flasks. URL: https://us.vwr.com/store/product/12585790/vwr-cell-culture-flasks, accessed on 28/09/2023.

[33] ThermoFisher Scientific. Balanced Salt Solutions. URL: https://www.thermofisher.com/be/en/home/life-science/cell-culture/mammalian-cell-culture/reagents/balanced-salt-solutions.html?gclid=CjwKCAjwyNSoBhA9EiwA5aYlb9BUudjYtSjmoDl8_0SUjhiEJzsPHRMsRYNgi2Uo0K2HqE1BmhvwFRoCWzwQAvD_BwE&ef_id=CjwKCAjwyNSoBhA9EiwA5aYlb9BUudjYtSjmoDl8_0SUjhiEJzsPHRMsRYNgi2Uo0K2HqE1BmhvwFRoCWzwQAvD_BwE:G:s&s_kwcid=AL!3652!3!596250123735!e!!g!!pbs%20cell%20culture!1759362858!68599252043&cid=bid_clb_cce_r01_co_cp0000_pjt0000_bid00000_0se_gaw_nt_pur_con, accessed on 28/09/2023.

[34] ThermoFisher Scientific. DPBS, no calcium, no magnesium. URL: https://www.thermofisher.com/order/catalog/product/14190144, accessed on 29/09/2023.

[35] ThermoFisher Scientific. Versene Solution. URL: https://www.thermofisher.com/order/catalog/product/15040066?gclid=CjwKCAjwyNSoBhA9EiwA5aYlbxRnZjkiW_Zvv0LFZ3WAYi4SBRe8JDnQbY19DrAEnr6i76ogprGC6hoCvHYQAvD_BwE&ef_id=CjwKCAjwyNSoBhA9EiwA5aYlbxRnZjkiW_Zvv0LFZ3WAYi4SBRe8JDnQbY19DrAEnr6i76ogprGC6hoCvHYQAvD_BwE:G:s&s_kwcid=AL!3652!3!530347123803!!!g!!!382790548!127140246227&cid=bid_clb_cce_r01_co_cp0000_pjt0000_bid00000_0se_gaw_dy_pur_con&s_kwcid=AL!3652!3!530347123803!!!g!!, accessed on 28/09/2023.

[36] Kambli N. Passaging hES/iPS cells using Versene EDTA, March 2020. URL: https://www.salk.edu/wp-content/uploads/2021/11/3.-Versene-EDTA-Passaging-protocol.pdf, accessed on 28/09/2023.

[37] New Jersey Department of Health. Hazardous Substance Fact Sheet, December 2008. URL: https://www.nj.gov/health/eoh/rtkweb/documents/fs/0876.pdf, accessed on 28/09/2023.

[38] Fuentes M. Hemocytometer square size. URL: https://www.hemocytometer.org/hemocytometer-square-size/, accessed on 01/10/2023.

[39] Bastidas O. Cell Counting with Neubauer Chamber: Basic Hemocytometer Usage. URL: https://mural.uv.es/basgaros/Cell-counting-Neubauer-chamber.pdf, accessed on 01/10/2023.

[40] B10Numb3r5 – The Database of Useful Biological Numbers. HeLa cell volume. URL: https://bionumbers.hms.harvard.edu/bionumber.aspx?id=103725, accessed on 01/10/2023.

[41] Thevelein J. et al. *Celbiologie en biochemie - Deel 1.* Acco, 2018-2019.

[42] National Nuclear Data Center (NNDC) at Brookhaven National Laboratory. Decay Radiation Information (^{241}Am). URL: https://www.nndc.bnl.gov/nudat3/DecayRadiationServlet?nuc=241Am&unc=NDS, accessed on 16/12/2023.

[43] Csepregi R. et al. Complex Formation of Resorufin and Resazurin with B-Cyclodextrins: Can Cyclodextrins Interfere with a Resazurin Cell Viability Assay? *PubMed Central*, 32(2), February 2018.

[44] B10Numb3r5 – The Database of Useful Biological Numbers. Cell cycle duration of HeLa cell. URL: https://bionumbers.hms.harvard.edu/bionumber.aspx?id=109393, accessed on 26/05/2024.

[45] Karu T.I. Exact Action Spectra for Cellular Responses Relevant to Phototherapy. *Photomedicine and Laser Surgery*, 23(4):355–361, 2005.

[46] SciPy documentation. Orthogonal Distance Regression (`scipy.odr`). URL: https://docs.scipy.org/doc/scipy/reference/odr.html, accessed on 15/09/2023.

[47] Bevington P.R. *Data Reduction and Error Analysis for the Physical Sciences.* New York: McGraw-Hill, 1969.

[48] Bartic C. et al. Stress-controlled Shear Flow Alignment of Collagen Type I Hydrogel Systems. *Acta Biomaterialia*, 150:128–137, 2022.

[49] Hillier K. Polyethylene Glycol. In Bylund D.B et al., editor, *xPharm: The Comprehensive Pharmacology Reference*, pages 1–3. Elsevier, New York, 2007.

[50] NSP - Nanosoft Polymers. 8-arm PEGs. URL: https://www.nanosoftpolymers.com/product-category/functional-pegs/8-arm-pegs/, accessed on 15/11/2023.

[51] Franck A. Viscoelasticity and Dynamic Mechanical Testing. TA Instruments Germany, URL: https://www.tainstruments.com/pdf/literature/AAN004_Viscoelasticity_and_DMA.pdf, accessed on 16/05/2024.

[52] Corning. Corning® Matrigel® Matrix. URL: https://www.scientificlabs.co.uk/handlers/libraryFiles.ashx?filename=Technical_Data_Sheets_3_356234_L.pdf, accessed on 04/11/2023.

[53] Jessop Z.M. et al. 8 - Candidate Bioinks for 3D Bioprinting Soft Tissue. In *3D Bioprinting for Reconstructive Surgery*, pages 145–172. Woodhead Publishing, 2018.

[54] Hubbell J.A. Chapter 21 - Matrix Effects. In *Principles of Tissue Engineering (Fourth Edition)*, pages 407–421. Academic Press, Boston, Fourth edition, 2014.

[55] Bächinger H.P. et al. 5.16 - Collagen Formation and Structure. In *Comprehensive Natural Products II*, pages 469–530. Elsevier, Oxford, 2010.

[56] Kaur J. et al. 3.5.2 Collagen Type IV. In *Stem Cell Biology and Tissue Engineering in Dental Sciences*. Academic Press, 2015.

[57] Esko J.D. et al. Heparan Sulfate Proteoglycans. *Cold Spring Harb. Perspect. Biol.*, 3(7), July 2011.

[58] Antoine E.E. et al . Review of Collagen I Hydrogels for Bioengineered Tissue Microenvironments: Characterization of Mechanics, Structure, and Transport. *Tissue Eng. Part B Rev.*, 20(6):683–696, December 2014.

[59] Fu L. et al. A Confocal Endoscope for Cellular Imaging. *Engineering*, 1(3):351–360, 2015.

[60] Prasad V. et al. How Does a Confocal Microscope Work? URL: https://physics.emory.edu/faculty/weeks/confocal/, accessed on 30/10/2023.

[61] Hofkens J. Applications of Fluorescence in Biological Systems, 2021-2022. Slides for the course "Spectroscopy of Biomolecules (G0O58C)" taught at KU Leuven.

[62] ThermoFisher Scientific. Calcein, AM, cell-permeant dye. URL: https://www.thermofisher.com/order/catalog/product/C1430, accessed on 12/10/2023.

[63] Fisher Scientific. Invitrogen™ Calcein, AM. URL: https://www.fishersci.be/shop/products/molecular-probes-calcein-am-1/10720345, accessed on 04/11/2023.

[64] ThermoFisher Scientific. Ethidium Homodimer-1 (EthD-1). URL: https://www.thermofisher.com/order/catalog/product/E1169?gclid=Cj0KCQjwsp6pBhCfARIsAD3GZuZ_tUueoGbMCBnuDu9xwWvWkZi00X06Qmzf2cSiQrf3FkZy1r4hz9caAlYMEALw_wcB&ef_id=Cj0KCQjwsp6pBhCfARIsAD3GZuZ_tUueoGbMCBnuDu9xwWvWkZi00X06Qmzf2cSiQrf3FkZy1r4hz9caAlYMEALw_wcB:G:s&s_kwcid=AL!3652!3!447292198730!!!g!!!10506731179!109642167491&cid=bid_pca_iva_r01_co_cp1359_pjt0000_bid00000_0se_gaw_dy_pur_con, accessed on 12/10/2023.

[65] Avantor™ Delivered By VWR™. HEPES (2-[4-(2-hydroxyethyl)-1-piperazinyl]ethanesulphonic acid) ≥ 99.5%. URL: https://nl.vwr.com/store/product/2360060/null, accessed on 26/09/2023.

[66] ImageJ Wiki. Fiji. URL: https://imagej.net/software/fiji/, accessed on 08/12/2023.

[67] Bell B.J. et al. Polymerization and Matrix Physical Properties as Important Design Considerations for Soluble Collagen Formulations. *Biopolymers*, 93:690, 2010.

[68] Abraham L.C. et al. Guide to Collagen Characterization for Biomaterial Studies. *J. Biomed. Mater. Res. B Appl. Biomater.*, 87B:264, 2008.

[69] Jai Chun H. et al. Multiphoton Microscopy: An Introduction to Gastroenterologists. *World J. Gastroenterol.*, 17(40):4456–4460, October 2011.

[70] The University of Queensland Australia. Brightfield Techniques. URL: https://imb.uq.edu.au/research/facilities/microscopy/training-manuals/microscopy-online-resources/image-capture/brightfield-techniques, accessed on 27/05/2024.

[71] Chemical Book. Jeffamine M-600(R). URL: https://www.chemicalbook.com/ChemicalProductProperty_EN_CB8420220.htm, accessed on 14/03/2024.

[72] Elespuru R.K. et al. The Photoinitiator Lithium Phenyl (2,4,6-Trimethylbenzoyl) Phosphinate with Exposure to 405 nm Light Is Cytotoxic to Mammalian Cells but Not Mutagenic in Bacterial Reverse Mutation Assays. *Polymers (Basel).*, 12(7):1489, July 2020.

[73] Hagemann A. et al. Review: 3-Aminopropyltriethoxysilane (APTES) Deposition Methods on Oxide Surfaces in Solution and Vapor Phases for Biosensing Applications. *Biosensors*, 13(1), 2023.

[74] Bryant S.J. et al. Comparative Study of the Viscoelastic Mechanical Behavior of Agarose and Poly(ethylene glycol) Hydrogels. *Wiley Online Library*, April 2011.

[75] Bodera F. et al. The Dance of the Nanobubbles: Detecting Acoustic Backscatter From Sub-Micron Bubbles Using Ultra-High Frequency Acoustic Microscopy. *Nanoscale*, 12, 2020.

[76] Krane K.S. *Introductory Nuclear Physics*. John Wiley & Sons, 1987.

[77] Stora T. et al. CERN-MEDICIS: Operational Indicators to Support the Production of New Medical Radionuclides by Mass-Separation. *Journal of Physics: Conference Series*, 2687(8):082039, January 2024.

[78] Mirion Technologies. The Continuous Air Monitoring (CAM) PIPS® Detector Properties and Applications. URL: https://mirionprodstorage.blob.core.windows.net/prod-20220822/cms4_mirion/files/cam-pips-detector-properties-app-note-c39167_wj540px.pdf, accessed on 08/04/2024.

[79] CAEN. *CoMPASS Multiparametric DAQ Software for Physics Applications (User Manual)*, November 2023.

[80] Cocolios T.E. et al. A Simple Decay-spectroscopy Station at CRIS-ISOLDE. *Nuclear Instruments and Methods in Physics Research Section A: Accelerators, Spectrometers, Detectors and Associated Equipment*, 844:14–18, 2017.

[81] Scipy.org. Scipy.stats.crystalball. URL: https://docs.scipy.org/doc/scipy/reference/generated/scipy.stats.crystalball.html, accessed on 05/04/2024.

[82] Chu S.Y.F. et al. The Lund/LBNL Nuclear Data Search. LBNL, Berkeley, USA, Department of Physics, Lund University, Sweden. URL: http://nucleardata.nuclear.lu.se/toi/, accessed on 07/12/2023.

[83] National Nuclear Data Center (NNDC) at Brookhaven National Laboratory. NuDat 3.0. URL: https://www.nndc.bnl.gov/nudat3/, accessed on 07/12/2023.

[84] Cetnar J. General Solution of Bateman Equations For Nuclear Transmutations. *Annals of Nuclear Energy*, 33:640–645, 2006.

[85] de Oliveira S.L. et al. General Solution To Bateman's Differential Equations With Direct Index Notation. *International Journal of Pure and Applied Mathematics*, 93(6):879–883, 2014.

[86] Fisher Scientific. Gibco™ Fetal Bovine Serum, value (formerly USDA-approved in North America or qualified, Brazil in other regions). URL: https://www.fishersci.ie/shop/products/fetal-bovine-serum-value-one-shot-format-1/17553595, accessed on 02/10/2023.

[87] ThermoFisher Scientific. Penicillin-Streptomycin (10,000 U/mL). URL: https://www.thermofisher.com/order/catalog/product/15140122, accessed on 02/10/2023.

[88] ThermoFisher Scientific. MEM Non-Essential Amino Acids Solution (100×). URL: https://www.thermofisher.com/order/catalog/product/11140050, accessed on 02/10/2023.

[89] ThermoFisher Scientific. DMEM, high glucose, GlutaMAX™ Supplement, pyruvate. URL: https://www.thermofisher.com/order/catalog/product/10569010?gclid=CjwKCAjwgsqoBhBNEiwAwe5w0_8eHl2TNie35rZos1d9fd4XzLgOR6BbLWqRtuTDQ_wOrdX_AYV0exoC74IQAvD_BwE&ef_id=CjwKCAjwgsqoBhBNEiwAwe5w0_8eHl2TNie35rZos1d9fd4XzLgOR6BbLWqRtuTDQ_wOrdX_AYV0exoC74IQAvD_BwE:G:s&s_kwcid=AL!3652!3!530347123803!!!g!!!382790548!127140246227&cid=bid_clb_cce_r01_co_cp0000_pjt0000_bid00000_0se_gaw_dy_pur_con&s_kwcid=AL!3652!3!530347123803!!!g!!, accessed on 26/09/2023.

[90] ThermoFisher Scientific. Technical Resources: 10569 - DMEM, high glucose, GlutaMAX(TM), pyruvate. URL: https://www.thermofisher.com/be/en/home/technical-resources/media-formulation.46.html, accessed on 26/09/2023.

[91] Edinburgh Instruments. What is a Jablonski Diagram (Perrin-Jablonski Diagram)? URL: https://www.edinst.com/blog/jablonski-diagram-2/, accessed on 15/09/2023.

[92] Hofkens J. Introduction to Fluorescence, 2021-2022. Slides for the course "Spectroscopy of Biomolecules (G0O58C)" taught at KU Leuven.

[93] Bender C.F. et al. A Simple Method of Removing Spin Contamination From Unrestricted Kohn-Sham Density Functional Calculations. *Theoretical and Computational Chemistry*, 4, 1996.

[94] BMG Labtech. Fluorescence Intensity (incl. FRET). URL: https://www.bmglabtech.com/en/fluorescence-intensity/, accessed on 15/09/2023.

[95] Haberstock S. How to Develop an Optimal Fluorescence Assay. URL: https://www.tecan.com/blog/how-to-develop-an-optimal-fluorescence-assay, accessed on 15/09/2023.

[96] TRIUMF. ICIS 2023 – 20^{th} International Conference on Ion Sources, September 2023.

[97] Cocolios T.E. et al. ISOL Technique for the Production of 225Ac at CERN-MEDICIS. *Journal of Medical Imaging and Radiation Sciences*, 50(4, Supplement 1):S92, 2019.

[98] Marsh B. Resonance Ionization Laser Ion Sources, 2013. URL: https://cds.cern.ch/record/1967371/files/CERN-2013-007-p203.pdf, accessed on 09/04/2024.

[99] Van Duppen P. Isotope Separation On Line and Post Acceleration. In *Lecture Notes in Physics*. Springer, 2006.

Part III

Appendices

"Mini cupcakes? As in the mini version of regular cupcakes? Which is already a mini version of cake? Honestly, where does it end with you people?"

Kevin Malone – The Office

A

Nutrient Medium For Supporting Cell Growth

In this appendix, further reference is provided on the nutrient medium that was used for supporting cell growth. The nutrient medium used in this project contains 10% of Gibco™'s fetal bovine serum (FBS) [86], 1% of Gibco™'s Penicillin Streptomycin (Pen Strep) containing 10000 units/mL of penicillin and 10000 μg/mL of streptomycin [87], 1% of Gibco™'s minimum essential medium non-essential amino acids (MEM NEAA) [88] and 88% of Gibco™'s Dulbecco's modified eagle medium (DMEM). DMEM contains high quantities of glucose, sodium pyruvate, GlutaMAX™ and phenol red, but was prepared without HEPES (2-[4-(2-hydroxyethyl)-1-piperazinyl]ethanesulphonic acid) [89, 65]. More specifically, each component in the modified DMEM can be categorised as either an amino acid, a vitamin, an inorganic salt or as an other component (i.e., components that cannot be placed in one of the first three categories). The molecular weight and concentration of each component in the modified DMEM is summarized in Table A.1, Table A.2, Table A.3 and Table A.4.

Table A.1: *Summary of the molecular weight (in u) and concentration (in mg/L) of each vitamin in the DMEM. Information obtained from [90].*

Component	Molecular weight [u]	Concentration [mg/L]
Choline chloride	140.0	4.0
D-Calcium pantothenate	477.0	4.0
Folic Acid	441.0	4.0
Niacinamide	122.0	4.0
Pyridoxine hydrochloride	206.0	4.0
Riboflavin	376.0	0.4
Thiamine hydrochloride	337.0	4.0
i-Inositol	180.0	7.2

Table A.2: *Summary of the molecular weight (in u) and concentration (in mg/L) of each amino acid in the DMEM. Information obtained from [90].*

Component	Molecular weight [u]	Concentration [mg/L]
Glycine	75.0	30.0
L-Alanyl-Glutamine	217.0	862.0
L-Arginine hydrochloride	211.0	84.0
L-Cystine 2HCl	313.0	63.0
L-Histidine hydrochloride-H_2O	210.0	42.0
L-Isoleucine	131.0	105.0
L-Leucine	131.0	105.0
L-Lysine hydrochloride	183.0	146.0
L-Methionine	149.0	30.0
L-Phenylalanine	165.0	66.0
L-Serine	105.0	42.0
L-Threonine	119.0	95.0
L-Tryptophan	204.0	16.0
L-Tyrosine disodium salt dihydrate	261.0	104.0
L-Valine	117.0	94.0

Table A.3: *Summary of the molecular weight (in u) and concentration (in mg/L) of each inorganic salt in the DMEM. Information obtained from [90].*

Component	Molecular weight [u]	Concentration [mg/L]
Calcium Chloride ($CaCl_2$) (anhyd.)	111.0	200.0
Ferric Nitrate ($Fe(NO_3)_3 \cdot 9H_2O$)	404.0	0.1
Magnesium Sulfate ($MgSO_4$) (anhyd.)	120.0	97.67
Potassium Chloride (KCl)	75.0	400.0
Sodium Bicarbonate ($NaHCO_3$)	84.0	3700.0
Sodium Chloride (NaCl)	58.0	6400.0
Sodium Phosphate monobasic ($NaH_2PO_{4-} \cdot H_2O$)	138.0	125.0

Table A.4: *Summary of the molecular weight (in u) and concentration (in mg/L) of each component in the DMEM that was labeled as "other component". Information obtained from [90].*

Component	Molecular weight [u]	Concentration [mg/L]
D-Glucose (Dextrose)	180.0	4500.0
Phenol Red	376.4	15.0
Sodium Pyruvate	110.0	110.0

"Do I need to be liked? Absolutely not. I like to be liked. I enjoy being liked. I have to be liked. But its not like this, compulsive, need, to be liked. Like my need to be praised."

Michael Scott – The Office

B

Basic Principles of Fluorescence

Jablonski diagrams are often used to visualize and interpret all radiative and non-radiative transitions underlying the observed fluorescence spectra of molecules. In this appendix, the basic principles of fluorescence will be discussed starting from a Jablonski diagram.

B.1 Jablonski Diagram

Consider the Jablonski diagram shown in Figure B.1.

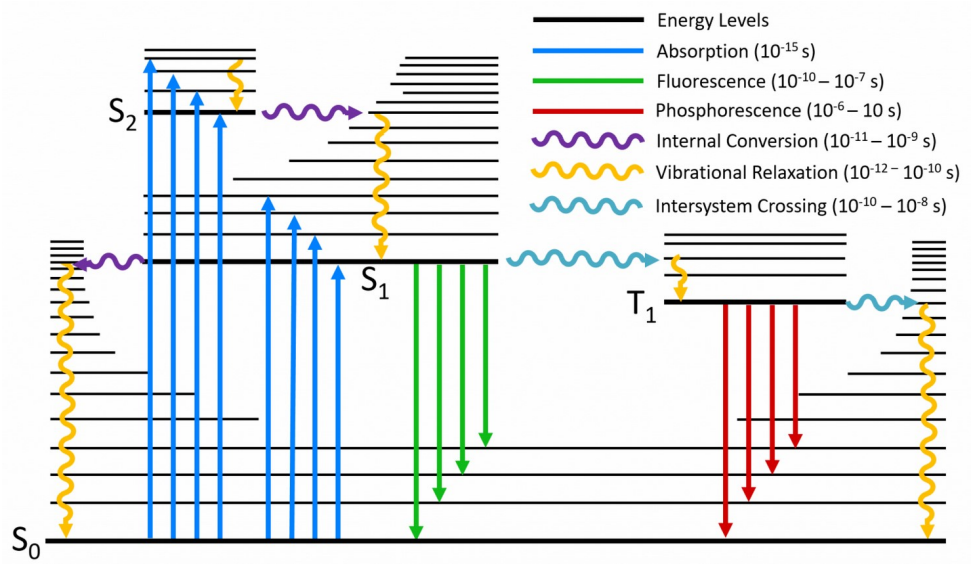

Figure B.1: *Illustration of a Jablonski diagram indicating all possible radiative and non-radiative pathways. The timescale of each pathway is also indicated in the legend of the figure. Figure obtained from [91].*

Each horizontal line indicates a vibrational state. The lowest vibrational state of an electronic state is indicated in bold and is often labeled with an S or a T. The capital

S stands for "Singlet state" (i.e. a total spin angular momentum equal to zero), such that S_0 is the singlet ground state of a molecule and S_n the n^{th} excited singlet state. The capital T stands for "Triplet state" (i.e. total spin angular momentum equal to one) such that T_n is the n^{th} excited triplet state [91]. The n^{th} excited triplet state is always slightly lower in energy compared to the n^{th} excited singlet state [92]. Most molecules have a singlet state as a ground state, but this is not true for every molecule: A counterexample is molecular oxygen which has a triplet state as ground state [91, 93].

When a substance is irradiated with light, the photons can be absorbed by the molecules of the substance resulting in the excitation of one or more electrons to an excited vibrational state. Once the molecule is in an excited state, three non-radiative processes can occur:

1. Internal conversion, which is an isoenergetic transition from a vibrational level in an electronic state towards a vibrational level in a different electronic state having the same spin multiplicity (indicated in purple in Figure B.1). Timescale: 10^{-11} - 10^{-9} seconds [92].

2. Vibrational relaxation, which is transition from a higher vibrational state to a lower vibrational state within the same electronic state (indicated in yellow in Figure B.1). Timescale: 10^{-12} - 10^{-10} seconds [92].

3. Intersystem crossing, which is an isoenergetic transition from a vibrational level in an electronic state towards a vibrational level in a different electronic state having a different spin multiplicity (indicated in light blue in Figure B.1). Timescale: 10^{-10} - 10^{-8} seconds [92].

Both internal conversion and vibrational relaxation are transitions between two vibrational levels with the same spin multiplicity and thus are quantum mechanically allowed transitions. Intersystem crossing, on the other hand, is a transition between two vibrational levels having a different spin multiplicity and thus is a quantum mechanically forbidden transition. As a result, internal conversion and vibrational relaxation typically occur before intersystem crossing [91, 92].

On the other hand, there are two radiative pathways that can occur as well:

1. Fluorescence, which is a transition between two electronic states with the same spin multiplicity (indicated in green in Figure B.1). However, in practice, fluorescence typically only occurs in the transition of S_1 towards S_0 as a consequence of vibrational relaxation. Timescale: 10^{-10} - 10^{-7} seconds [92].

2. Phosphorescence, which a transition between two electronic states with different spin multiplicity (indicated in red in Figure B.1). Timescale: 10^{-6} - 10 seconds [92].

Fluorescence is a transition between two singlet states and is thus a quantum mechanically allowed transition. Phosphorescence, on the other hand, is a quantum mechanically forbidden transition which explains why fluorescence typically occurs before phosphorescence when comparing the timescales of both pathways [91]. Vibrational relaxation almost always occurs before fluorescence. Hence, when a molecule of a substance absorbs a photon, the wavelength of the emitted photon as a result of fluorescence will almost always be larger than the wavelength of the absorbed photon [92].

B.2 Bandwidth

The illustration in Figure B.2 shows a typical excitation and fluorescence emission spectrum of a molecule.

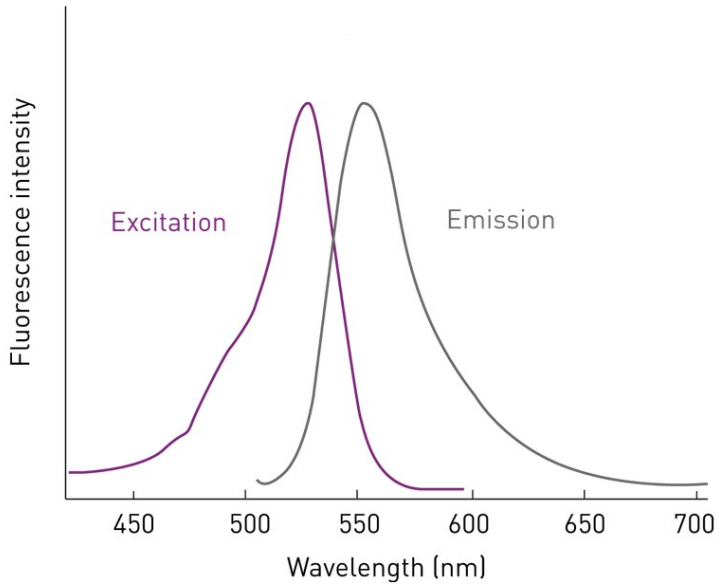

Figure B.2: *Illustration of a typical excitation and fluorescence emission spectrum. Figure slightly adapted from [94].*

When a sample is irradiated with light, the amount of absorption depends on the wavelength of the photons, as can clearly be seen in Figure B.2. Hence, to maximize the emission of photons due to fluorescence, it is important to irradiate the molecules of the sample with light at the right wavelength. The bandwidth associated to the excitation or emission wavelength indicates the range of photon wavelengths exciting or emitted from the sample. More specifically, let λ be the wavelength of the light irradiating the sample and let $\Delta\lambda$ be the associated bandwidth. Then the sample is irradiated with photons having a wavelength ranging from $\lambda - \frac{\Delta\lambda}{2}$ up to $\lambda + \frac{\Delta\lambda}{2}$. In a similar way, if λ' is the wavelength of the photons emitted from the sample as a result of fluorescence and $\Delta\lambda'$ is the associated bandwidth, then the sample emits fluorescence photons ranging from $\lambda' - \frac{\Delta\lambda'}{2}$ up to $\lambda' + \frac{\Delta\lambda'}{2}$ [95].

"She's one of my 447 Facebook friends. Everyone wants a slice."

Phil Dunphy – Modern Family

C

The ^{225}Ac and ^{227}Ac Decay Chains

The ^{225}Ac and ^{227}Ac decay chains are respectively shown in Figure C.1 and Figure C.2.

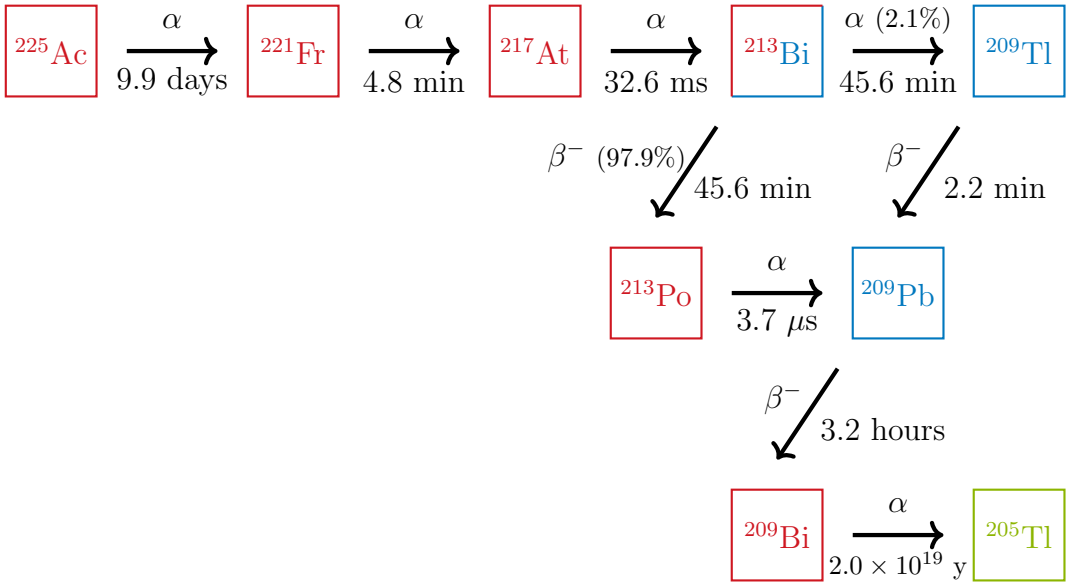

Figure C.1: *The ^{225}Ac decay chain. The isotopes indicated in red decay through α-decay, the isotopes in blue decay through β^--decay and the isotopes in green are stable. The half-life of each isotope is written next to each decay. The image is based upon the information retrieved from [82, 83].*

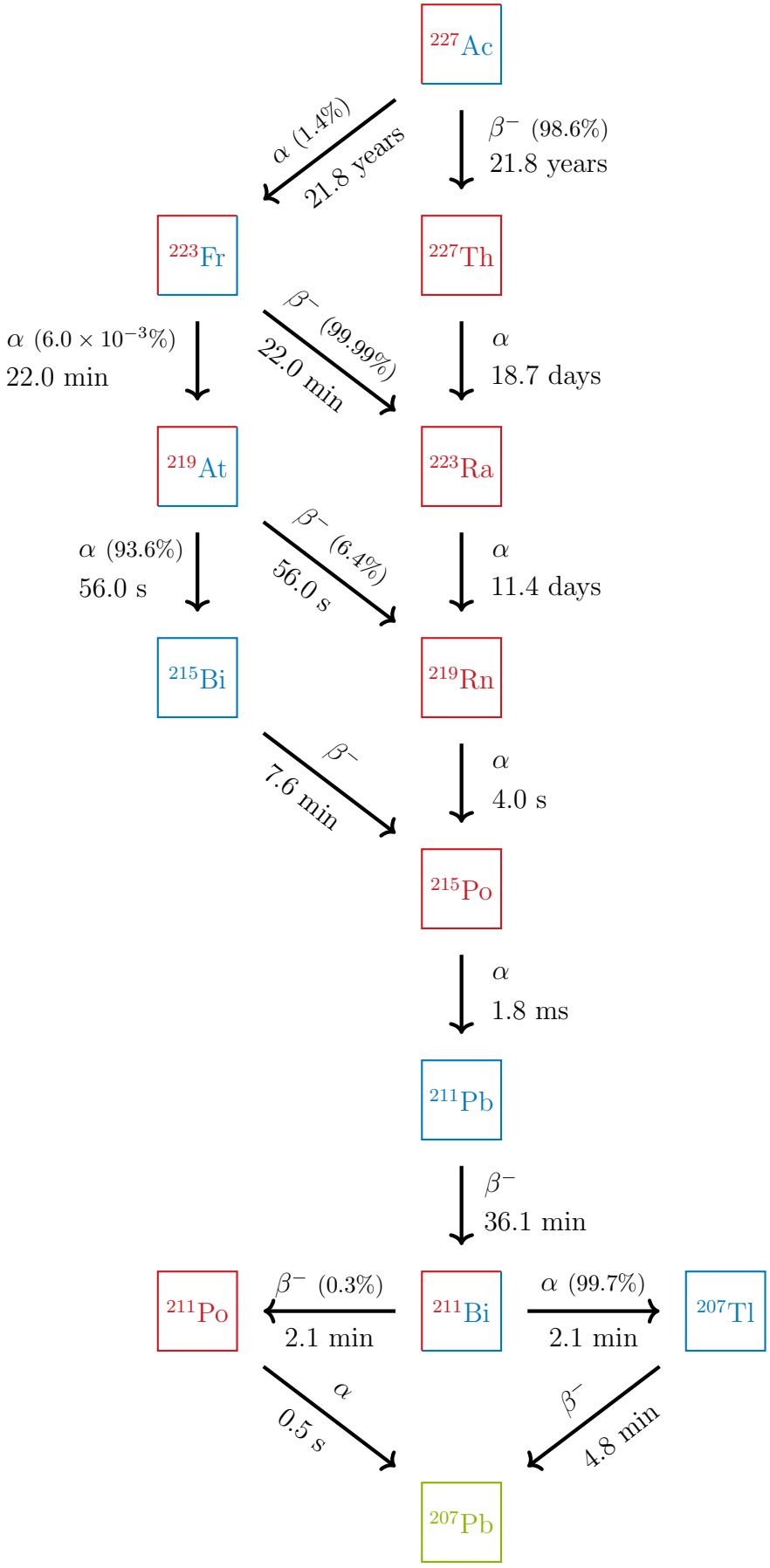

Figure C.2: *The ^{227}Ac decay chain. The isotopes indicated in red decay through α-decay, the isotopes in blue decay through β^--decay and the isotopes in green are stable. The half-life of each isotope is written next to each decay. The image is based upon the information retrieved from [82, 83].*

"Claire likes to say you can be part of the problem or part of the solution. But I happen to believe you can be both."

Phil Dunphy – Modern Family

D
The ISOL method

Further reference will be provided in this appendix on the ISOL method based on the schematic illustration provided in Figure D.1.

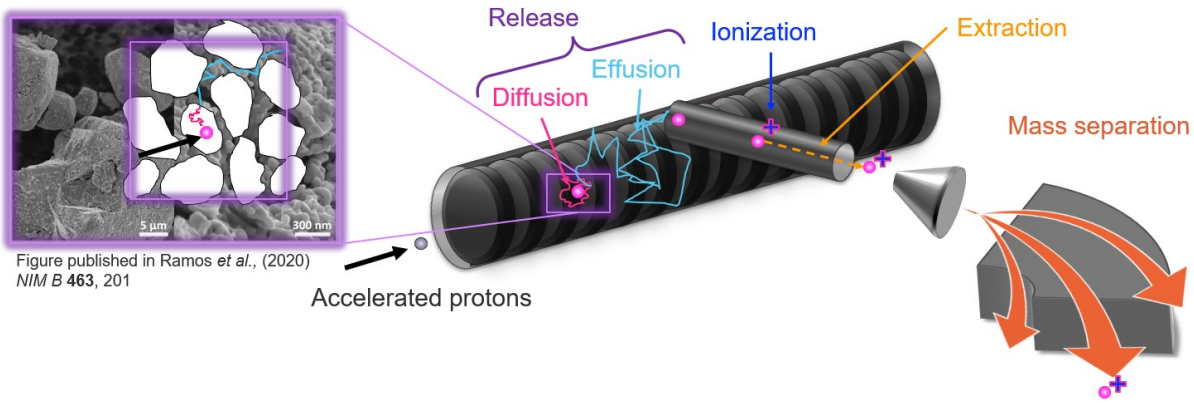

Figure D.1: *A schematic overview of the ISOL method. Figure obtained from [96].*

The first step in the ISOL method, is to collide high-energy protons on a heated target ($\sim$ 2000 °C). At CERN, the energy of the protons is of the orders of GeV. As a result, nuclear reactions will occur within the target to produce the required isotopes together with many by-products. For the production of ^{225}Ac at MEDICIS, a thorium carbide (ThC) target is used. The high heat of the target enables the diffusion (i.e., the movement of the isotopes within the grains of the target) and effusion (i.e., the movement of the isotopes between the grains of the target) process. Both the required ^{225}Ac and the formed by-products are extracted from the target in this way as shown in Figure D.1. However, to get rid of the many by-products and to obtain a pure ^{225}Ac beam in the end, the extracted isotopes are first partially selected based on their chemical element using a resonant ionisation laser ion source. Afterwards, they pass through a magnetic field such that the ionised elements can be selected based on their mass in order to distinguish between isotopes. The resonant ionisation laser ion source makes use of a

series of frequencies corresponding to the electron transitions of the required atom. Hence, if the frequencies are chosen in such a way they correspond to the electronic transitions of actinium, only the required actinium atoms become ionized as a result of the stepwise excitation. In the next step, the extracted elements arrive at the mass separator where the ionised atoms are separated based on their mass using an analyzing magnet. Contrarily to the target and ion source that are put on high voltage (i.e., $\sim$ 40 - 60 kV), the mass separator on the other hand is grounded. Hence, the only force acting on the charged particles is the Lorentz force as a consequence of the magnetic field ($\sim$ 300 mT). As a result, it can be shown using Newton's second law of motion that the charged particles will travel along a circular trajectory and that the radius r of this trajectory will be equal to

$$r = \frac{mv}{|q|B}, \tag{D.1}$$

where m is the mass of the isotopes, v their velocity, $|q|$ the magnitude of their charge and B the magnitude of the magnetic field. Hence, based on the curvature of the circular trajectory, different isotopes can be distinguished from each other based on their mass. Finally, after passing through the magnetic field, the isotopes are implanted on an aluminium-coated gold foil which is the foil that was used for the experiments in this project [97, 98, 99].

"I know it's hard to believe, but I was actually a bit of a nerd back in the day and it was suggested that I was out of my league when I landed Claire. By Jay mostly, and my friends, and my parents and Claire."

Phil Dunphy – Modern Family

E

The Uncertainty Associated to the Weighted Mean

The weighted mean and the uncertainty associated to the weighted mean were utilized in section 5.5 to obtain a value for the recoil efficiency. In this appendix, further reference on the weighted mean and a derivation of the uncertainty on the weighted mean will be provided.

When n values x_1, x_2, ..., x_n are measured, with an uncertainty σ_1, σ_2, ..., σ_n respectively, the weighted mean $\langle x \rangle$ is then defined such that

$$\langle x \rangle = \frac{\sum_{i=1}^{n} x_i \cdot w_i}{\sum_{i=1}^{n} w_i}. \tag{E.1}$$

The values w_1, w_2, ..., w_n are weight factors defined such that $w_i = \frac{1}{\sigma_i^2}$ for each $i \in \{1, 2, ..., n\}$. Obeying the rules regarding uncertainty propagation, the uncertainty $\sigma_{\langle x \rangle}$ on the weighted mean can be determined as

$$\sigma_{\langle x \rangle} = \sqrt{\sum_{i=1}^{n} \left(\frac{\partial \langle x \rangle}{\partial x_i} \right)^2 \cdot \sigma_i^2}. \tag{E.2}$$

Using Equation E.1, this expression can be rearranged such that

$$\begin{aligned} \sigma_{\langle x \rangle} &= \sqrt{\sum_{i=1}^{n} \left(\frac{1}{\sum_{j=1}^{n} w_j} \right)^2 \cdot \left(\frac{\partial}{\partial x_i} \left[\sum_{k=1}^{n} x_k \cdot w_k \right] \right)^2 \cdot \sigma_i^2} \\ &= \sqrt{\left(\frac{1}{\sum_{j=1}^{n} w_j} \right)^2 \cdot \sum_{i=1}^{n} \left(\sum_{k=1}^{n} \frac{\partial x_k}{\partial x_i} \cdot w_k \right)^2 \cdot \sigma_i^2} \\ &= \frac{1}{\sum_{j=1}^{n} w_j} \cdot \sqrt{\sum_{i=1}^{n} \left(\sum_{k=1}^{n} \delta_{ki} \cdot w_k \right)^2 \cdot \sigma_i^2} \end{aligned} \tag{E.3}$$

due to the fact that each $w_j > 0$ and thus no absolute values are required. The symbol δ_{ki} represents a Kronecker delta, meaning that

$$\delta_{ki} = \begin{cases} 1, & k = i \\ 0, & k \neq i. \end{cases} \tag{E.4}$$

Hence,

$$\sum_{k=1}^{n} \delta_{ki} \cdot w_k = w_i. \tag{E.5}$$

Combining this result with the expression on the final line of Equation E.3, it is found that

$$\begin{aligned} \sigma_{\langle x \rangle} &= \frac{1}{\sum_{j=1}^{n} w_j} \cdot \sqrt{\sum_{i=1}^{n} w_i^2 \cdot \sigma_i^2} \\ &= \frac{1}{\sum_{j=1}^{n} w_j} \cdot \sqrt{\sum_{i=1}^{n} w_i} \\ &= \frac{1}{\sqrt{\sum_{i=1}^{n} w_i}} \end{aligned} \tag{E.6}$$

due to the fact that

$$\begin{aligned} w_i^2 \cdot \sigma_i^2 &= \frac{1}{\sigma_i^4} \cdot \sigma_i^2 \\ &= \frac{1}{\sigma_i^2} \\ &= w_i. \end{aligned} \tag{E.7}$$

Department of Physics and Astronomy
Celestijnenlaan 200D – Bus 2412
3001 HEVERLEE, BELGIUM
tel. +32 16 32 71 24
https://fys.kuleuven.be/english